UNIVERSITY OF SOUTHAMPTON

FACULTY OF ENGINEERING, SCIENCE AND MATHEMATICS

INSTITUTE OF SOUND AND VIBRATION RESEARCH

SOUND RADIATION FROM A VIBRATING SURFACE UNDER A BOUNDARY LAYER

by Malcolm Gordon Smith

A thesis submitted for the degree of
Doctor of Philosophy

January 2004

Abstract

This thesis investigates the sound field generated by a plane vibrating surface radiating into a moving fluid. The mean flow considered consists of a semi-infinite fluid flowing parallel to a surface, with a boundary layer next to the surface.

The usual governing equations for sound propagation in a shear flow, using pressure and acoustic particle velocity, have singularities if either the mean velocity gradient becomes infinite or at a critical layer where the Doppler shifted frequency of wall vibration becomes zero. It is shown that the first of these singularities may be avoided by using the particle displacement as a wave variable in place of the particle velocity. Both singularities may be avoided by using the displacement impedance as a variable. The new formulation has enabled a list of properties of solutions at a critical layer to be compiled.

The sound radiation problem is solved by numerically integrating the governing equations for sound waves radiating away from the surface at each horizontal wave number, applying a boundary condition corresponding to the wave number spectrum of the wall vibration, and then using an inverse spatial Fourier transform to determine the radiated sound field.

The effect of the flow Mach number and boundary layer thickness on the radiation efficiency of individual wave number components, and the power and sound field radiated by a uniform piston vibrating in an otherwise rigid wall are considered. The model is validated by replicating analytic results for a uniform flow over a compact piston, an increase in sound power output and a convective amplification effect that increases the pressure upstream of the source and reduces the level downstream. It is shown that, as the boundary layer thickness is increased, the power output and convective amplification are reduced, and the sound field is further modified by refraction of upstream propagating sound away from the surface and by downstream channelling of sound in the boundary layer.

The model is used to investigate the performance of a flush mounted device in the wall that uses speed of sound propagation between a source and one or more receivers to determine properties of the flow. It is shown that by measuring propagation speed at two appropriate frequencies it is possible in principle to measure the free-stream Mach number, the boundary layer displacement thickness and the direction of the flow.

CONTENTS

Acknowledgements

Completing this study has taken a considerable amount of personal time and energy over a considerable number of years, and so completing it has required the support and patience of my family, my colleagues and sometimes my clients.

Firstly, thanks are due to my supervisor Professor Chris Morfey, who resolutely encouraged me on despite many trials along the way. His quiet determination to help me through this project is an example to all supervisors.

Secondly, thanks go to the many colleagues in ISVR, in both the Consultancy Unit and the academic department, who have provided moral support, paid fees or tolerated diversion of my energy away from the other things I could and should have been doing.

Thirdly, thanks are due to Mike Gill, Tony Stickland and Steve Whale at Gill Electronic R&D, and to Doug Greenwell, formerly of DERA, for introducing the flow measurement problem to me and giving permission to use test results from our joint consultancy report in this thesis. Without the focus of this interesting problem it is doubtful whether I would have succeeded in my studies.

Finally my love and thanks go to my wife Michèle for her support and encouragement, and apologies to her and to my daughters Naomi and Nathalie for all the things I have not done because I needed to complete this personal endeavour.

Symbols

x	coordinate direction parallel to the flow
y	coordinate direction transverse to the flow
z	coordinate direction away from the wall
z_0	particular z coordinate location
$\boldsymbol{U}$	mean flow velocity vector
$U(z)$	mean flow velocity component in the x direction
U0	free stream mean flow velocity
$M(z)$	mean flow Mach number
M0	free stream mean flow Mach number
ρ_0	unperturbed fluid density
c_0	speed of sound
δ	boundary layer thickness
δ_{99}	profile 99% thickness
δ_{disp}	boundary layer displacment thickness
δ_{mom}	boundary layer momentum thickness
δ_{ke}	boundary layer kinetic energy thickness
p	acoustic pressure
$\mathbf{u}$	acoustic particle velocity vector
u_x, u_y	acoustic particle velocity in the x and y directions
u_z	acoustic particle velocity in the z-direction
q	acoustic particle displacement in the z-direction
a	acoustic particle acceleration in the z-direction
χ	displacement impedance, p/q
β	displacement admittance, q/p
p_{init}	initial value for the acoustic pressure at the edge of the boundary layer $z = \delta$
q_{init}	initial value for the acoustic particle displacement at the edge of the boundary layer
f	frequency
ω	rotational frequency, $2\pi f$
λ	wavelength of sound, c_0/f
k_0	wave number, ω/c_0
k_x	wave number component in the x direction
k_y	wave number component in the y direction
k_z	wavenumber in the z direction in the region of uniform mean flow
$\overline{D}$	operator $\frac{\partial}{\partial t} + \mathbf{U}.\nabla$; after time and space Fourier transformations $\overline{D} = j(\omega - k_x U)$
z_{crit}	z-location of a critical layer, where $\overline{D} = 0$
ξ	normalized distance from the critical layer
L	computational domain size or path length over which a flow measurement is made
t_u, t_d	time of flight upstream or downstream for a non-dispersive pulse of sound
M_d	propagation Mach number of a wave

Figures

Chapter 1

1. INTRODUCTION AND OUTLINE OF CONTENTS

1.1 Aims and motivation

The sound field radiated into a fluid by a vibrating surface is well understood when the fluid is at rest, as discussed in textbooks such as Junger and Feit [1] and Pierce [2], or when there is a uniform flow parallel to the surface, as discussed by Morse and Ingard [3] and Dowling and Ffowcs Williams [4]. This thesis addresses the more complex problem of the sound field generated by a plane vibrating surface when the adjacent fluid has a non-uniform mean flow profile.

The major motivation for the study was a requirement to model the behaviour of an ultrasonic device for measuring properties of a boundary layer flow. The performance of the device itself is examined in Chapters 8 and 9. The early chapters concentrate on the formulation of the modelling problem, the development of tools for the analysis, and the development of a deeper understanding of how individual wave number components are radiated from the surface and propagate through the shear flow.

A second aim was an ability to predict the effect of a shear flow on the sound field radiated by a localised source at a wall. The sound field in the body of the fluid is not actually required for the purposes of modelling the flow-measuring device, although clearly an understanding of the characteristics of the overall sound field is useful. Chapters 5, 6 and 7, which deal with the power and pressure radiated away from the surface are thus partially motivated by a number of other aeroacoustic problems, such as the effect of shear flow on radiation from sources of aerodynamic noise and the active control of sound propagation in ducts. These other applications are mentioned incidentally at various points through the thesis and are summarised in Chapter 10.

1.2 Scope of the investigation

The mean flow considered in the study consists of a semi-infinite fluid flowing parallel to a surface, with a boundary layer next to the surface. The governing acoustic equations developed in Chapter 2 allow for a non-uniform mean density $\rho(z)$ and speed of sound

$c(z)$ away from the surface, although both quantities are taken to be constant in the remainder of the thesis. Potentially therefore, the model can be used to examine the effect of density and sound speed gradients through the boundary layer, such as occur for example at a heated wall, or in adiabatic flows at high subsonic Mach numbers.

The model is valid for boundary layers of arbitrary thickness to wavelength ratio, and some results are presented for shear layers up to ten wavelengths thick. The majority of results presented, however, are for boundary layers varying from zero to one wavelength thick since this covered the range of interest for the flow measurement problem.

The method developed here can be used to model sound radiation from any spatial distribution of surface vibration. Again however, because of the requirement to model the sound field produced by an ultrasonic transducer, the emphasis is on radiation from point sources and from pistons of finite size vibrating in an otherwise rigid surface.

1.3 Outline of contents

The analysis begins in Chapter 2 with a new derivation of the governing equations of sound propagation in a non-uniform parallel mean flow. It is shown that the second order differential equation obtained by Pridmore-Brown [5], can conveniently be left as two simultaneous first order equations, in two variables, which arise directly from the momentum and continuity equations for the fluid. Because the problem is homogeneous in directions parallel to the surface, the equations may be Fourier transformed with respect to the x- and y-coordinates. The solution in the z- direction (normal to the wall) is obtained via a numerical integration of the governing equations through the shear layer.

A number of alternative wave variables are considered in Chapter 2. The acoustic pressure is always used as one variable but, depending on circumstances, the best co-variable to use is the z-component of either the particle velocity, the particle displacement or the displacement impedance (pressure/displacement). If the mean flow velocity gradient becomes infinite, as for example at the wall an idealised turbulent boundary layer, the equations based on particle velocity are not well defined and the displacement or displacement impedance equations should be used instead. However, at some specific wave numbers, either when there is a critical layer present (i.e. a z-location where the Doppler shifted frequency of the source is

zero) or when there are channelled modes in the boundary layer, there are advantages for one or other of the displacement or displacement impedance wave variables.

A useful new result in Chapter 2 is the derivation of a first-order differential equation for the variation of the displacement impedance through the boundary layer. The pressure field can subsequently be calculated from another first-order equation, using the displacement impedance result, if required.

Chapter 2 concludes by summarising the general properties of solutions at a critical layer that may be used to verify numerical solutions obtained in Chapter 4. The list of properties includes new results that apply to acoustic solutions in any shear layer profile.

Chapter 3 describes some of the technicalities of the procedure for numerically integrating the governing equations through the boundary layer, given starting values that satisfy the radiation condition at the edge of the boundary layer. Various methods of obtaining the solution at a critical layer are compared. The chapter concludes with an assessment of which method works most consistently and accurately, and offers criteria for the choice of wave variables.

Outgoing acoustic disturbances generated in the fluid by particular wave number components in the surface are investigated in Chapter 4, with many interesting features of solutions in the wave number domain being demonstrated. This detailed analysis assists in the interpretation of spatial domain solutions in later chapters. The effects include refraction of upstream-propagating waves away from the surface, tunnelling of waves that are cut off at the surface but propagate in the exterior mean flow, and the channelling of downstream-propagating waves.

The radiation impedance and radiation efficiency of the surface are modified by the mean flow, and the effect on the power radiated by the surface at each wave number is considered in Chapter 5. This analysis prepares the way for predicting the power radiated by a piston in Chapter 7. A useful new result is that power flow away from the surface is conserved in a parallel shear flow, so that the power radiated to the far-field can be calculated at the surface rather than at the edge of the boundary layer.

Chapter 6 provides the formulation of the method for predicting the sound field radiated by a piston at the wall. The wall boundary condition is applied to give the pressure disturbance in the fluid at any z-location, caused by the vibration of the piston, as a function of wave numbers in the x- and y- directions. The pressure field in any plane $z = z_0$ is then given by an inverse Fourier transform into the (x,y) spatial domain. It is shown that inaccuracies in the solution can occur for a number of reasons, and methods of controlling these errors are discussed. Firstly, inaccuracies due to use of a discrete Fourier Transform, which may give rise to errors at coincidence and due to the effect of image sources, may be controlled by including damping in the model. Secondly, a problem of 'leakage' due to the asymmetry in the radiation impedance of the surface, arising from the asymmetrical effect of the mean flow, can be avoided by applying a Hanning or similar window function to the wave number spectrum of the source.

The effect of a boundary layer on the pressure field and the power radiated by a piston is described in Chapter 7. By comparing predictions for a thin boundary layer with an analytical benchmark for uniform flow it is shown that the variation of power radiated by the source as a function of flow Mach number is correctly predicted. The model is also shown to correctly predict the effect of convective amplification on the radiated pressure field; an increase in the pressure level upstream of the source and a reduction in the level downstream.

Having validated the model for a near-uniform flow the effect of increasing the thickness of the boundary layer is then demonstrated; the power output of the source is gradually reduced to that of a source in zero flow, and the pressure field is modified by a reduction in the effect of convective amplification and a growing influence of boundary layer refraction, with channelling of sound downstream and a shadow zone upstream. The spatial characteristics of the sound field are thus shown to be a strong function of boundary layer thickness.

In Chapter 8 the model is used to predict the behaviour of a flow measuring device, in which a source transducer flush-mounted in the wall radiates sound into the flow, and a similar receiver transducer measures the amplitude and phase of the sound field at some point on the wall downstream of the source. It is shown that when the boundary layer is thin on the wavelength scale the system measures the free-stream flow velocity, but that when the

boundary layer thickness is greater than $1/10^{th}$ of a wavelength the apparent flow velocity measured by the system is significantly reduced.

This dependence of 'measured' flow velocity on the ratio of boundary layer thickness to wavelength is shown to be a useful effect which could be used to derive a measure of both the free stream flow velocity and the boundary layer displacement thickness. Furthermore, the model demonstrates that a system using a single source and two receivers, measuring phase speed at two appropriate frequencies, could in principle measure free stream flow velocity, boundary layer displacement thickness and flow direction.

In Chapter 9 the model is compared with some basic measurements that were performed on a prototype instrument under a consultancy contract with Gill Electronics R&D and DERA (now QinetiQ). Quantitative comparisons between the model and the experiments can be made for one of the test conditions; agreement between measurements and predictions for this case is found to be very good. The trends in other data, for which quantitative comparisons cannot be made without detailed aerodynamic modelling, agree qualitatively with the predictions of the model.

Chapters 8 and 9 together demonstrate the feasibility of a new type of device for carrying out aerodynamic measurements in boundary layers. This method could complement other methods such as hot wire anemometry and Laser Doppler Anemometry, for which measurements close to a surface can be problematic. There are also possibilities for the application of such a system to monitor flow over the surfaces of aircraft, ships, etc.

The overall conclusions of the study are presented in Chapter 10, together with a summary of possible extensions to the work presented here and other applications for the derived governing equations and the solution methodology.

1.4 Claim to originality

A primary aim of this thesis has been to describe a method for predicting the behaviour of a novel flow-measuring device, and so the work presented in Chapters 8 and 9 is clearly original. However, the problems and issues that were resolved in developing the

mathematical model mean that many other chapters also contain significant new results. This section summarises the main original aspects of the study.

Chapter 2 considers a range of wave variables and new governing equations and uses these to generate a list of properties of solutions at a critical layer, summarised in Section 2.5, that must be satisfied irrespective of the characteristics of the mean flow profile. A few of the properties listed may be seen in previously published results for specific flow profiles, but most of the properties and the generalisation to arbitrary flow given here are entirely new. It has been found that continuity of particle displacement is not satisfied across a critical layer, a fact that should also be taken into consideration when modelling sound transmission through a shear layer of vanishing thickness (a vortex sheet).

Of the equations produced in Chapter 2, the new governing equation for the displacement impedance in a parallel mean flow, (2.32a), and the partially coupled equation for pressure given in (2.32b), are particularly useful since they provide both a means of finding solutions for all mean flow profiles, even when a critical layer is present and a simpler equation for determining the radiation impedance of a surface under a shear flow. There may also be potential benefits in the fact that the second order differential equation derived by Pridmore Brown has been reduced to two first order equations that may be solved consecutively, and which do not require the evaluation of the mean velocity derivative.

The analysis in Section 3.3, using equations (2.32a,b) to examine the behaviour of solutions of the governing equations in the vicinity of a critical layer, has provided an improved comparison of the accuracy of two ways of integrating around the singularity. The fact that it was difficult to make the numerical integrals converge to a correct solution, with the properties identified analytically in section 2.5, may be useful in other similar areas of research. This is particularly the case for the complex ω method that is generally preferred because it is simple to implement.

Chapters 4 and 5 include a number of new results on the radiation into a shear flow of specific wave number components in a vibrating surface. The solutions for pressure plotted in Section 4.2, although showing features that might have been expected from previous studies of sound propagation in inhomogeneous media, are nonetheless new results that are

specific to sound radiation through a parallel shear flow and have not been presented elsewhere.

A valuable new result is demonstrated in Section 5.1, a proof that sound power is conserved when acoustic energy is transmitted across a parallel shear flow. This fact has enabled a well-defined radiation efficiency for the surface to be evaluated as a function of wave number and boundary layer thickness; it is plotted in figure 5.4. Previously only results for uniform flow were known, and figure 5.4 shows that a boundary layer can have a strong effect on the efficiency with which a vibrating surface can radiate sound upstream.

Chapter 6 describes an extension to the standard method of using the spatial Fourier transform in x and y to solve sound radiation problems. Such techniques are most often applied where an analytical solution in the z-direction is known, for example for radiation into a uniform flow, and no publications have been found where an integral in the z-domain is also required. The z-integral made the problem far more demanding numerically, necessitating use of discrete Fourier transforms with the consequences discussed in Sections 6.2 and 6.3. Because of the combined requirement of limiting the wave number range of the Fourier transforms and predicting the response at the surface and near the source, the problem of 'leakage' due to the asymmetry of the flow became apparent, and was resolved by a novel application of windowing methods as discussed in Section 6.5. This problem must have occurred to a lesser extent in publications dealing with sound radiation into uniform flow, affecting convergence of the transform integrals, but has not previously been noted.

The numerical predictions of the sound fields radiated by a vibrating piston under a boundary layer presented in Chapter 7 are all new results which, besides being interesting in their own right, also provide useful insight into how far the assumptions of a thin boundary layer and a compact source size used in analytical solutions remain accurate.

Finally, Chapters 8 and 9 present the results from the flow meter study. The use of ultrasound to measure flow in ducts is well established, the general concept of using ultrasound to measure flow over a surface originated at QinetiQ, and the hardware and data processing techniques for doing so were developed by Gill Electronics R&D, so that no claim to originality in these areas is made here. The originality in the work presented in this thesis

lies in the development and application of a novel mathematical model and the validation against the experimental data.

A specific new result in Chapter 8, that arose from the mathematical modelling work, is that measuring the frequency dependence of sound propagation speed in a boundary layer flow may potentially be used to determine both free-stream flow velocity and boundary layer displacement thickness.

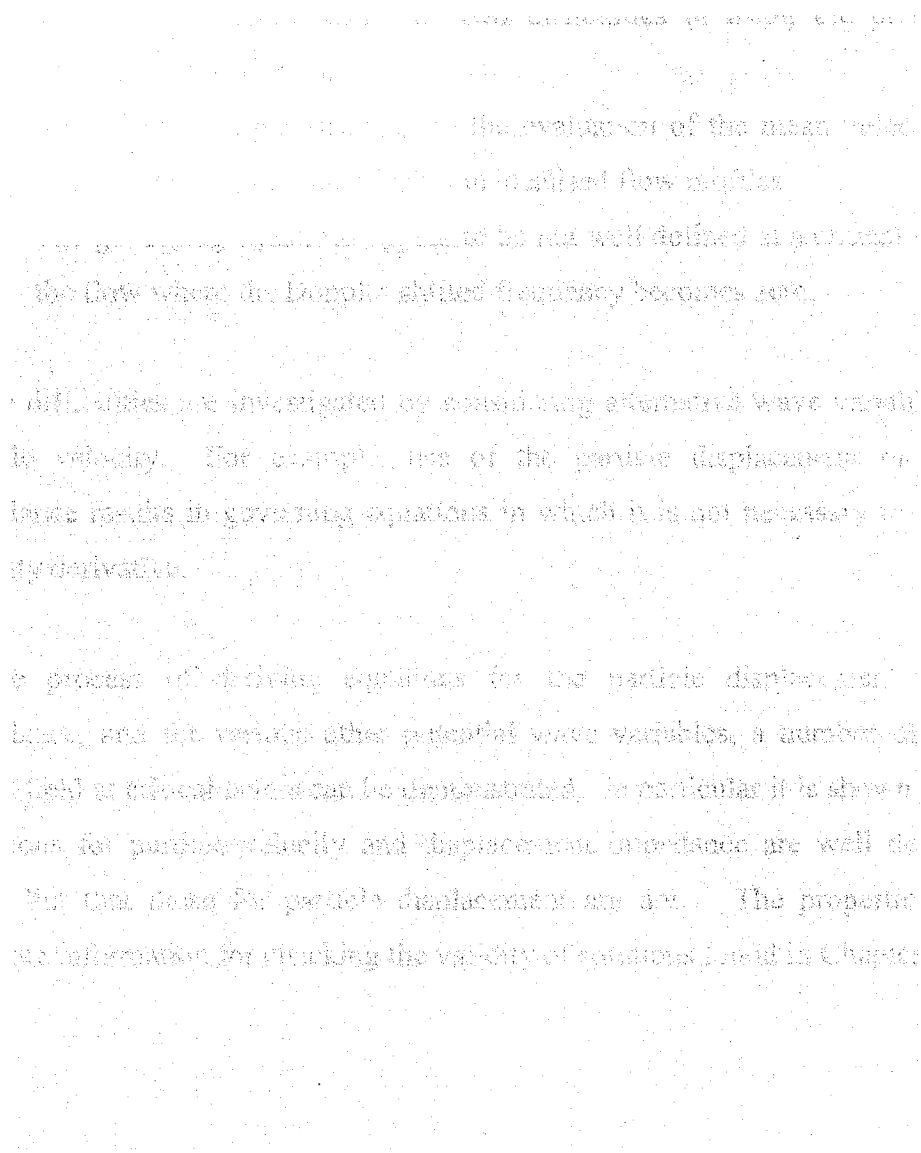

Chapter 2

2. THEORY OF WAVE TRANSMISSION IN A PARALLEL SHEAR FLOW USING MODIFIED WAVE VARIABLES

This chapter investigates the governing equations for sound propagation in a parallel shear flow. These equations are most commonly expressed either as a second order differential equation in the acoustic pressure, or as coupled first order equations for the acoustic pressure and particle velocity.

In particular circumstances there are two difficulties in using the pressure and particle velocity as the wave variables:

- the governing equations require the evaluation of the mean velocity derivative, and this is not always defined for some idealised flow profiles.
- The governing equations appear to be not well defined at a critical layer, a location in the flow where the Doppler shifted frequency becomes zero.

These difficulties are investigated by considering alternative wave variables in place of the particle velocity. For example, use of the particle displacement or the displacement impedance results in governing equations in which it is not necessary to evaluate the mean velocity derivative.

In the process of deriving equations for the particle displacement and displacement impedance, and for various other potential wave variables, a number of properties of the sound field at critical layers can be demonstrated. In particular it is shown that the governing equations for particle velocity and displacement impedance are well defined at a critical layer, but that those for particle displacement are not. The properties derived provide valuable information for checking the validity of solutions found in Chapter 4.

2.1 Review of literature

2.1.1 Governing acoustic equations in a parallel shear flow

An equation for sound propagation in a parallel shear flow was published by Pridmore-Brown in 1958 [5]. This equation, given in (2.10) on page 13, is a second order differential equation for the pressure distribution as a function of coordinate z, for a specified value of wave number in the x- and y-directions, (k_x,k_y). The coordinate system is shown in figure 2.1.

Because the effect of shear flow is an important issue for the study of sound transmission and attenuation in ducts the Pridmore-Brown equation has formed the basis for numerous subsequent studies, many of which are listed by Eversman [6]. This review, which focuses on models applicable to aero engines, outlines the derivation of an equation in 3-D cylindrical coordinates that is similar to Pridmore-Brown's 2-D equation

The first difficulty noted above for the Pridmore-Brown equation, and the equation given by Eversman, is that it is necessary to evaluate the mean velocity derivative dU/dz at all points in the flow. This becomes infinite at the wall for some boundary layer profiles such as the $1/7^{th}$ power law profile used to model turbulent boundary layers. Pridmore-Brown used an asymptotic method to find the solution at the wall for this boundary layer profile. Others, for example Agarwal and Bull [7], have used modified boundary layer profiles, representative of the viscous boundary sub-layer near the wall, to provide a profile whose derivative can be evaluated at the wall.

An alternative approach is to use particle displacement as a wave variable in place of the particle velocity. This method, described in Section 2.3 and used in equation (2.14), leads to governing equations that do not involve the mean velocity derivative.

The use of the particle displacement as an acoustic variable has recently been described by Peyret & Elias [14], who used an equation originated by Galbrun [15] as the basis of a finite element model of sound propagation in a duct carrying a sheared mean flow. It appears that the Galbrun equation does not require mean-flow derivatives to be evaluated, although the boundary layer used by Peyret & Elias was taken to have a quarter-sinusoid profile, whose gradient is in any case finite at the wall, so that this issue was not discussed.

The Galbrun technique has also been used in recent work to be published by Gabard et al [16], to develop a finite element model of sound propagation in a flexible walled duct carrying a shear flow. The mixed pressure-displacement form of equations chosen by them is similar to equation (2.14) derived below. Gabard uses the model developed by Pagneux and Auregan [17] as a reference to check their solutions. This paper models sound propagation in the duct using the Pridmore-Brown equation, and uses a continuity of particle displacement boundary condition to couple the acoustic equation to the equation for flexural vibration of the wall.

Although there is a wealth of literature on alternative methods for modelling the effect of stratified or generally inhomogeneous media - see for example Brekhovskikh & Godin [18] and the field of ocean acoustics [19] - the methods used are not generally applicable to the shear flow problem. Ray acoustics has been used to model sound propagation in non-uniform flow [20], but this is not an appropriate method for modelling a boundary layer whose thickness may be comparable with the wavelength of sound.

2.1.2 Critical layers

Besides the issue of mean velocity derivative, a second difficulty with the Pridmore-Brown equation, (2.10), and related equations is that, for some values of axial wave number k_x, the factor $\overline{D} = j(\omega - k_x U)$, in the denominator of the second term, can go to zero at some point through the boundary layer, a so-called critical layer. In that case the equation is not well defined unless the numerator is also zero.

The values of k_x for which a critical layer occurs are not generally of interest in duct acoustics since these waves are propagating sub-sonically and are therefore cut-off in the duct. For example, the potential for difficulties can be seen in the duct termination boundary conditions used by Peyret & Elias [14], but the issue of critical layers is not discussed.

Critical layers are an issue for other problems of sound radiation and transmission in a shear flow however, for example in modelling sound generation in jet shear layers [8, 9, 10, 11], and sound transmission through shear layers [12, 13]. Tam & Morris [9] consider two ways of integrating around the singularity in their equations and Campos et al [12] use a Frobenius

expansion to obtain solutions in a region around the critical layer. These techniques are considered in depth in Section 2.4.1 and are compared with the method of solution derived here.

2.2 Derivation of the governing equations using pressure and particle velocity as wave variables

This section outlines the derivation of the governing equations for sound propagation in a steady parallel inviscid shear flow using pressure and particle velocity, as originally described by Pridmore-Brown [5].

The particular case of interest is the flow shown in figure 2.1, in which a parallel shear flow (idealised boundary layer) separates a surface at $z = 0$ from uniform flow in the x-direction in the region $\delta<z<\infty$. The undisturbed flow field is uniform in any plane z = constant, and its pressure is constant. Figure 2.1 also shows a 2-D or 3-D source radiating into the flow, the problem which is studied from Chapter 6 onwards.

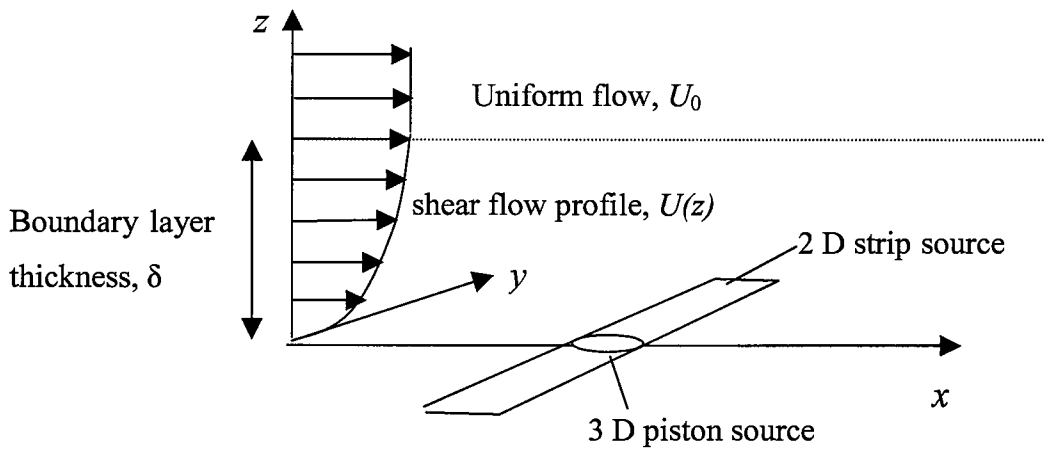

Figure 2.1 boundary layer flow in the x-direction over a surface at z=0 with a piston or strip source

The linearized momentum and continuity equations in vector notation, for small amplitude perturbations of the flow in figure 2.1, are [21,22,23]

$$\rho_0 \left(\overline{D}\,\mathbf{u} \;+\; (\mathbf{u}\cdot\nabla)\mathbf{U}\right) \;=\; -\nabla p \tag{2.1}$$

$$\frac{1}{\rho_0 c_0^{\,2}}\,\overline{D}\,p \;=\; -\nabla\cdot\mathbf{u} \tag{2.2}$$

where $\mathbf{U}$ is the mean velocity vector, $\mathbf{u}$ is the acoustic particle velocity vector with components (u_x, u_y, u_z), p is acoustic pressure, ρ_0 is the local fluid density and c_0 is the local speed of sound. $\overline{D}$ is the operator $\frac{\partial}{\partial t} + \mathbf{U}.\nabla$, and subscript 0 denotes unperturbed values.

Throughout this chapter the density ρ_0 and speed of sound c_0 are assumed to be functions of z, so that the equations derived are as general as possible. The later discussion, from Chapter 3 onwards, is based on the assumption that the density and speed of sound are constant through the boundary layer. Including the effect of non-uniform density and sound speed in the numerical solution is straightforward.

Equation (2.1) is a vector equation with three components and so (2.1) and (2.2) together provide a set of four simultaneous equations that may be solved for the four acoustic variables u_x, u_y, u_z and p.

Given that the mean flow has the form shown in figure 2.1, i.e. $\mathbf{U} = (U(z), 0, 0)$, equations (2.1) and (2.2) are homogeneous in the three time/space variables t, x, and y and may be Fourier transformed to the frequency / wave number variables ω, k_x and k_y. The convention used for the transform is that solutions of the following form are sought:

$$p(x,y,z,t) = \tilde{p}(k_x,k_y,z)e^{j(\omega t - k_x x - k_y y)} \tag{2.3}$$

Using the same convention for the other acoustic variables the Fourier transform of equations (2.1) and (2.2) leads to the following four equations in transformed variables. The ~ denoting a transformed variable has been dropped for clarity.

$$\rho_0\left(\overline{D}\,u_x + u_z\frac{dU}{dz}\right) = jk_x p \tag{2.4}$$

$$\rho_0\,\overline{D}\,u_y = jk_y p \tag{2.5}$$

$$\rho_0\,\overline{D}\,u_z = -\frac{\partial p}{\partial z} \tag{2.6}$$

$$\frac{1}{\rho_0 {c_0}^2}\,\overline{D}\,p = jk_x u_x + jk_y u_y - \frac{\partial u_z}{\partial z} \tag{2.7}$$

where the Fourier transform of $\overline{D}$ is given by

$$\overline{D} = j(\omega - k_x U) \tag{2.8}$$

Using (2.4) and (2.5) to eliminate u_x and u_y from (2.7), and leaving (2.6) unchanged, leads to the following coupled equations in u_z and p:

$$\frac{\partial u_z}{\partial z} = -\frac{1}{\rho_0\overline{D}}\left(\left(\frac{\overline{D}^2}{{c_0}^2} + {k_x}^2 + {k_y}^2\right)p + jk_x\rho_0 u_z\frac{dU}{dz}\right) \tag{2.9a}$$

$$\frac{\partial p}{\partial z} = -\rho_0\overline{D}u_z \tag{2.9b}$$

Combining the z derivative of (2.9b) with (2.6) and (2.9a) to eliminate u_z and $\partial u_z/\partial z$ leads directly to the second order differential equation in p derived by Pridmore-Brown:

$$\left(\frac{\overline{D^2}}{{c_0}^2} + k_x^2 + k_y^2\right)p + \left(\frac{1}{\rho_0}\frac{d\rho_0}{dz} - 2j\frac{k_x}{\overline{D}}\frac{dU}{dz}\right)\frac{\partial p}{\partial z} - \frac{\partial^2 p}{\partial z^2} = 0 \tag{2.10}$$

As already noted in Section 2.1, both the coupled first order equations (2.9) and the second order differential equation (2.10) are difficult to solve numerically for some commonly assumed profiles, such as the $1/7^{th}$ power law profile used to define the boundary layer for

turbulent flow over a flat plate, because the velocity gradient $\frac{dU}{dz}$ becomes infinite at the wall. This difficulty may be avoided by changing variables as shown in Section 2.3.

The second complication discussed in the previous section is that equations (2.9a) and (2.10) appear to be not well defined when $\overline{D} = 0$. This condition occurs at the so-called critical layer where the Doppler shifted frequency vanishes [12]. From (2.8) it may be seen that this happens when $\omega = k_x U$, i.e. when $k_x = \frac{kc_0}{U}$. Since U varies from zero at the wall to U_0 at the edge of the boundary layer and into the region of uniform flow, it follows that $\overline{D}$ will be zero at some point through the boundary layer for all values of k_x such that $\frac{k_x}{k} > \frac{c_0}{U_0}$.

The solution of the governing equations when a critical layer is present is discussed in Sections 2.4 and 3.3. In Section 2.4 it is shown that $\frac{dp}{dz}$ and the bracketed term in equation (2.9a) are both zero at a critical layer, and furthermore that $\frac{1}{\overline{D}}\frac{dp}{dz}$ and $\frac{du}{dz}$ remain finite there, thus both equations (2.10) and (2.9a) remain finite at a critical layer. The main problem with using these equations therefore, besides the difficulty of evaluating numerically the ratio of two terms which both tend to zero, is that $\frac{dU}{dz}$ can be infinite at the wall for some flow profiles.

In subsonic flow critical layers occur only when $k_x > k$, which means that the waves are travelling subsonically in the x-direction. Subsonic axial phase speeds are not often considered in sound transmission problems in duct acoustics since these represent cut-off modes which decay rapidly with axial distance, although Swinbanks [42] shows however that wave numbers with a critical layer represent hydrodynamic disturbances convected by the fluid. It will be seen in Chapter 6 that these wave numbers are potentially important for sound radiation problems, especially at high free-stream Mach numbers and near the boundary wall.

2.3 Alternative equations using pressure and particle displacement as wave variables

A simpler set of governing equations may be obtained by expressing (2.9) in terms of the variable

$$q = \frac{u_z}{\overline{D}} \tag{2.11}$$

Morse and Ingard [3], see page 736, show that q is the normal component of particle displacement.

Differentiating (2.11) and (2.8) with respect to z gives

$$\frac{\partial q}{\partial z} = \frac{1}{\overline{D}^2}\left(\frac{\partial u_z}{\partial z}\overline{D} - u_z\frac{\partial \overline{D}}{\partial z}\right) \tag{2.12}$$

where

$$\frac{\partial \overline{D}}{\partial z} = -jk_x\frac{dU}{dz}. \tag{2.13}$$

Substituting for $\frac{\partial u_z}{\partial z}$ and $\frac{\partial \overline{D}}{\partial z}$ in equation (2.12) using (2.9a) and (2.13) leads to equation (2.14a) below. Equation (2.14b) is obtained by substituting $\overline{D}q$ for u_z in (2.9b).

$$\frac{\partial q}{\partial z} = -\frac{1}{\rho_0\overline{D}^2}\left(\frac{\overline{D^2}}{{c_0}^2} + {k_x}^2 + {k_y}^2\right)p \tag{2.14a}$$

$$\frac{\partial p}{\partial z} = -\rho_0\overline{D}^2 q \tag{2.14b}$$

In this form of the equations the mean velocity gradient $\frac{dU}{dz}$ has been eliminated. This means that a solution for p and q may be found for all values of z, even where the gradient is infinite in the assumed boundary layer flow profile.

Equation (2.14a), however, is not well defined at a critical layer, where $\overline{D} = 0$, unless p=0 there. The variable q given in (2.11) may also be not well defined.

2.4 Alternative forms of solution and other wave variables for use at critical layers

2.4.1 Review of other published methods

In order to solve the governing differential equations for all values of z it is necessary to integrate the equations through the boundary layer. Both forms of equation so far presented – those based on (p,u_z) and on (p,q) - are undefined or difficult to evaluate at a critical layer, and so another method for integrating through a critical layer is sought.

Tam & Morris [9] proposed two methods for integrating around such a singularity: one can either use a complex value for the frequency, or allow the variable z to become complex in the region of the singularity. These methods are discussed further in Section 3.3; they form the basis for the numerical solution procedure eventually used in this study.

An alternative method has been investigated by Campos et al [12]. They obtained solutions in the region of a critical layer by using the Frobenius method to find a polynomial expansion of the solution in the variable ξ, the normalized distance from the critical layer. The method can be used to find solutions for any specified flow profile. The solutions take the form:

$$\Phi_\sigma(\xi) = \xi^\sigma \sum_{n=0}^{\infty} a_n(\sigma)\xi^n \tag{2.15}$$

where the index, σ, and the coefficients $a_n(\sigma)$ have to be determined for each specific problem.

Campos shows that for the case of a linear flow profile there are two linearly independent solutions, corresponding to $\sigma = 0$ and $\sigma = 3$. For both solutions $a_n = 0$ when n is odd and this means that Φ_0 is an even function of ξ whereas Φ_3 is an odd function of ξ. From equation (2.15) it may be seen that the two solutions have the following properties at the critical layer, ξ=0.

σ=0 solution:

$$\Phi_0 = a_0(0), \quad \frac{d\Phi_0}{d\xi} = 0, \quad \frac{d^n\Phi_0}{d\xi^n} = \begin{matrix} a_n(0) & for \quad n = 2,4,6..... \\ 0 & for \quad n = 3,5,7..... \end{matrix} \tag{2.16a}$$

σ=3 solution:

$$\Phi_3 = 0, \quad \frac{d\Phi_3}{d\xi} = 0, \quad \frac{d^n\Phi_3}{d\xi^n} = \begin{matrix} 0 & for \quad n = 2,4,6..... \\ a_{n-3}(3) & for \quad n = 3,5,7..... \end{matrix} \tag{2.16b}$$

The first derivatives of both solutions are zero at the critical layer and this may be shown to be the case for any finite and continuous solution of the Pridmore-Brown pressure equation, (2.10), for any arbitrary flow profile, by considering the behaviour of the most singular terms in the limit as ξ tends to zero.

2.4.2 General properties in the critical layer region

Assuming that for small ξ the pressure has an asymptotic dependence $p = O(\xi^{\alpha_1})$, then $\frac{\partial p}{\partial z} = O(\xi^{\alpha_2})$ where $\alpha_2 \le \alpha_1 - 1$ and $\frac{d^2 p}{dz^2} = O(\xi^{\alpha_3})$ where $\alpha_3 \le \alpha_2 - 1$.

Since $\alpha_3 < \alpha_2 < \alpha_1$, the term $\frac{\partial^2 p}{\partial z^2}$ appears to be most singular term of (2.10). It is possible however for the term $2j\frac{k_x}{\overline{D}}\frac{dU}{dz}\frac{\partial p}{\partial z}$ to have the same order as $\frac{\partial^2 p}{\partial z^2}$ since $\overline{D} = O(\xi)$ inside the boundary layer.

However, noting that

$$\frac{\partial}{\partial z}\left(\overline{D}^2\frac{\partial p}{\partial z}\right) = 2\overline{D}\frac{\partial \overline{D}}{\partial z}\frac{\partial p}{\partial z} + \overline{D}^2\frac{\partial^2 p}{\partial z^2} = \overline{D}^2\left(-2j\frac{k_x}{\overline{D}}\frac{dU}{dz}\frac{\partial p}{\partial z} + \frac{\partial^2 p}{\partial z^2}\right), \tag{2.17}$$

the Pridmore-Brown equation may be rewritten

$$\left(\frac{\overline{D^2}}{c_0^2}+k_y^2+k_y^2\right)p \;+\; \frac{1}{\rho_0}\frac{d\rho_0}{dz}\frac{\partial p}{\partial z} \;-\; \frac{1}{\overline{D}^2}\frac{\partial}{\partial z}\left(\overline{D}^2\frac{\partial p}{\partial z}\right) \;=\; 0. \qquad (2.18)$$

In this form the last term is always the most singular term and hence must tend to zero at the critical layer. For this to be the case $\frac{\partial p}{\partial z}$ must be $O(\xi)$ or higher, and thus $\frac{\partial p}{\partial z}=0$ at the critical layer. This is a useful result that will be used in the next section to derive further information about solutions at critical layers.

2.4.3 Governing equations for other wave variables

The methods used by Tam & Morris [9] and by Campos [12] provide two potential ways of solving the governing equations in the region of a critical layer, but alternative ways of integrating through the layer explicitly by using other wave variables are now considered.

The properties of the Campos solutions for the linear flow profile (2.16), and also comparison of equations (2.9) and (2.14), suggest that it may be useful to consider higher derivatives of particle velocity, or ratios of particle displacement and pressure, as potential wave variables. By deriving the appropriate differential equations it is possible to prove a number of properties of the solution in the region of the critical layer. These properties are useful for checking the validity of solutions obtained by numerical integration and are summarised in the next section.

2.4.3.1 Particle acceleration

By analogy with equation (2.11) the particle acceleration in the z direction is given by

$$a \;=\; \overline{D}u_z \qquad (2.19)$$

Differentiating (2.19) with respect to z gives

$$\frac{\partial a}{\partial z} \;=\; \frac{\partial u_z}{\partial z}\overline{D} \;+\; u_z\frac{\partial \overline{D}}{\partial z} \qquad (2.20)$$

Substituting for $\frac{\partial u_z}{\partial z}$ and $\frac{\partial \overline{D}}{\partial z}$ using equations (2.9a) and (2.13) leads to equation (2.21a) below. Equation (2.21b) is obtained by substituting for u_z in (2.9b) using (2.18) .

$$\frac{\partial a}{\partial z} = -\frac{1}{\rho_0}\left(\frac{\overline{D^2}}{c_0^{\,2}} + k_x^{\,2} + k_y^{\,2}\right) p - 2jk_x \frac{a}{\overline{D}} \frac{dU}{dz} \tag{2.21a}$$

$$\frac{\partial p}{\partial z} = -\rho_0 a \tag{2.21b}$$

For equation (2.21a) to be suitable for use at the critical layer it is necessary that $\frac{a}{\overline{D}}$ remains finite. Because $\frac{\partial p}{\partial z} = 0$ at the critical layer, it follows from (2.21b) that a is also zero there. Since both a and $\overline{D}$ tend to zero at the critical layer, L'Hopital's rule gives that

$$\lim_{z \to z_{crit}} \frac{a}{\overline{D}} = \lim_{z \to z_{crit}} \frac{\partial a / \partial z}{\partial \overline{D} / \partial z} \tag{2.22}$$

Multiplying both sides of (2.22) by $\frac{\partial \overline{D}}{\partial z}$ and substituting using (2.13), gives

$$\lim_{z \to z_{crit}} \left(-jk_x \frac{dU}{dz} \frac{a}{\overline{D}}\right) = \lim_{z \to z_{crit}} \frac{\partial a}{\partial z} \quad . \tag{2.23}$$

Using (2.19) and (2.21a) and noting that $\overline{D} = 0$ at $z = z_{crit}$, this means that

$$-jk_x \frac{dU}{dz} u(z_{crit}) = \lim_{z \to z_{crit}} \frac{\partial a}{\partial z} = \frac{1}{\rho_0}(k_x^{\,2} + k_y^{\,2}) p(z_{crit}) \tag{2.24}$$

Because $p(z_{crit})$ is finite, (2.24) shows that $u(z_{crit})$ is also finite and hence, from (2.19) $\frac{a}{\overline{D}}$ remains finite. This proves that equation (2.21a) is well defined at the critical layer.

Although equations (2.21a,b) potentially form a well defined set of equations, so that particle acceleration could be used as a variable to obtain solutions for all values of z, the fact that (2.21a) involves the mean velocity derivative $\frac{dU}{dz}$ is inconvenient and alternative variables are considered in the next section.

First however, the issue of whether equations (2.9a) and (2.10) remain finite at a critical layer will be resolved. From equation (2.4) it is apparent that the bracketed term in (2.9a) is zero at a critical layer, thus $\frac{du_z}{dz}$ is the ratio of two terms which tend to zero there.

Applying L'Hopital's rule to equation (2.9a) gives

$$\lim_{z\to z_{crit}} \frac{du_z}{dz} = \lim_{z\to z_{crit}} \frac{\frac{d}{dz}\left((\frac{\overline{D}^2}{c_0^2} + k_x^2 + k_y^2)p + jk_x\rho_0 u_z \frac{dU}{dz} \right)}{\frac{d}{dz}\left(\rho_0 \overline{D}\right)} \tag{2.25}$$

Taking ρ_0 and c_0 to be constant, using the facts that $\overline{D} = 0$ and $\frac{dp}{dz}$ at a critical layer, and using (2.24), gives

$$\lim_{z\to z_{crit}} \frac{du_z}{dz} = \frac{-j(k_x^2 + k_y^2)p\frac{d^2U}{dz^2}}{k_x\rho_0\left(\frac{dU}{dz}\right)^2} \tag{2.26}$$

From (2.26), and since $k_x > 0$ when a critical layer is present, it is apparent that $\frac{du_z}{dz}$ tends to a finite limit and thus u_z must be finite at the critical layer. Furthermore, equation (2.9b) together with (2.24) shows that

$$\frac{1}{\overline{D}}\frac{\partial p}{\partial z} = -\rho_0 u_z = \frac{-j(k_x^2+k_y^2)p}{k_x \frac{dU}{dz}} \tag{2.27}$$

and so the Pridmore Brown equation, (2.10), is also well defined at a critical layer

2.4.3.2 Admittance and impedance

Useful equations may be obtained by considering the displacement impedance χ, and the displacement admittance β, defined respectively by:

$$\chi(k_x,k_y,z) = \frac{p(k_x,k_y,z)}{q(k_x,k_y,z)} \tag{2.28}$$

$$\beta(k_x,k_y,z) = \frac{q(k_x,k_y,z)}{p(k_x,k_y,z)} \tag{2.29}$$

Differentiating equations (2.28) and (2.29) and substituting using (2.14) it is easy to show that χ and β must satisfy the following equations

$$\frac{\partial \chi}{\partial z} = A\chi^2 - B \tag{2.30}$$

$$\frac{\partial \beta}{\partial z} = B\beta^2 - A \tag{2.31}$$

where $A = \frac{1}{\rho_0 \overline{D}^2}\left(\frac{\overline{D^2}}{c_0^2} + k_x^2 + k_y^2\right)$ and $B = \rho_0 \overline{D}^2$.

Since A is infinite at z_{crit}, as are q and β, so equation (2.31) is not useful in the critical layer problem. It has been included here as it is useful for determining modified boundary conditions in soft-walled ducts as mentioned in Chapter 10.

Equation (2.30) is useful for the critical layer problem however, as will be shown below. It has the advantage that it is an independent equation in the slowly varying (see plots in Chapter 4) parameter χ and is therefore computationally economical. It does not however

provide all the information required to explicitly calculate p and either q or u_z and so it is necessary to also use (2.14b) as a supplementary equation.

Equation (2.30) is independent of p and is written out in full in (2.32a). Equation (2.14b) must be re-written by substituting for q using (2.28) to give equation (2.32b).

$$\frac{d\chi}{dz} = \frac{1}{\rho_0}\left(\frac{\overline{D^2}}{{c_0}^2} + {k_x}^2 + {k_y}^2\right)\left(\frac{\chi}{\overline{D}}\right)^2 - \rho_0 \overline{D}^2 \tag{2.32a}$$

$$\frac{\partial p}{\partial z} = -\rho_0 \overline{D}^2 \frac{p}{\chi} \tag{2.32b}$$

Equation (2.32a) is well defined at the critical layer since $\frac{\chi}{\overline{D}} = \frac{p}{u_z}$ and both p and u_z are finite there. Also, by substituting (2.24) into (2.32a) and allowing $\overline{D}$ to tend to zero, it is easy to show that

$$\lim_{z \to z_{crit}} \frac{\partial \chi}{\partial z} = \frac{-k_x^2}{({k_x}^2 + {k_y}^2)} \rho_0 \left(\frac{dU}{dz}\right)^2 \tag{2.33}$$

Equations (2.32a,b) have the form required; they are well defined and, although both χ and $\overline{D}$ are zero there, remain finite at the critical layer. They have the advantage over (2.21a,b) that it is not necessary to calculate the mean velocity derivative $\frac{dU}{dz}$.

2.5 Summary of solution properties at a critical layer

This section summarises the information about solutions at the critical layer that have been demonstrated in the previous sections, the only requirement being that the solution be finite and continuous at the critical layer.

- By re-writing the Pridmore-Brown equation as (2.18) it has been shown that $\frac{\partial p}{\partial z} = 0$ at the critical layer.

- Equation (2.21b) shows that the particle acceleration a is zero at z_{crit}, and equations (2.24) and (2.21a) may then be used to show that $\frac{a}{D}$ and $\frac{\partial a}{\partial z}$ remain finite there.
- Equation (2.24) shows that u_z is finite and that $\frac{p(z_{crit})}{u(z_{crit})} = \frac{-jk_x}{(k_x^2 + k_y^2)} \rho_0 \frac{dU}{dz}$
- Equation (2.26) shows that $\frac{\partial u_z}{\partial z}$ remains finite at a critical layer, and hence so does u_z.
- From (2.24) and (2.14a) it may be deduced that q and $\frac{\partial q}{\partial z}$ become infinite.
- Since p is finite but q is infinite, it follows that χ is zero at the critical layer. Furthermore, $\frac{\partial \chi}{\partial z} = \frac{-k_x^2}{(k_x^2 + k_y^2)} \rho_0 \left(\frac{dU}{dz}\right)^2$ there and is thus real valued.
- It will be seen in Section 3.1 that p and χ always have real initial values at the edge of the boundary layer when a critical layer is present. Since the coefficients of (2.32a) and (2.32b) are all real valued functions of z, and $\frac{\partial p}{\partial z}$ and $\frac{\partial \chi}{\partial z}$ have been shown to be real valued at the critical layer, it follows that p and χ are real valued everywhere.
- The ratio $p/q = \chi$ passes through zero so, providing p is non-zero, q must change sign across the layer. It may be concluded that the commonly assumed boundary condition of continuity of particle displacement across a thin boundary layer [3] does not apply when the boundary layer contains a critical layer.

2.6 Conclusions from Chapter 2

New differential equations for acoustic propagation in a parallel shear flow have been derived, as shown in (2.14a,b) and (2.32a,b). These equations are both equivalent to the Pridmore-Brown equation, whether expressed as the second order equation (2.10) or in the form of coupled first order equations as in (2.9a,b), and will provide the same solutions.

The new equations based on displacement impedance, (2.32), have the advantage that they are well defined at all z locations, irrespective of boundary layer profile and whether a critical

layer is present. A disadvantage of using displacement impedance will be noted in Chapter 4 since this variable can become infinite when channelled boundary layer modes are present.

In relation to the two difficulties noted at the start of this chapter the utility of the variables considered may be summarised as follows:

- The particle velocity is well defined at all locations except where the mean flow derivative becomes infinite
- The particle displacement formulation does not require evaluation of the mean flow derivative, but this variable is not well defined at a critical layer
- The displacement impedance formulation is well defined at a critical layer and does not involve the mean flow derivative. The method breaks down however when boundary layer modes are present.

Another potential advantage of using the displacement impedance formulation is that the equations are not fully coupled; a solution for χ can be obtained first using equation (2.32a), and this is then used in (2.32b) to find a solution for p. It will also be seen in Chapters 5 and 6 that if only the radiated power or the sound pressure at the wall is required, then only (2.32a) need be solved.

The list of properties given in Section 2.5 will be used in Chapter 4 for validating numerical solutions, the key properties here being that $\frac{\partial p}{\partial z} = 0, \chi = 0$ at a critical layer and that solutions are real valued everywhere in the boundary layer when a critical layer is present. Other properties listed may be useful in other ways, particularly the limiting values of the acoustic impedance $\frac{p}{u}$ and of $\frac{\partial \chi}{\partial z}$ and $\frac{\partial u_z}{\partial z}$ at the critical layer. The fact that the particle displacement changes sign across the layer (i.e. continuity of particle displacement does not apply across a critical layer) is important, as is the understanding of which parameters remain finite and which become infinite.

Chapter 3

3. NUMERICAL SOLUTION OF THE GOVERNING EQUATIONS

It was shown in Chapter 2 that the linearized equations for sound propagation in a boundary layer may be written using a number of different wave variables. Because of the preference in this study for avoiding the evaluation of dU/dz, the equations based on particle displacement are used below in preference to those based on particle velocity.

Even with this requirement, for many problems it is still possible to use either equations (2.14a,b), which relate acoustic pressure p and particle displacement q, or equations (2.32a,b) which relate p and the displacement impedance χ. In some special circumstances, however, either χ or q may become infinite. In the first case, an example of which is shown in figure 4.4b), equations (2.14a,b) must be used. If on the other hand q becomes infinite, then equations (2.32a,b) must be used, as discussed in Section 3.3 below.

For most of Chapters 3 to 7 the cubic boundary layer profile since, for a given boundary layer thickness the effects occur more gradually. The $1/7^{th}$ power law profile is mainly discussed in Chapter 8.

3.1 Initial values for the integration through the boundary layer

The same governing equations can be used to model the reflection of incident sound, where the surface acts as a passive boundary, or the radiation of sound into the boundary layer from a prescribed vibration of the wall. The former case, which applies to sound propagation in an acoustically lined duct, involves specification of a boundary condition at the wall and integration outwards through the boundary layer. This case is mentioned in Chapter 10 as being an area for further research.

For the case of sound radiation from a vibrating wall, however, a radiation boundary condition is required at the edge of the boundary layer. Initial values are required for p and

either q or χ at $z = \delta$, depending on the chosen governing equations. The appropriate value for χ will depend on the specified values of free-stream flow velocity and of ω, k_x and k_y.

In the uniform flow region the velocity gradient is zero, $dU/dz = 0$, and the z-dependence of the field variables has the form $e^{-jk_z z}$ for some constant k_z. Thus, at the edge of the boundary layer, equations (2.4) – (2.7) simplify to:

$$\rho_0 \overline{D}\, u_x = jk_x p \tag{3.1}$$

$$\rho_0 \overline{D}\, u_y = jk_y p \tag{3.2}$$

$$\rho_0 \overline{D}\, u_z = jk_z p \tag{3.3}$$

$$\frac{1}{\rho_0 c_0^{\,2}} \overline{D}\, p = jk_x u_x + jk_y u_y + jk_z u_z \tag{3.4}$$

Eliminating u_x, u_y and u_z from these equations leads to

$$\left(\frac{\overline{D^2}}{c_0^{\,2}} + k_x^2 + k_y^2\right) p + k_z^2 p = 0 \tag{3.5}$$

At the edge of the boundary layer $\overline{D} = j(\omega - k_x U_0)$, where U_0 is the free stream flow velocity, and thus from (3.5):

$$k_z = \pm\sqrt{(\omega - k_x U_0)^2 / c_0^{\,2} - k_x^2 - k_y^2} \tag{3.6}$$

Using equation (2.11) to substitute for u_z in equation (3.3) gives

$$p = \frac{-j\rho_0 \overline{D}^2}{k_z} q \tag{3.7}$$

Thus, after choosing an arbitrary initial value for q, initial values for the other variable may be obtained as follows:

$$q_{init} = 1$$

$$p_{init} = \frac{-j\rho_0 \overline{D}^2}{k_z} q_{init} \tag{3.8}$$

$$\chi_{init} = \frac{p_{init}}{q_{init}}$$

When c_0 and ω are real, equation (3.6) shows that k_z is either purely real or purely imaginary, so that the wave either propagates or decays in the uniform flow region. In the case of k_z being imaginary the initial values of q, p and χ are all real and, as discussed in Section 2.5, this means that solutions are real for all values of z.

The square root in (3.8) has an undetermined sign and it is necessary to choose the root whose sign corresponds to propagation or decay away from the surface. When ω and c_0 are real, then k_z is a purely real or purely imaginary quantity and for the sign convention used here the positive root is required in each case. Mathematical routines for evaluating square roots generally choose the root with the positive real part and (3.8) can be programmed as written. In some cases however, as discussed in the next section and in Chapter 5, it is useful to make ω or c_0 complex and programming (3.6) as written may give the wrong root. In general the correct root is always obtained by setting:

$$k_z = -j\sqrt{k_x^2 + k_y^2 - (\omega - k_x U_o)^2 / {c_0}^2} \tag{3.9}$$

3.2 Numerical integration of the governing equations

Integration of equations (2.14a,b) or (2.32a,b) is easily achieved using standard numerical routines. For preliminary studies the equations were integrated using MATLAB routine ODE45 that uses a fourth order Runge-Kutta formulation. The routine allows the specification of a relative tolerance parameter for controlling errors at each step of the integration. The tolerance was adjusted to ensure good convergence of the solutions.

For 3-D problems it was found that solutions using MATLAB were too slow and that the numerical integrations could be very significantly speeded up by use of a FORTRAN sub-

program called from the main MATLAB code. The FORTRAN code used the IMSL library double precision routine DIVPRK that is described in the implementation notes as using a Runge-Kutta-Verner fifth-order and sixth-order method. The Fortran integration routine was not 100% successful in correctly integrating around critical layers, as described in the next section, and this restricted it use to a maximum flow Mach number of 0.3. There are a number of ways round this difficulty which will be implemented in due course, for example by using the limiting values of gradients at the critical layer given in Section 2.5.

3.3 Solution at critical layers

At a critical layer, where $\overline{D} = 0$, it was shown in Chapter 2 that equations (2.14a,b) are not well defined and that (2.32a,b) should be used instead. In practice however, special care is still required to avoid numerical errors when integrating (2.32a,b) up to and past the critical layer, since it is necessary to evaluate the ratio of two parameters, χ and $\overline{D}$, both of which tend to zero there. Tam & Morris [9] have suggested two methods of solution for avoiding a singularity in their equations. The two methods will now be applied in turn to the current problem, to see which best recovers the known properties of the solution at the critical layer as set out in Section 2.5.

3.3.1 Solution using a complex z variable

The first method suggested by Tam & Morris was to integrate around the singularity in their equations by allowing the variable of integration, z, to become complex. The velocity profile $U(z)$ thus becomes a complex valued function, $\overline{D}$ does not become zero, and (2.32b) is defined along all points of the path.

It may be noted that (2.14a,b) can also be integrated in this way except that, because q and dq/dz become large and vary rapidly at the critical layer, it is difficult to integrate the equations accurately.

The solution for $p(z)$ at any point through the boundary layer z_1, up to the critical layer region, is given by the path integral:

$$p(z_1) = p(\delta) + \int_{z=\delta}^{z=z_1} \frac{dp}{dz} dz \tag{3.10}$$

At the point of deviation of the integral into the complex z'-domain there is a change of variable to $z' = f(z)$ for some function f defining the looped path. The path integral is then given by

$$p(z_1) = p(\delta) + \int_{z=\delta}^{z=z_1} \frac{dp}{dz'} \frac{dz'}{dz} dz \tag{3.11}$$

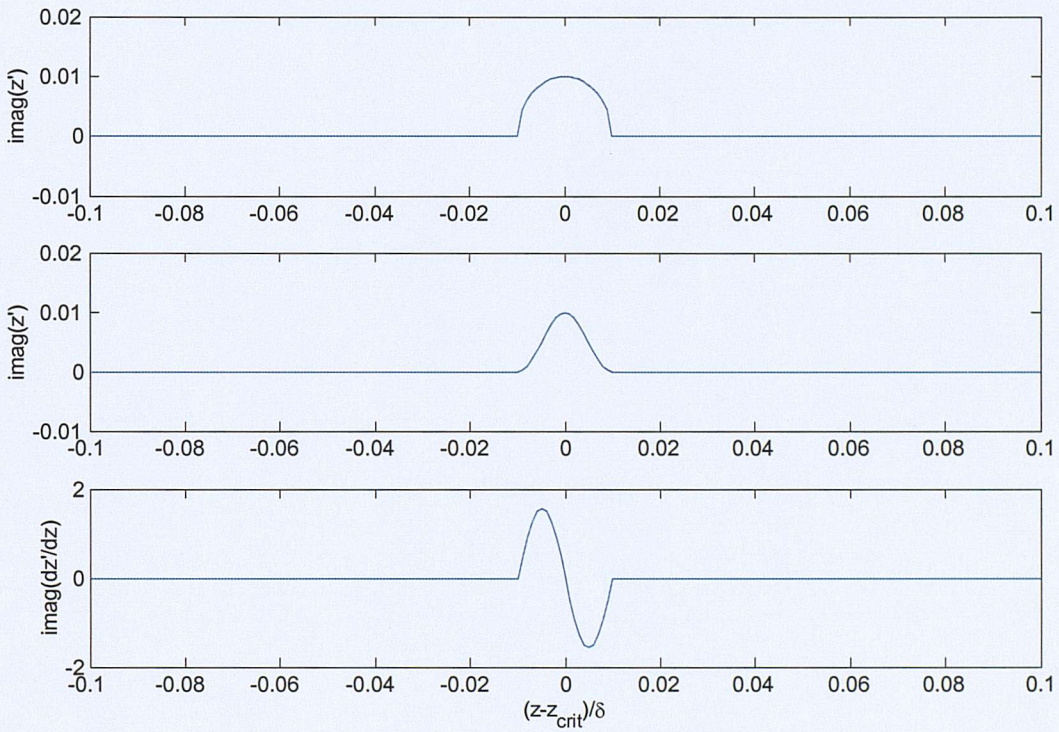

Figure 3.1 Integration variable z' a) as a semi-circular deviation, b) as a cosine deviation. c) shows the derivative of the cosine deviation.

Conventionally a detour around a singularity is depicted as a semi-circle, as illustrated in figure (3.1a), but such a detour causes numerical problems in the integration since dz'/dz is discontinuous at the point of deviation of the path. The detour should thus ideally have a derivative which is continuous everywhere. The function chosen here was defined by

$$z' = z + \frac{i\delta_{crit}}{2}\left(\cos(\frac{\pi}{\delta_{crit}}(z - z_{crit})) + 1\right) \qquad \text{for} \quad |z - z_{crit}| \le \delta_{crit}$$
$$z' = z \qquad \text{otherwise} \qquad , \qquad (3.12)$$

The derivative of z' with respect to z is then given by

$$\frac{dz'}{dz} = 1 - \frac{i\pi}{2}\sin(\frac{\pi}{\delta_{crit}}(z - z_{crit})) \qquad \text{for} \quad |z - z_{crit}| \le \delta_{crit}$$
$$\frac{dz'}{dz} = 1 \qquad \text{otherwise} \qquad (3.13)$$

The imaginary part of z' is shown in figure (3.1b). Its derivative, figure (3.1c), has the required property of continuity at the point of deviation of the path.

By Cauchy's theorem [24,25], which states that the integral of an integrable function around any closed path in the complex plane is zero, the solution at the end of the deviation is independent of the path chosen and is thus the exact solution. In the region of the deviation however the solution obtained is perturbed from the true solution.

Figures 3.2 to 3.4 show a typical solution obtained by using this method to integrate (2.32a,b) around the critical layer to obtain p and χ, q then being calculated from (2.28).

The convention used throughout the thesis for plots such as these, is that the real and imaginary parts of a complex solution are shown in red and green respectively. Where negative values need to be plotted on a logarithmic scale the line is shown dotted. For some logarithmic plots of the pressure the absolute value of the solution provides additional useful information; when plotted this is shown in blue.

Figure 3.2 shows the complete solution throughout the boundary layer on a logarithmic scale. The same result is then shown on expanded linear scales, focussing in progressively on the behaviour of the solution in the region of the critical layer, figure 3.3, and the behaviour in the region of the deviation, figure 3.4. The critical layer occurs at $z/\delta = 0.4$ and the value of δ_{crit} used was $10^{-4}\,\delta$.

The numerical solution may be compared with the expected properties that were listed in Sections 2.5 and 3.1.

- In the outer boundary layer p, q and χ are real valued and decay exponentially away from the wall, figure 3.2.
- At the critical layer $\partial p / \partial z$ and χ are both zero, figure 3.3a,b.
- In the neighbourhood of z_{crit} , q becomes large and changes sign across the critical layer, figure 3.3c.
- A short distance below the critical layer p passes through zero and changes sign, figures 3.2a and 3.3a. χ also passes through zero, figures 3.2b and 3.3b. From (2.30), with k_y=0, $\frac{\partial \chi}{\partial z}$ must have the value $\rho_0 \left(\frac{dU}{dz} \right)^2$ at $z = z_{crit}$.
- In the vicinity of the deviation into the complex z domain, figure 3.4, the imaginary part of χ is perturbed to be non-zero, whereas the real part of χ is largely unperturbed.
- Figure 3.2 shows that the solutions for $z < z_{crit}$ have an imaginary part, whereas from Section 2.5 it is known that solutions must be real valued. This inaccuracy is discussed below.
- χ is predominantly real valued and positive, except between the two zero crossings, figures 3.3b.

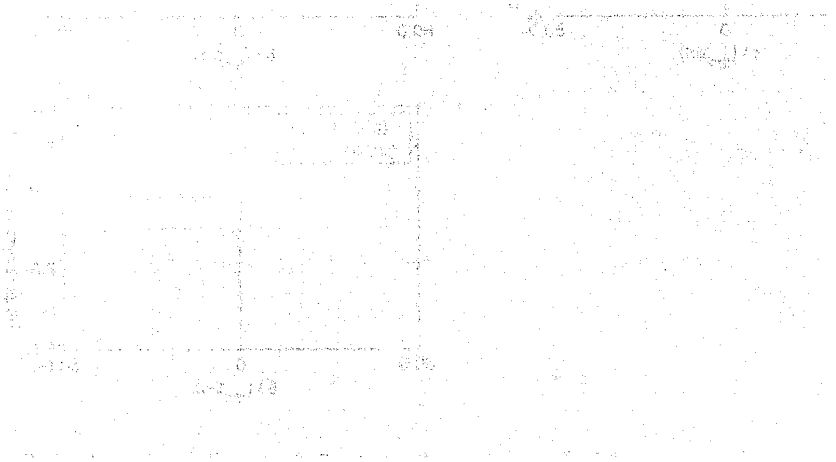

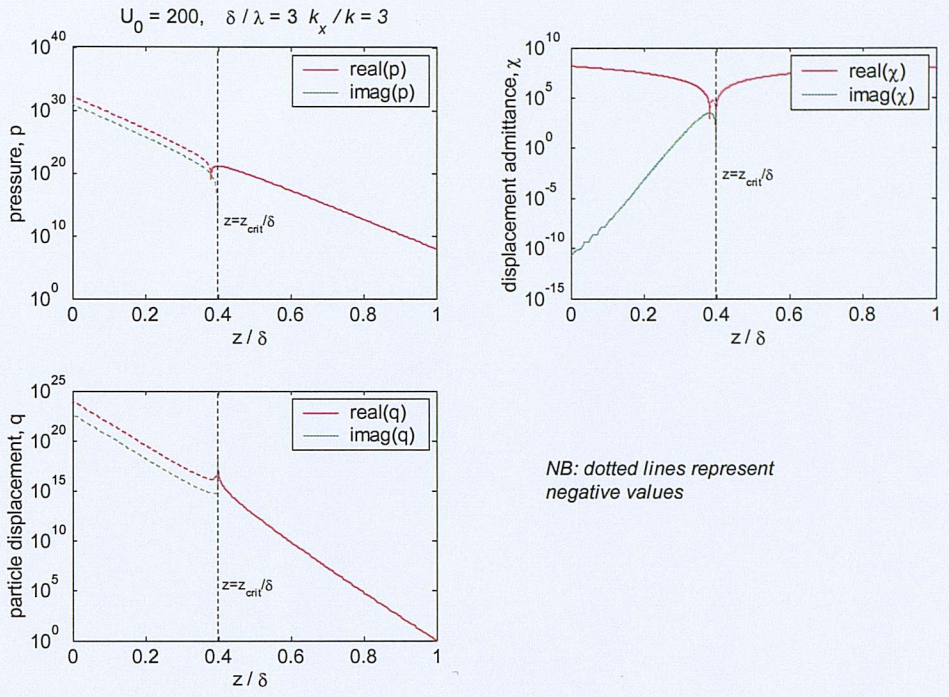

Figure 3.2 Typical numerical solution for pressure p(z) and displacement impedance χ(z) in the presence of a critical layer. Particle displacement is calculated from q(z)=p(z)/ χ(z) . Negative values plotted on logarithmic scales are shown dotted.

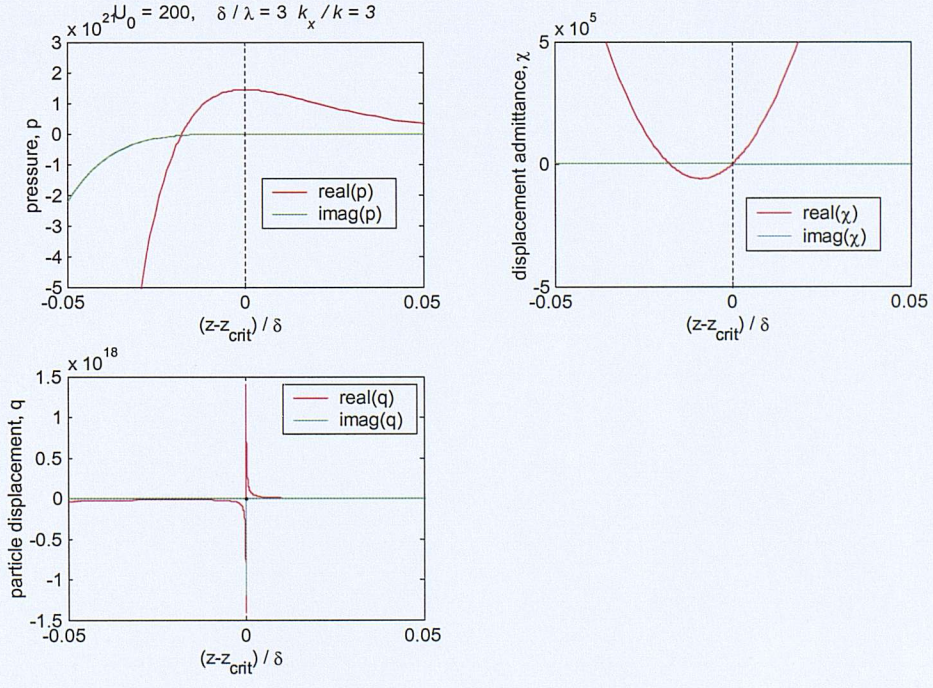

Figure 3.3 Solution from figure 3.2 plotted on expanded linear scales.

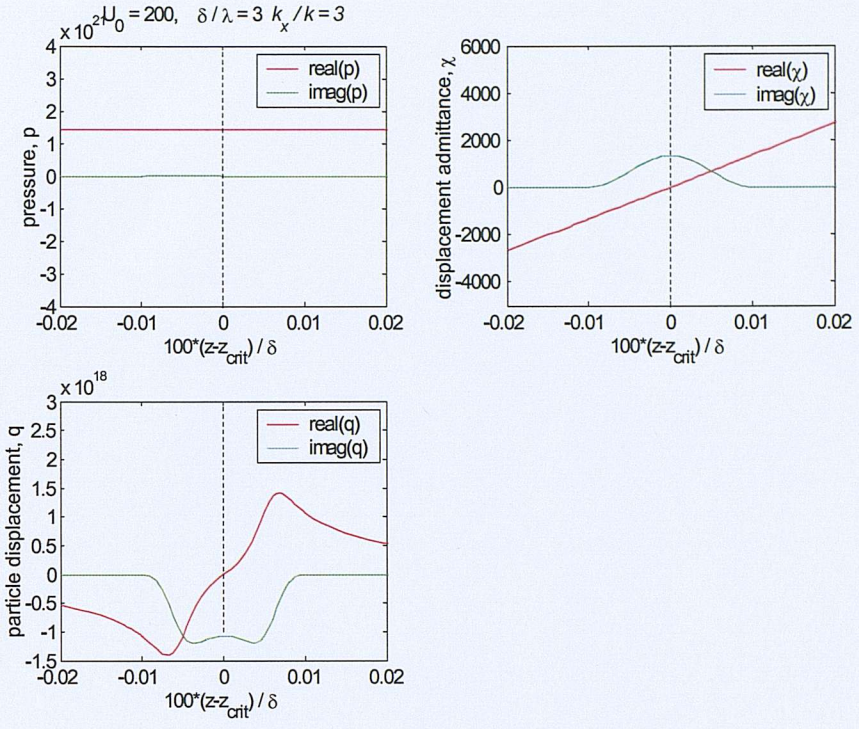

Figure 3.4 Solution from figure 3.3 further expanded in the region of the anti-clockwise deviation around the critical layer.

The solution shown above uses a small value of δ_{crit} , corresponding to 1e-4 δ, and the integration follows a path in which z' has a positive imaginary part, which is referred to as an anticlockwise deviation. Considering the imaginary parts of χ and q in figure 3.4b) and 3.4c) it can be seen that, for an anticlockwise deviation, χ has a positive imaginary part and q has a negative imaginary part.

From this it is clear that the reason for the erroneous imaginary part in the solution of figure 3.2 is that a small numerical error accumulates during the integrating process around the deviation. The residual imaginary part grows rapidly in the final integration to the wall.

Figures 3.5 and 3.6 show the result of integrating instead around a path with a negative imaginary part to z′, a clockwise deviation. This gives a solution *p(z)* with the same real part, but an opposite sign in the imaginary part. Because the integrals around the positive and negative deviations use identical numerical integration steps the magnitude of the residual error is the same in each case, and this fact may be used to obtain the true solution to the

problem. With the two solutions labelled p^+ and p^- respectively, then the true real valued solution to the problem may be taken as either Re(p^+) or as $(p^+ + p^-)/2$.

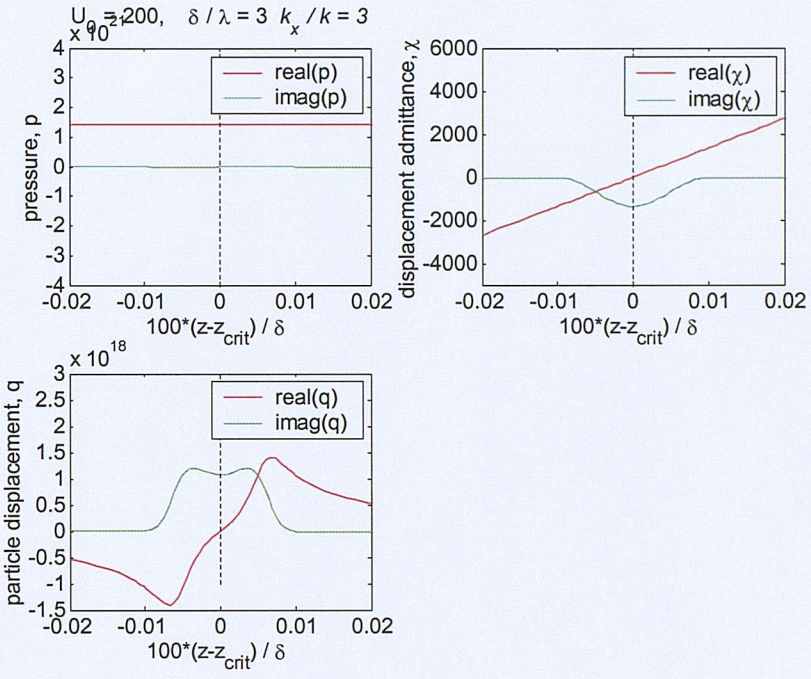

Figure 3.5 Solution as for figure 3.4 but with a clockwise deviation around critical layer.

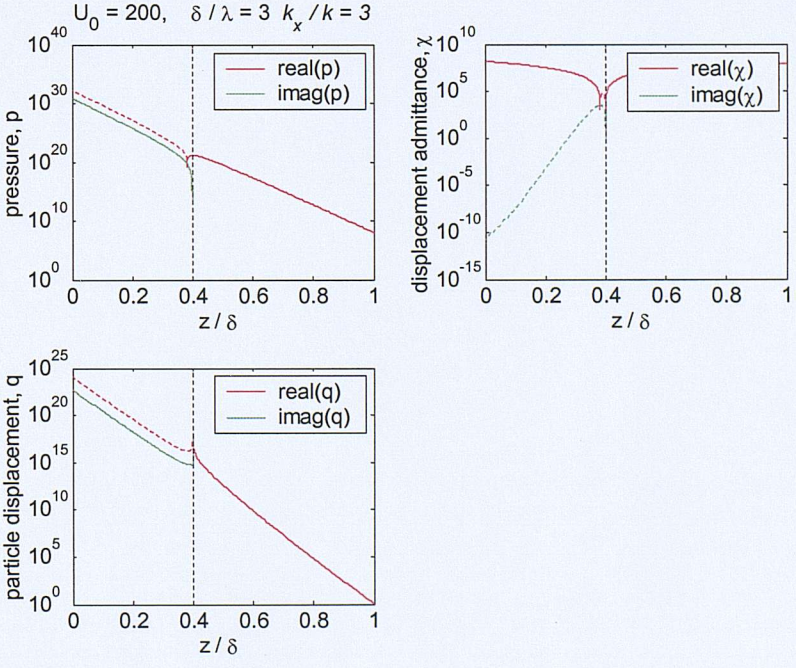

Figure 3.6 Solution as for figure 3.2 obtained using the clockwise deviation of figure 3.5

Figure 3.7 shows the real part of the solution obtained for p, using four different values of δ_{crit}. As noted above, the solution outside the region of deviation into the complex z plane should be exact to within the accuracy of numerical integration, and this is observed in the results shown.

Although the real part is obtained consistently, the erroneous imaginary part is not obtained repeatably. This is shown in figure 3.8 which shows the imaginary part for the same four values of δ_{crit}, the real part of the solution also being shown for reference. The numerical solution does not converge to the correct solution of Im(p)=0 as $\delta_{crit} \to 0$. It is thus necessary to force the correct solution by taking the real part of the numerical solution.

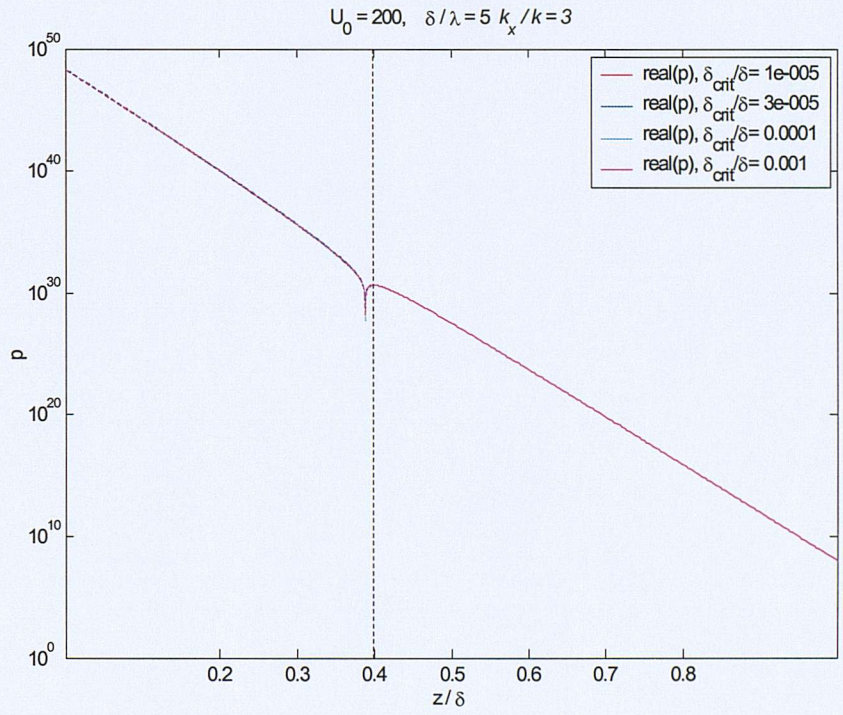

Figure 3.7 Variation of the real part of p(z) for various values of δ_{crit}

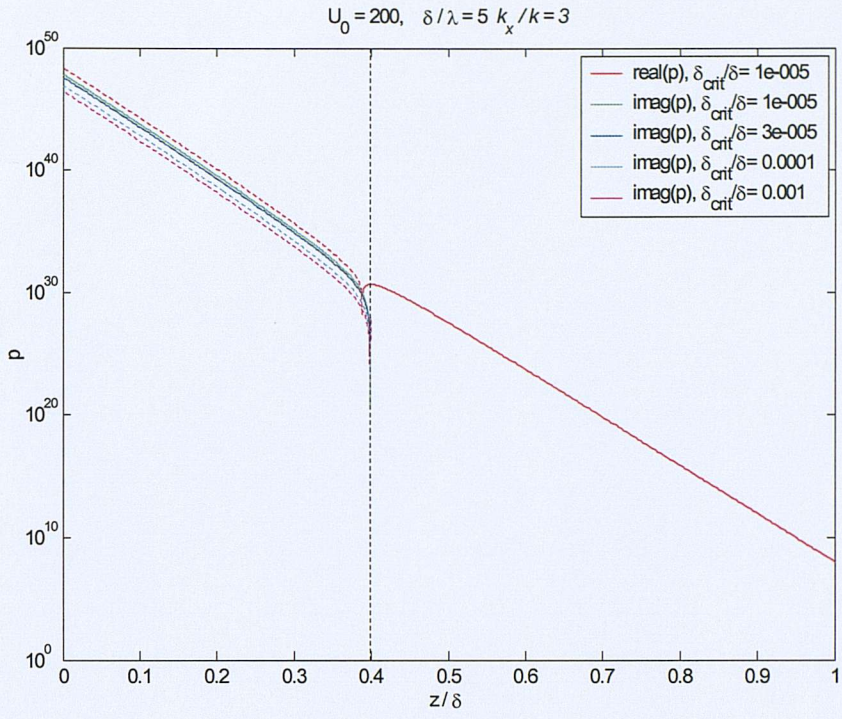

Figure 3.8 Variation of the erroneous imaginary part of p(z) for various values of $\delta_{crit.}$ The real part of the solution is shown for reference

3.3.2 Solution using a complex ω variable

The alternative method proposed by Tam & Morris, [9], is to consider ω to be a complex variable defined by $\omega'(\varepsilon) = \omega(1 + i\varepsilon)$ for some small value of ε. The required solution is then $\lim_{\varepsilon \to 0}(p(z, \omega'(\varepsilon))$.

Causality requires that ε should be negative for the chosen sign convention. Figures 3.9 and 3.10 show the real and imaginary parts of the solution *p(z)* for four values of ε. The same wave number and flow conditions have been used as in figures 3.2 – 3.6.

For the first three values of ε the real part of the solution is independent of ε on this scale, but for ε = -1e-6 the solution changes significantly. Comparison with figure 3.5 shows that the three first solutions are in agreement with the solution found using the complex *z* method, but that when ε becomes too small an error occurs in the integration process. The effect of the numerical error can be seen clearly in the solution for $\chi(z)$, figure 3.11, where the solution obtained for ε =-1e-6 is clearly in error. Furthermore, as ε is made progressively smaller, the real part of the solution appears superficially to be converged and the imaginary part reduces

in proportion to ε. This behaviour gives the impression that the solution is converging correctly, whereas in fact it is converging to an incorrect solution.

It might be thought that taking the opposite sign for ε would lead to an imaginary part of opposite sign, and that the true solution could thus be obtained by adding the two solutions. In fact, for the size of ε necessary to obtain the correct solution to the real part, the imaginary part is not of equal magnitude.

3.3.3 Comparison of solution accuracy using the two methods

The accuracy of the two methods of solution is compared in figure 3.12. The graph shows the pressure at the wall as a function of the small parameter $\delta\omega = \varepsilon\omega$ or δ_{crit}. As already noted, the solution using complex z should give the same answer at the wall irrespective of the chosen path around the singularity. Since the numerical integration process becomes easier the larger δ_{crit} becomes, the best estimate of the correct solution has been taken as the value for $\delta_{crit} = 0.1$. The largest deviation from this value using this method is about 5%.

By comparison the solution using complex ω happens to give the correct answer for one particular value of ε, but never truly converges. Presumably, as $\delta\omega$ is reduced from a value of 0.1, the solution begins to converge towards the correct answer, but then as $\delta\omega$ becomes too small the integration error increases and the solution diverges from the true solution. It may be noted, however, that the maximum error factor of 1.7 shown in figure 3.10 is small in comparison with the overall change by a factor of 10^{40} in p through the boundary layer. For this reason the error does not show up in figure 3.7 when $|\varepsilon| > 1e\text{-}6$.

In summary it has been shown that the complex z method of solution yields more consistently accurate results then the complex ω method, though at the expense of some intricacy in the integration process. However, the complex ω method is simpler to apply, and gives results which may be sufficiently accurate for engineering purposes.

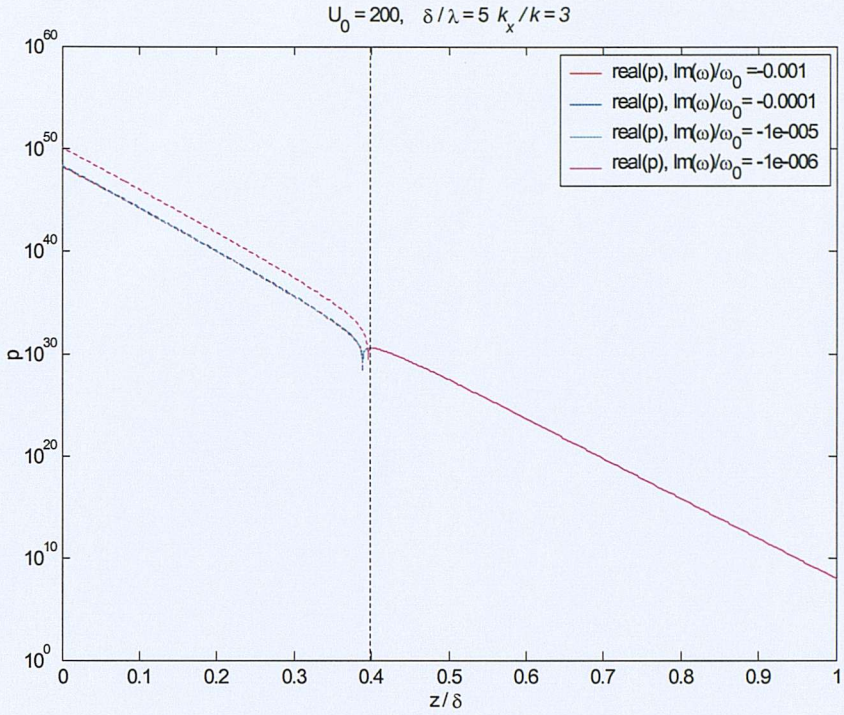

Figure 3.9 Solution for real part of p(z) through the critical layer for four values of ε

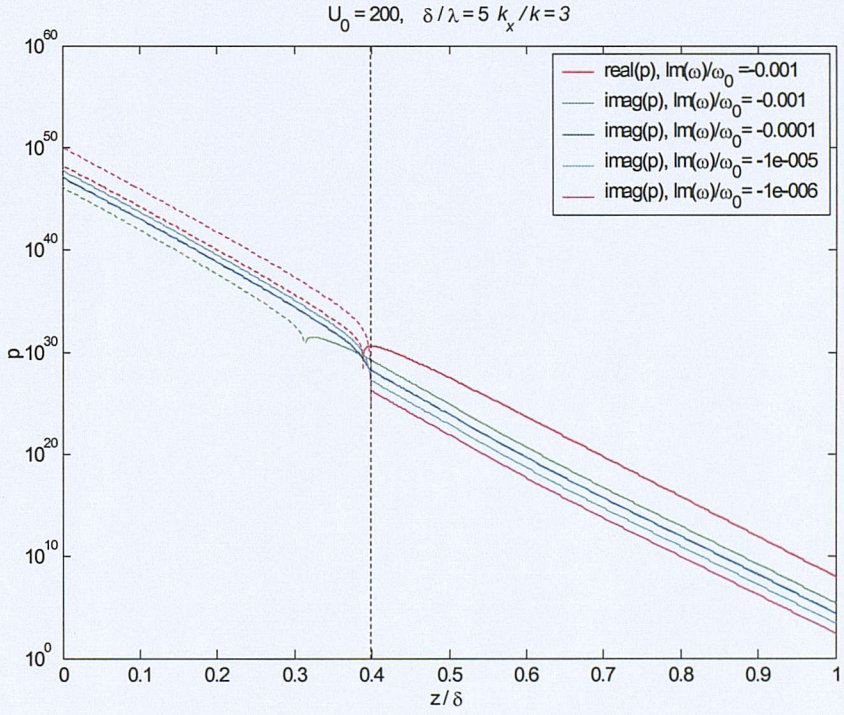

Figure 3.10 Solution for imaginary part of p(z) through the critical layer for four values of ε. Real part of solution shown for reference

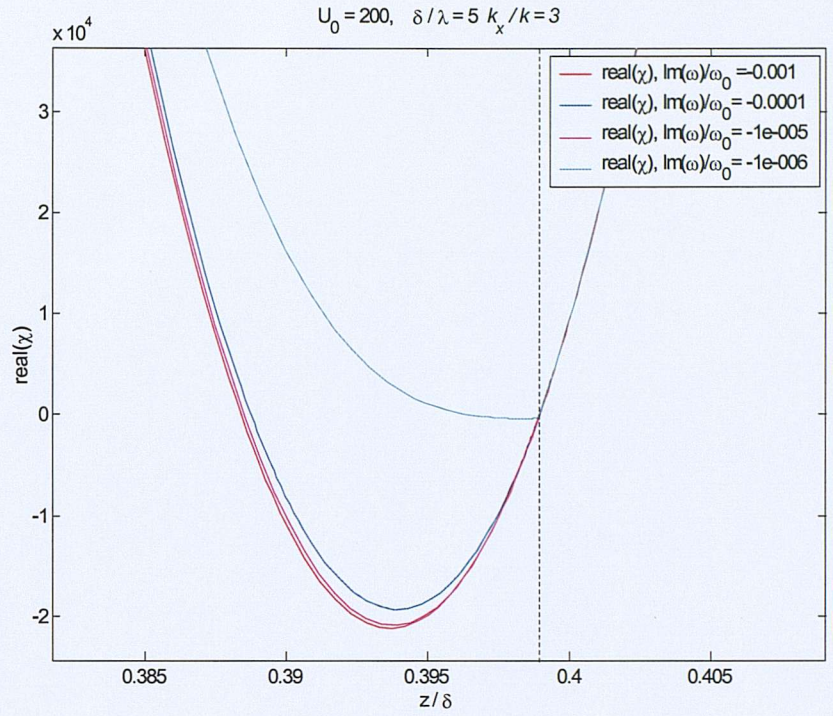

Figure 3.11 Solution for χ(z) through the critical layer for four values of ε showing effect of numerical errors on the solution when ε = 1e-6.

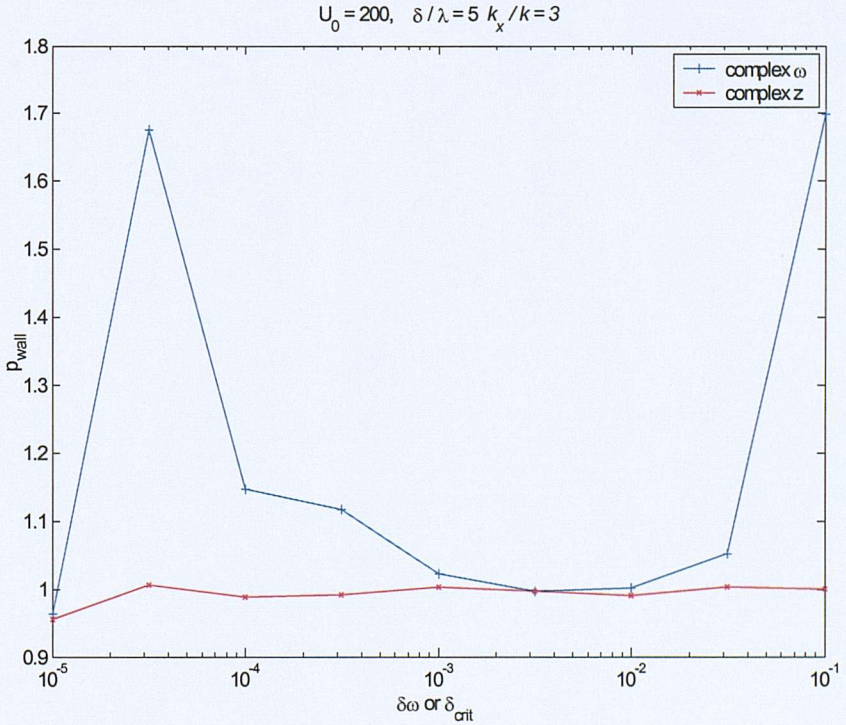

Figure 3.12 Pressure at the wall, real(p(0)), normalised to the best estimate of the correct solution, as a function of δω or δ_{crit}

Chapter 4

4. OUTGOING WAVE SOLUTIONS OF THE GOVERNING EQUATIONS AS A FUNCTION OF WAVE NUMBER

This chapter discusses, for one particular velocity profile, the general characteristics of solutions to the governing equations as a function of wave number k_x. A few example solutions with zero flow are presented for reference in Section 4.1, but the main results of the chapter are shown in Section 4.2.

Besides being dependent on wave number, the solutions will also depend upon the parameters of the boundary layer profile, i.e. the free stream velocity, the boundary layer thickness and the boundary layer shape. The two profiles used throughout this thesis are a third order polynomial (cubic) profile, which is typically used to define the flow profile for a laminar boundary layer, and the $1/7^{th}$ power law profile, which is commonly used to approximate a turbulent boundary layer; the free-stream velocity in both cases is assumed constant (i.e. non-accelerating flow). The two profiles are defined in equation (4.1) and plotted in figure 4.1.

$$U_{cub}(z) = \frac{U_0}{2}\left(\frac{3z}{\delta} - \frac{z^3}{\delta^3}\right)$$
$$U_{1/7}(z) = U_0\left(\frac{z}{\delta}\right)^{1/7} \tag{4.1}$$

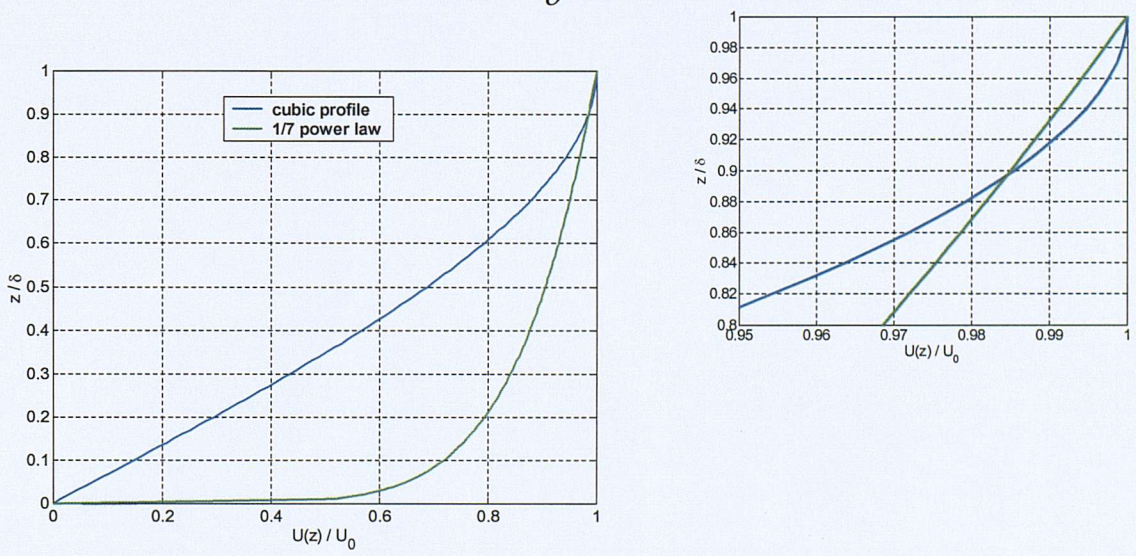

Figure 4.1 Cubic and $1/7^{th}$ power law mean flow boundary layer profiles. The insert shows that $\delta_{99} \approx 0.92\delta$ for the cubic profile and $\delta_{99} \approx 0.93\delta$ for the $1/7^{th}$ power law profile.

The boundary layer thickness parameter used in the bulk of this thesis is δ, the distance from the wall to the edge of the uniform flow. Generally boundary layers are defined by the thickness at which 99% of the free-stream flow velocity is attained, δ_{99}. Figure 4.1 shows that this is occurs at 0.92δ and 0.93δ for the two profiles shown. Other boundary layer parameters are discussed in Chapter 8.

Numerical solutions shown in Section 4.2 are for free stream Mach number $M_0 = 0.6$, the boundary layer thickness is chosen to be three wavelengths thick, $\delta/\lambda = 3.0$ and the cubic flow profile is used. These basic flow conditions provide a case where all the key features of the solutions can be observed as the axial wave number is changed. The effect of varying each of the mean flow parameters, including the boundary layer profile, is considered in later chapters.

For most of the solutions presented equations (2.14) were solved to give p and q, χ is then calculated from these solutions. The exception is where a critical layer occurs, in which case equations (2.32) are solved for p and χ. The plots always show p and χ, since these are more informative than plots of p and q.

Whereas in the previous chapter the main interest was in numerical methods and the accuracy of numerical solutions, with results presented in an un-normalised form as integrated from the initial values in (3.8), the aim of this and subsequent chapters is to describe the physical nature of the sound field radiated from a vibrating surface. For this reason solutions will now be presented in a non-dimensionalised form:

$$\begin{aligned} q_{norm}(z) &= \frac{q(z)}{q(0)} \\ p_{norm}(z) &= \frac{p(z)}{\omega\rho_0 c_0 q(0)} \\ \chi_{norm}(z) &= \frac{p_{norm}}{q_{norm}} = \frac{\chi(z)}{\omega\rho_0 c_0} \end{aligned} \tag{4.2}$$

It will be seen that, because of the non-uniform flow, sound is refracted as it propagates away from the surface. Refraction may be examined by considering the direction of propagation

of the wave to be approximated by a 'local wave vector', $\mathbf{k}=\frac{\nabla p}{-jp}$. For a plane wave propagating in uniform flow this vector is normal to the wave front (the surface of constant phase), [20].

Assuming Fourier transformed x- and y-variables the wave vector is given by:

$$\mathbf{k}=\frac{\nabla p}{-jp}=(k_x, k_y, \frac{1}{-jp}\frac{\partial p}{dz}) \tag{4.3}$$

Defining a z-dependent notional local wave number in the z-direction, $k_z(z)$, such that

$$\frac{\partial p}{\partial z}=-jk_z p \tag{4.4}$$

then, using equation (2.14b) and (2.28), k_z is given by

$$k_z=-j\rho_0\overline{D}^2\frac{q}{p}=-j\rho_0\frac{\overline{D}^2}{\chi} \tag{4.5}$$

If, in the region of some point z_0, the function $k_z(z)$ is effectively constant, then the solution to equation (4.4) in the region around z_0 is

$$p(z)=|p(z_0)|e^{-jk_z(z_0)z} \tag{4.6}$$

and, from equation (4.3),

$$\mathbf{k}(z_0)=(k_x, k_y, k_z(z_0)) \tag{4.7}$$

In general it will be seen that k_z is a complex valued function, and splitting the real and imaginary parts of $k_z(z_0)$ in (4.6) gives.

$$p(z)=|p(z_0)|e^{\mathrm{Im}(k_z(z_0))z}e^{-j\,\mathrm{Re}(k_z(z_0))z} \tag{4.8}$$

Clearly Im(k_z) determines whether p(z) is locally growing or decaying in the z-direction, whereas Re(k_z) defines the local phase variation of the solution and thus the nominal direction of propagation of the wave. This is similar to the approaches of Rice [26] for soft-wall duct modes and Candel [20] for ray acoustics in non-uniform flow. The nominal angle of propagation of the wave relative to the wall, θ_x, is thus given by equation (4.9). Taking the absolute value of k_x in the denominator aids interpretation of the angle plots since this always gives an angle in the range 0° to 90°.

$$\theta_x = \tan^{-1}\left(\frac{\mathrm{Re}(k_z)}{abs(k_x)}\right) = \tan^{-1}\left(\mathrm{Re}\left(\frac{-j\rho_0\overline{D}^2 q}{abs(k_x)p}\right)\right) = \tan^{-1}\left(\mathrm{Re}\left(\frac{-j\rho_0\overline{D}^2}{abs(k_x)\chi}\right)\right) \qquad (4.9)$$

This definition of propagation angle is not appropriate where k_z is varying rapidly on a wavelength scale and a local solution in the form of equation (4.6) is not valid. Similarly, when Im(k_z) is large relative to Re(k_z) the concept of an angle of propagation is not well defined by equation (4.9). It will be seen however that the propagation angle defined in this way is convenient for describing the refraction through the boundary layer.

4.1 Zero flow solutions

The purpose of this section is to provide a few illustrative no-flow solutions as a reference point for the with-flow solutions presented in the next section. Although there is no mean flow, propagation over a notional boundary layer three wavelengths thick is assumed.

In the absence of mean flow the solution is homogeneous in the z-direction and the uniform flow z-wave number k_z, obtained from equation (3.8), is constant everywhere and controls whether the wave propagates or decays away from the surface. The angle of propagation calculated from equation (4.9) is also constant in z.

Figures 4.1a-d) show the pressure, displacement impedance, wave number k_z and propagation angle for waves with k_x/k_0 = 0, 0.95 and 1.5. The result for k_x/k_0 = 0 is shown on a linear y-scale in figure 4.1a) and on logarithmic scale in figure 4.1b).

As before the convention used for plotting complex data is red for the real part, green for the imaginary part and blue for the modulus. Negative data plotted on the logarithmic scale are

shown as dotted lines. Depending on whether the wave is propagating or decaying it may be convenient to use either logarithmic or linear scales, and the appropriate choice is made without further note in the descriptions below.

When $|k_x/k_0| < 1$ (i.e. $k_x/k_0 = 0$ or 0.95) the wave propagates in the z-direction and the real and imaginary parts of pressure vary sinusoidally. The ratio between pressure and particle displacement, χ, is a constant purely imaginary number in each case, thus the relative amplitude and phase of p and q is constant at all locations. As $|k_x|$ is increased, k_z decreases so that the wavelength in the z-direction increases, and the angle of propagation relative to the x-axis decreases; thus at $k_x/k_0 = 0.0$ and $k_x/k_0 = 0.95$ the wave radiates at 90° and 20° to the x-axis respectively.

When $|k_x/k_0| > 1$ equation (3.8) shows that k_z becomes imaginary and the wave is evanescent, decaying exponentially away from the surface and, from (4.9), with an angle of propagation of 0°. This is shown in figure 4.1c) for the case $k_x/k_0 = 1.5$. With the pressure plotted on a log scale the constant rate of decay away from the surface is clear, and determined by $\mathrm{Im}(k_z)$. For cut-off waves the displacement impedance χ is a constant purely real number.

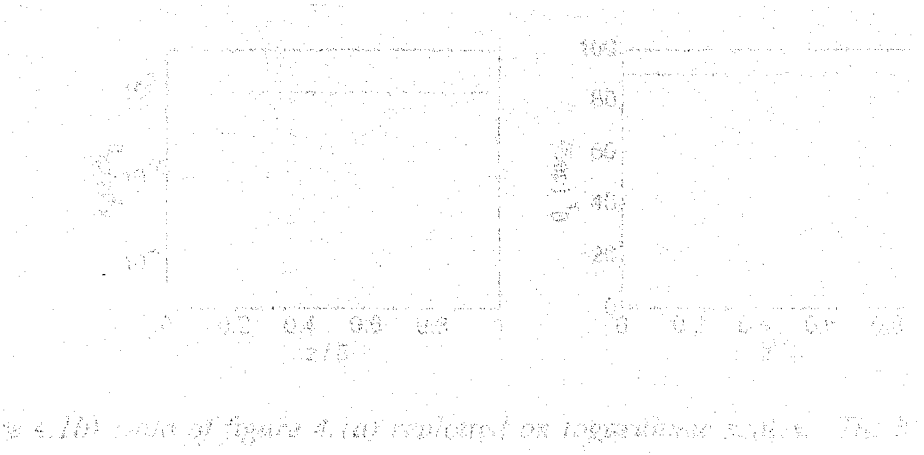

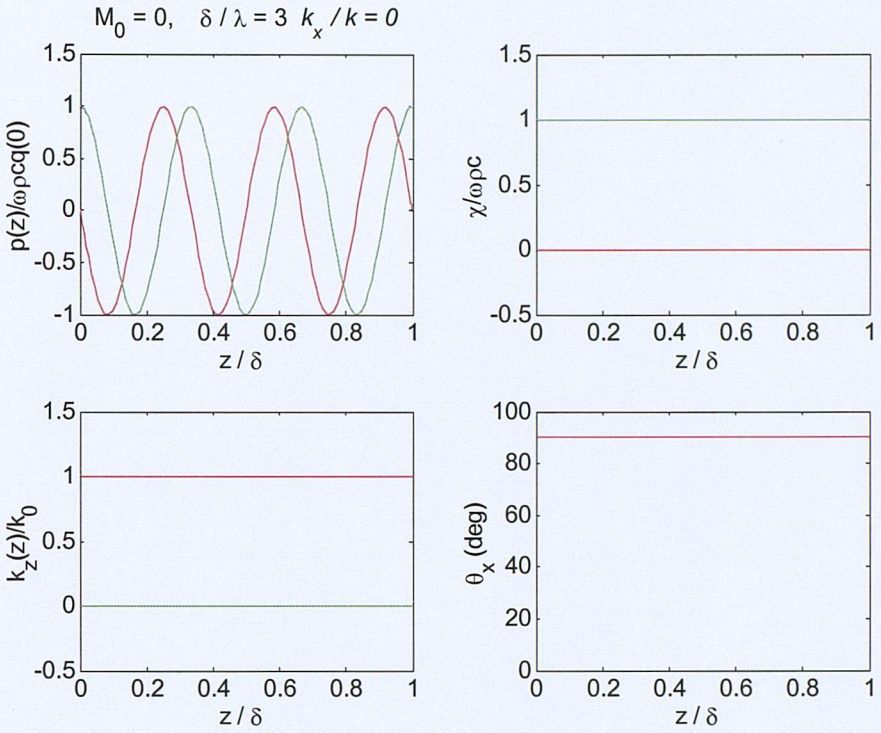

Figure 4.1a) Pressure, particle displacement and displacement impedance for a waves with $k_x/k_0=0$, no flow. The real part of each variable is shown in red, the imaginary part in green

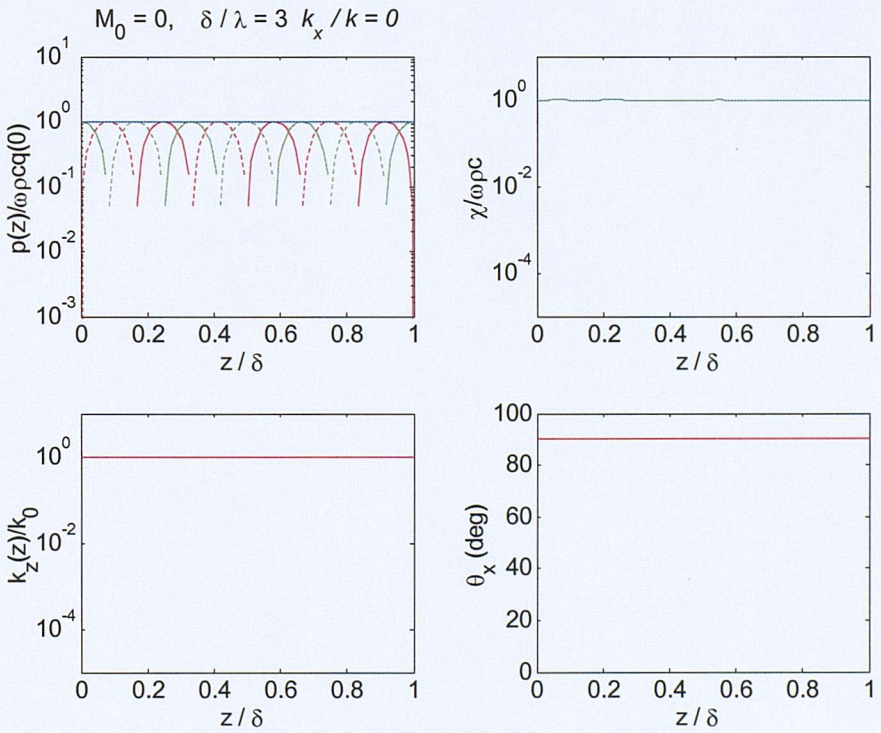

Figure 4.1b) Data of figure 4.1a) replotted on logarithmic scales. The blue line shows the modulus of the solution, negative values on a logarithmic scale are shown dotted.

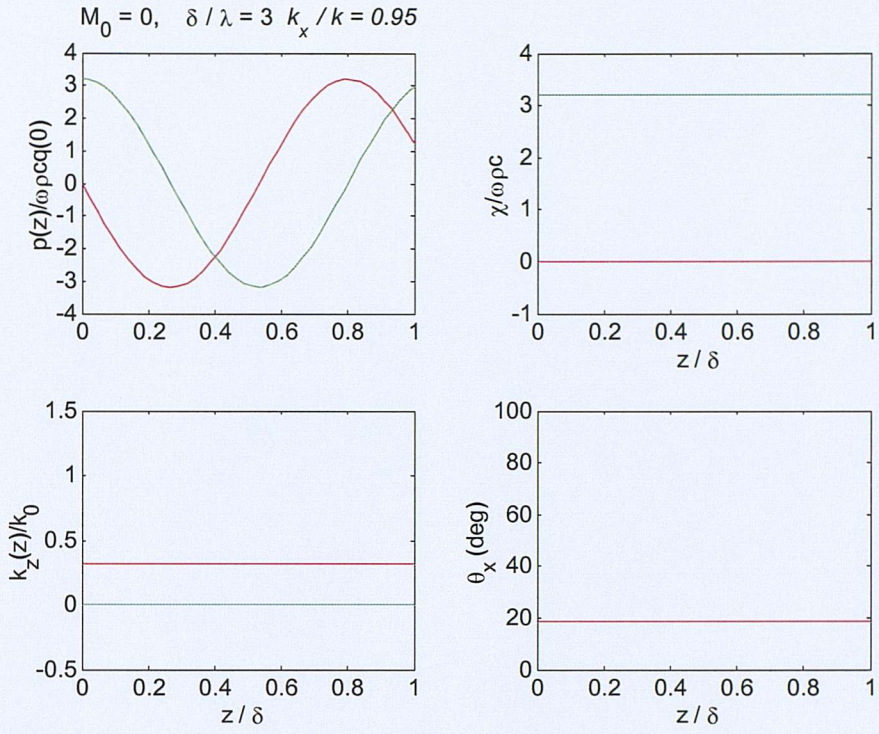

Figure 4.1c) Solution for k_x/k_0=0.95, no flow.

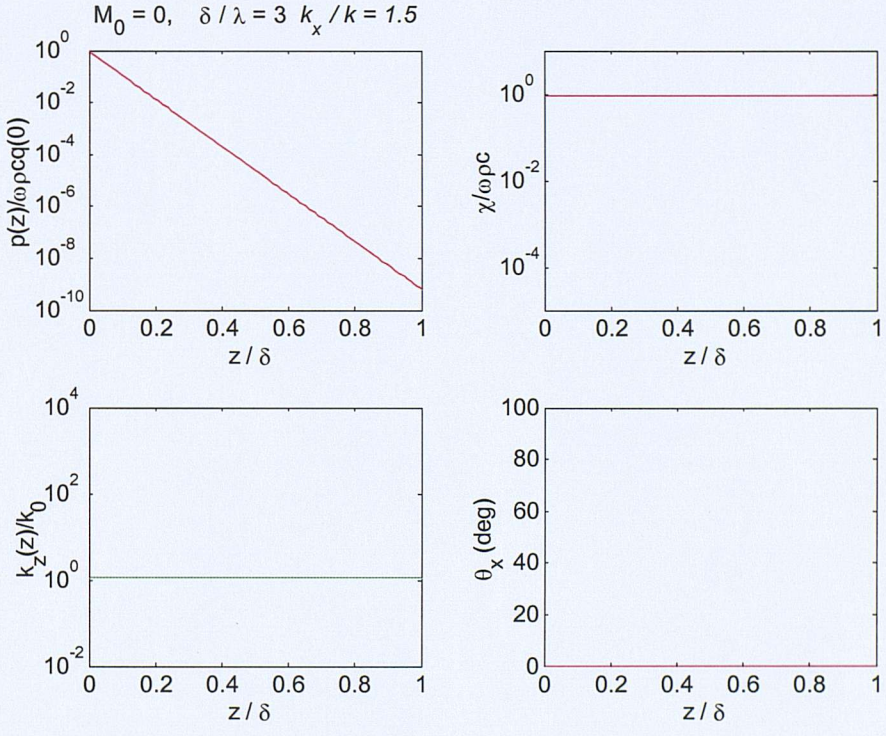

Figure 4.1d) Solution for k_x/k_0=1.5, no flow.

4.2 Solutions with a mean shear flow

Throughout this section the mean flow and boundary layer parameters are taken as $M_0 = 0.6$, $\delta / \lambda = 3$ and the cubic boundary layer profile defined by (4.1) is used. Plots are presented on either linear or logarithmic scales as appropriate.

Consider first the case $k_x/k_0 = 0$. Equation (3.7) shows that the initial values for p, q and χ are independent of the mean flow, as are the differential equations (2.13) or (2.30). Thus the solution for $k_x/k_0 = 0$ is as shown in figure 4.1a).

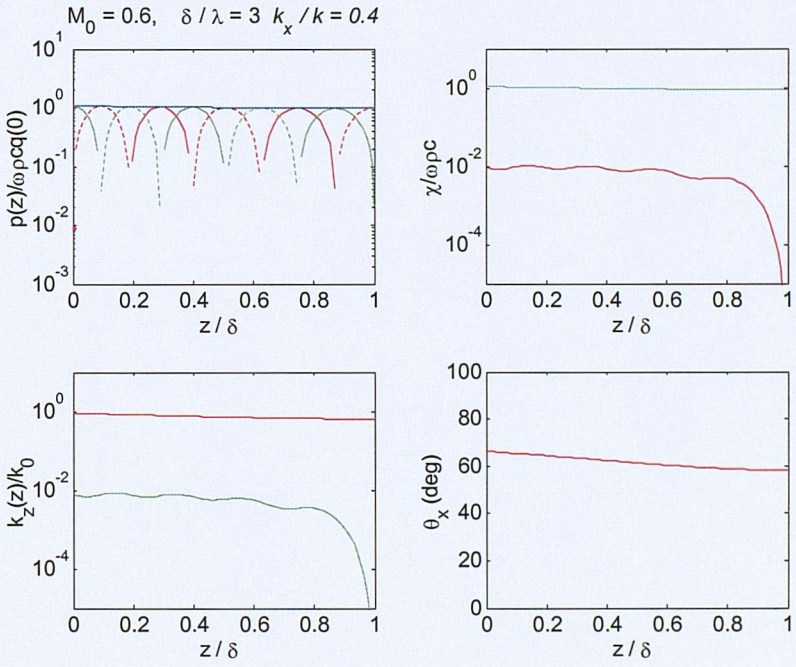

Figure 4.2a) Solutions for a wave with k_x/k_0=+0.4; reference flow conditions

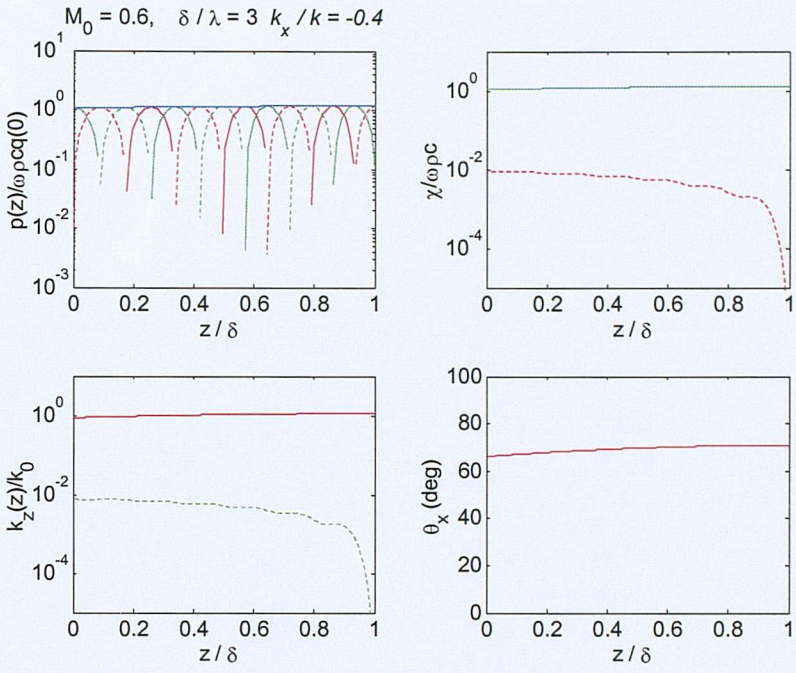

Figure 4.2b) Solutions for a wave with k_x/k_0=-0.4; reference flow conditions

When a mean shear flow is present, the direction of wave propagation relative to the mean flow is important, the effect being illustrated in figure 4.2 which shows solutions for k_x/k_0 = ±0.4. For the wave propagating in the positive x-direction, (k_x/k_0 = +0.4, figure 4.2a), the amplitude of the wave falls slightly with distance from the wall and the angle of propagation changes from 65° at the wall to 59° at the edge of the boundary layer, i.e. the wave is refracted towards the direction of flow. These two effects are both evident in the wave number plot, the small reduction in the real part controlling the change in propagation angle (note that the change in z-wavelength is also apparent in the pressure plot), and the small positive imaginary part determining the decay in amplitude away from the surface.

For the wave propagating against the flow (k_x/k_0 = -0.4, figure 4.2b), the pressure amplitude grows with distance from the wall and the angle of propagation changes from 65° at the wall to 70° at the edge of the boundary layer, i.e. the wave is refracted away from the wall. These effects can again be seen in the wave number plot, with the change in wavelength in the z-direction also evident in the pressure plot. The imaginary part of k_z is negative since the wave grows as it propagates away from the wall.

An interesting feature of the wave number plots is that the imaginary part oscillates. This indicates that, although the pressure varies monotonically through the boundary layer, the rate of change is not constant. Clearer examples of this effect are given below and discussed in more detail.

Before proceeding to examine in detail the behaviour of outgoing wave solutions for other k_x values it is useful to consider the global picture, as presented in figure 4.3. The red and green curves show respectively the angle of propagation at the wall and the angle of propagation at the edge of the boundary layer as a function of k_x. It should be noted that, because the absolute value of k_x is taken in equation (4.9), for negative wave numbers the angle is taken relative to the upstream direction. Thus an angle of 65° upstream corresponds to an angle of 180-65 = 115° relative to the flow direction. This was convenient since it makes the angular changes due to refraction away from the surface easier to interpret.

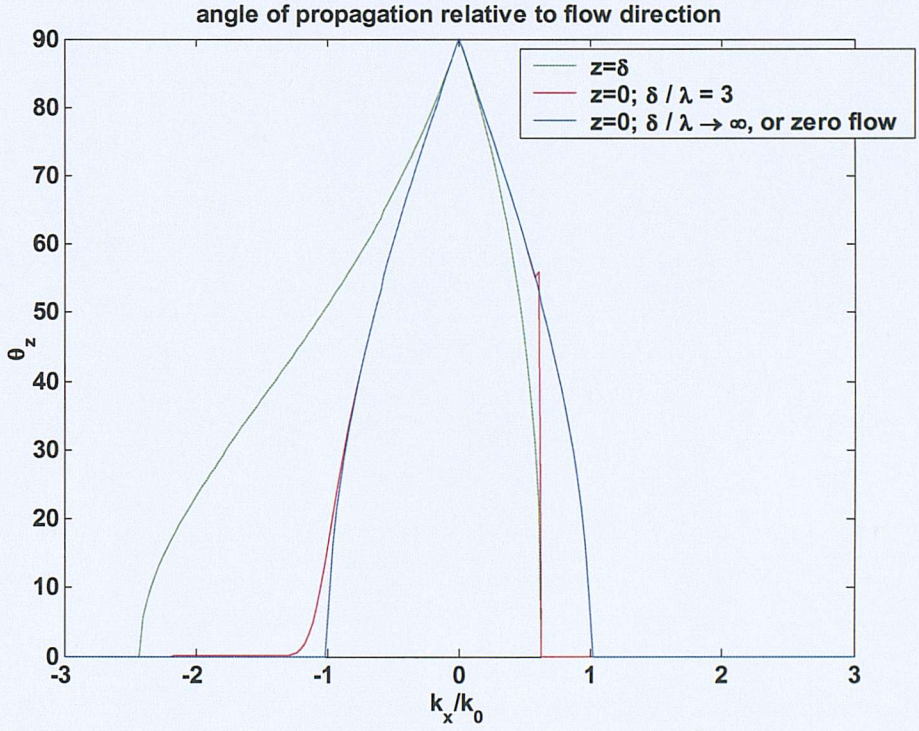

Figure 4.3 Changes to the propagation angle through the boundary layer. M_0=0.6, $\delta / \lambda = 3$.

For reference the propagation angle in the absence of flow is also plotted, showing that for $|k_x/k_0| > 1$ the propagation angle is zero and waves are evanescent. This line can also be considered as the propagation angle at z=0 in the limit as $\delta/\lambda \rightarrow \infty$. For $k_x = \pm 0.4$ the change in angles already noted can be seen.

Features of particular interest in figure 4.3 are as follows:

- for $k_x/k_0 > 1/(1+M_0) = +0.62$, i.e. when the wave in the surface is propagating downstream subsonically relative to the uniform flow, solutions have a propagation angle of zero at both $z=\delta$ and at $z=0$. This indicates that cut-off occurs simultaneously in the uniform flow region and at the wall.
- for $k_x/k_0 < -1/(1-M_0) = -2.5$, i.e. the wave in the surface is propagating upstream subsonically relative to the uniform flow, solutions have a propagation angle of zero in the region of uniform flow. It will be shown below that, for $-2.5 < k_x/k_0 < -1$ the propagation angle converges to zero but remains finite until cut-off occurs when $k_x/k_0 < -2.5$.

We now return to the detailed examination of solutions for specific wave numbers, using figure 4.3 for guidance, and first consider waves propagating with the flow. Figures 4.4a)-d) show solutions for $k_x/k_0 = 0.6$, 0.7, 1.5 and 2.0, values which have been selected to show a range of features of interest.

At $k_x/k_0 = 0.6$ the wave is still cut-on at the edge of the boundary layer, k_z has a dominant real part, but the imaginary part oscillates between positive and negative. In this case pressure no longer varies monotonically through the boundary layer, but actually grows and declines in amplitude. The pressure amplitude variation is reminiscent of a standing wave, except that the reflected wave (travelling inwards towards the surface) is produced by the gradient in the mean flow rather than by a discrete change in flow. The angle of propagation appears to vary significantly, although $\mathrm{Re}(k_z)$ may be varying too rapidly for equation (4.4) to be accurate.

At $k_x/k_0 = 0.7$ the wave is cut-off, $\mathrm{Re}(k_z)=0$, and this gives a propagation angle of 0°. At $z/\delta=0.15$ the pressure changes sign, passing through zero, and as a result the displacement impedance χ also passes through zero and changes sign. At $z/\delta = 0.02$ and 0.35 however χ becomes large and changes sign, and this indicates that particle displacement, q, passes through zero. At such points it is clear that solving governing equations (2.14a,b) for p and q is appropriate since equation (2.32b) is not defined where $q = 0$. The oscillating real part of pressure is indicative of a standing waves in the channel formed by the boundary layer.

At higher wave numbers, e.g. $k_x/k_0 = 1.5$, the solutions for p and q decay exponentially away from the wall, with the rate of decay increasing as k_x increases.

Finally, when $k_x/k_0 > 1/M_0 = 1.67$, there is the wave number region in which a critical layer occurs, as discussed in detail in Section 3.3. The result shown in figure 4.4d) is for $k_x/k_0 = 2.0$, and displays the change in sign of p and the double zero crossing of χ. Both wave number and propagation angle plots are meaningless for this solution.

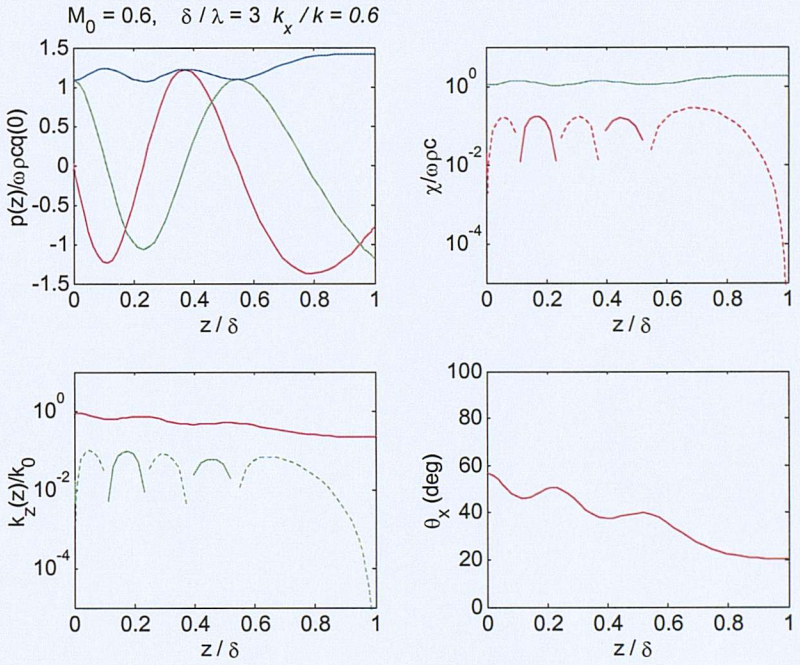

Figure 4.4a) Solution for a wave with k_x/k_0=+0.6; M_0=0.6, $\delta / \lambda = 3$.

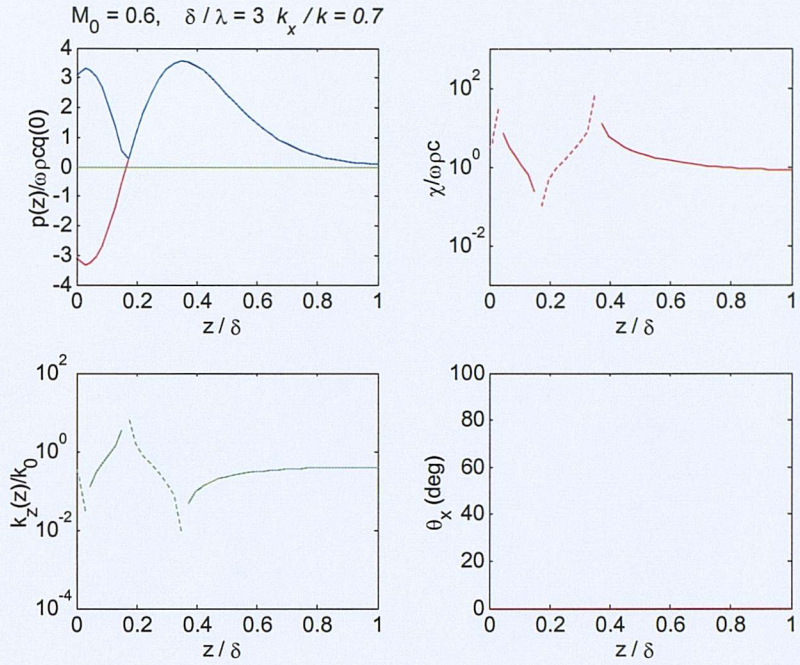

Figure 4.4b) Solution for k_x/k_0=+0.7.

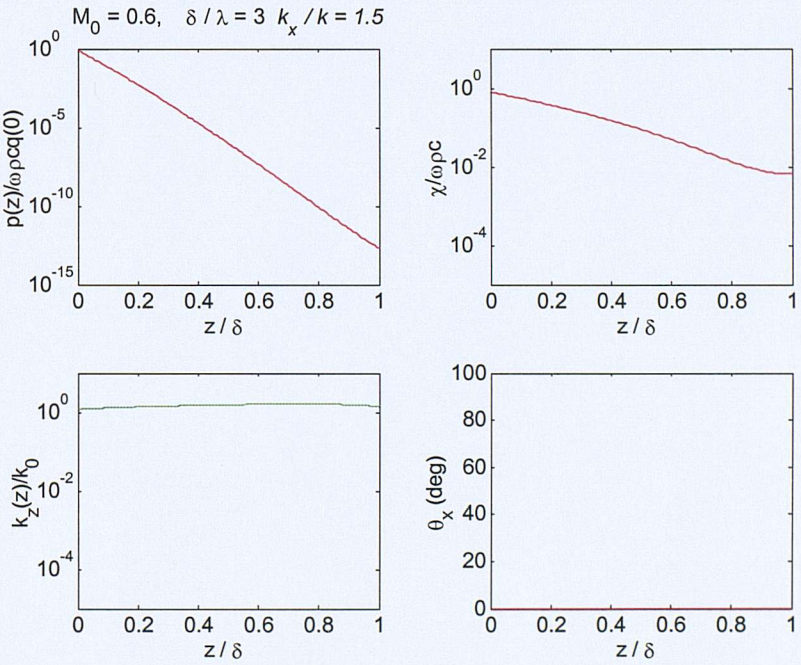

Figure 4.4c) Solution for k_x/k_0=+1.5

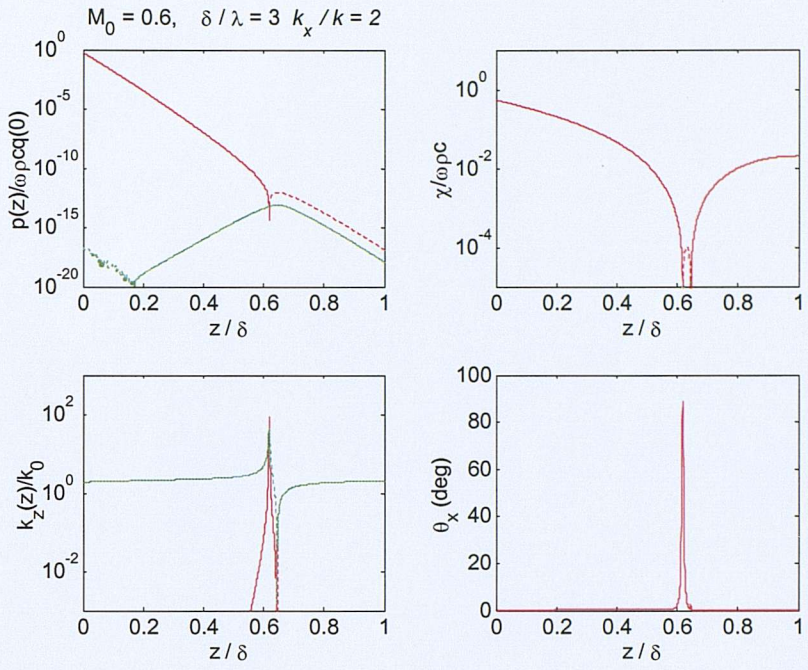

Figure 4.4d) Solution for k_x/k_0=+2.0.

Considering next negative values of k_x, representing waves propagating upstream, figure 4.5a)-d) show solutions for k_x/k_0 = -0.95, -1.1, -1.5 and –3.0.

For k_x/k_0 = -0.95, k_z is predominantly real throughout the boundary layer and the wave is propagating, although the pressure amplitude initially falls and then increases as indicated by the change of sign of Im(k_z). Re(k_z) grows through the boundary layer indicating refraction away from the wall as shown by θ_x.

When k_x/k_0 = -1.1, k_z is initially dominated by the imaginary part so that the pressure shows a strong decay, although because Re(k_z) > 0 the propagation angle is greater than 0°. The effect is more marked at k_x/k_0 = -1.5. These waves are called tunnelling waves [ref] since they are close to being cut-off near the wall, but do permit some transportation of energy away from the wall. From figure 4.5c) may be inferred that the cross-over could be defined as the point where Re(k_z) > Im(k_z).

The final plot in figure 4.5 is for k_x/k_0 = -3.0. In this case the wave is cut-off in the uniform flow region and the pressure decays exponentially throughout the boundary layer.

Unlike the positive values of k_x/k_0 which propagate downstream and are refracted towards the wall, there are no standing wave effects seen for the wave numbers representing upstream propagation.

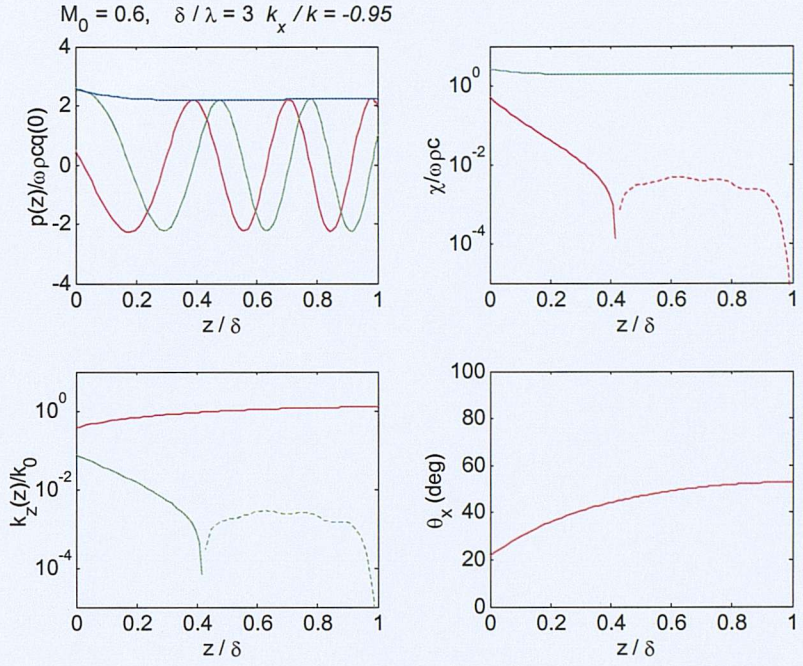

Figure 4.5a) Solutions for k_x/k_0=–0.95 with the reference mean flow.

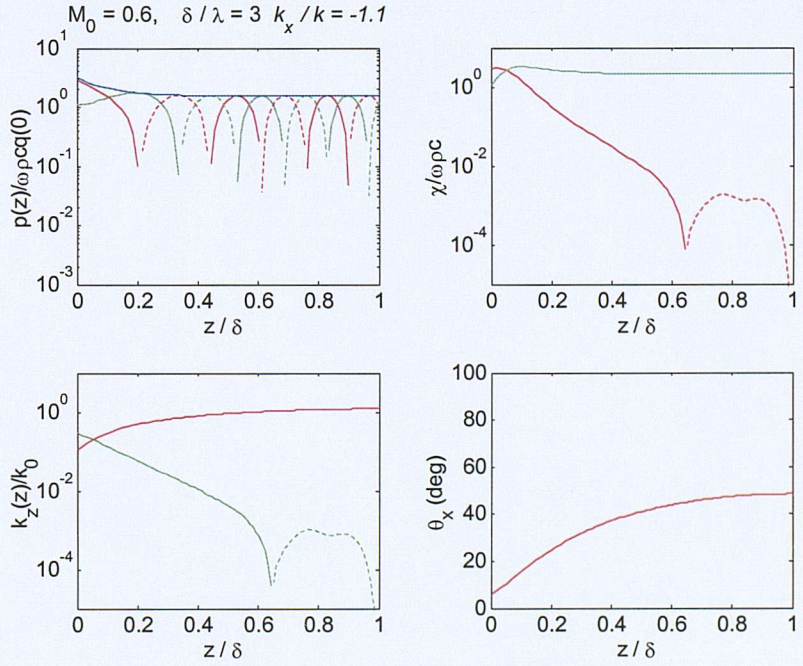

Figure 4.5b) Solutions for k_x/k_0=–1.1

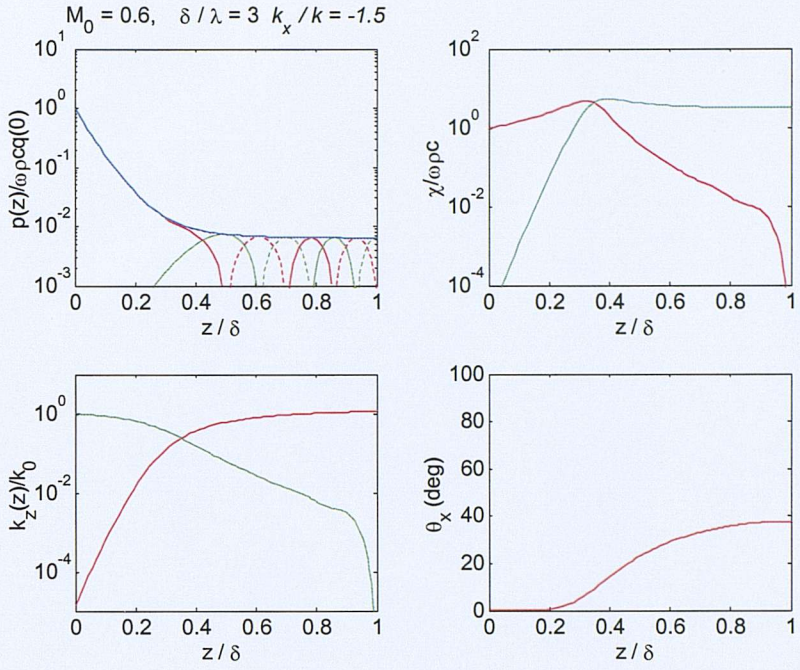

Figure 4.5c) Solutions for k_x/k_0=–1 5

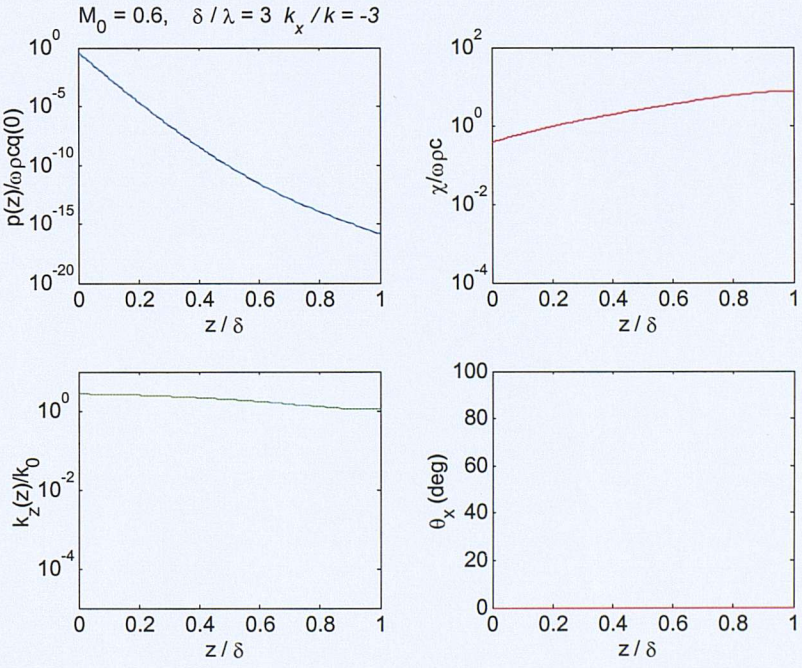

Figure 4.5d) Solutions for k_x/k_0=–3.0.

4.3 Conclusions

For sound radiation into a uniform flow the waves are either cut-on or cut-off depending on the speed of the wave in the surface relative to moving fluid.

This chapter has demonstrated the more complex behaviour of sound propagation through a shear flow, with upstream propagating waves being refracted away from the surface, whilst downstream propagating waves are refracted downstream and are thus 'channelled' by the boundary layer.

Two particular effects may be expected to significantly alter the sound field radiated into a shear flow compared with the radiation into a uniform flow:

- Upstream propagating waves in the range $-1/(1-M_0) < k_x/k_0 < -1$ propagate subsonically relative to the flow in the lower boundary layer, thus being cut-off and decaying away from the surface, whilst propagating supersonically relative to the flow in the outer portion of the boundary layer. In this case the wave tunnels through the flow near the wall until it can propagate in the outer boundary layer. In consequence, an analysis using uniform flow will over predict the pressure generated in the fluid for these negative wave numbers.
- Downstream propagating waves in the range $1/(1+M_0) < k_x/k_0 < 1$ are cut-on at the wall, but cut-off in the main body of the flow, and thus propagate for a short distance away from the surface but decay thereafter. In consequence an analysis based on uniform flow will underestimate the pressure near the wall for these wave numbers.

Chapter 5

5. ACOUSTIC POWER FLOW AND RADIATION IMPEDANCE

In this chapter we consider the power radiated from a vibrating surface for the idealised 2-D situation shown in figure 5.1, namely a single wave number disturbance at the wall radiating through a parallel shear flow. It is shown analytically that the sound power flowing away from the surface is conserved. The numerical model of Chapters 2-4 is then used to investigate the effect of a finite thickness boundary layer on the radiation impedance and radiation efficiency for the vibrating surface.

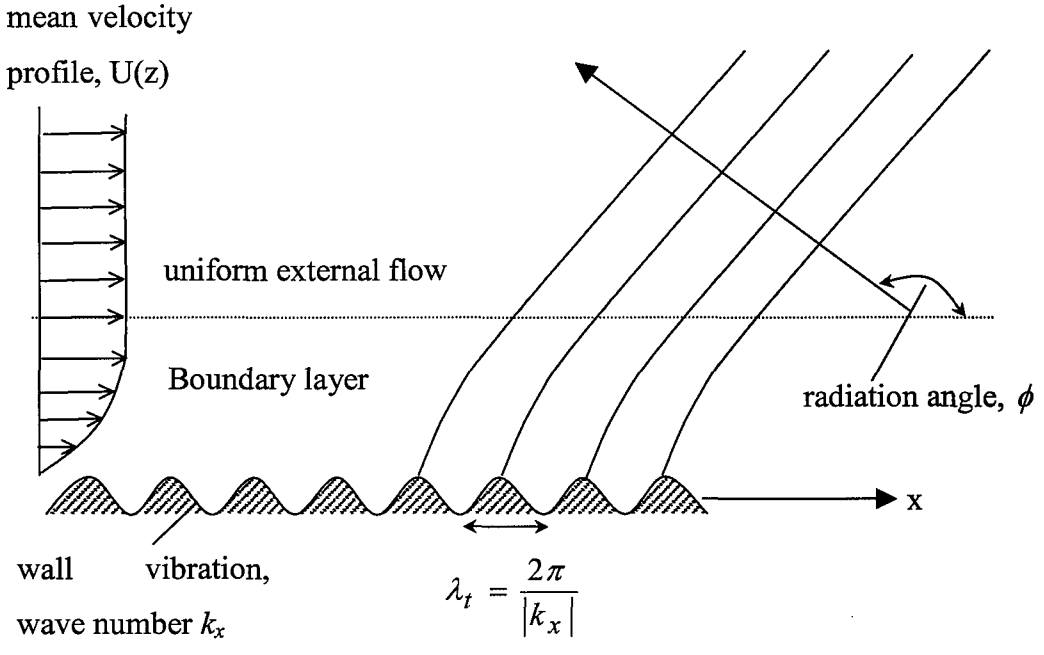

Figure 5.1 Radiation through a boundary layer from surface vibration propagating upstream with wave number k_x

The radiation impedance of a wall vibrating with a single wave number disturbance is discussed in Chapter 11 of Morse and Ingard [3]; this provides a limiting case for the effect of boundary layer thickness discussed in section 5.2.

The radiation efficiency of vibrating plates under a uniform flow has been investigated recently by Graham [27], who modelled the radiation impedance of particular modes of

vibration using asymptotic methods, and by Frampton [28] who calculated the modal radiation impedance numerically. These papers use the spatial Fourier transform technique employed here, but do not include the effect the shear flow. The model developed here can be used without modification to predict the effect of a boundary layer on the radiation impedance of modes of vibration of a plate. This is suggested as an area for further work in Chapter 10.

5.1 Power flow in a parallel shear flow

For sound propagation through an arbitrary mean flow field, with local Mach number given by the vector $\mathbf{M}$, Morfey [27] shows that a logical definition of intensity is given by equation (5.1).

$$\mathbf{I}(x_0, y_0, z_0, t) = p\mathbf{u}^* + (\mathbf{M}\cdot\mathbf{u})(\mathbf{M}p^* + \rho c\mathbf{u}^*) + \mathbf{M}\frac{p^2}{\rho c} \tag{5.1}$$

Intensity defined in this way is shown to be conserved for a range of flow conditions, although not normally for rotational flows such as shear layers. Tester [29] shows that power is not conserved through a shear flow for the case of a sound incident on the wall of a lined duct, where the axial wave number is complex, but for a hard walled duct concludes that the power flow into the wall is conserved because it is zero. It remains to be proven therefore whether or not sound radiated through a shear layer from a vibrating surface is conserved.

In (5.1) the acoustic pressure p and particle velocity $\mathbf{u}$ are real variables with arbitrary time dependence, and $\mathbf{I}(t)$ is interpreted as the instantaneous energy flux vector associated with the sound field. Taking the z-component of (5.1), normal to the parallel flow $U(z)$ under consideration, and taking the time average for a single frequency solution, the power radiated per unit area through any plane $z = z_0$ is obtained as

$$W_{rad}(z_0) = \frac{1}{2}\mathrm{Re}\left((p + \rho U u_x)u_z^*\right)_{z=z_0} \tag{5.2}$$

where u_x is the x-component of the acoustic particle velocity, which from (2.4) is given by

$$u_x = \frac{1}{\overline{D}}\left(\frac{jk_x p}{\rho_0} - u_z \frac{dU}{dz}\right) \tag{5.3}$$

Note that (p, u_x and u_z) are now complex variables with $e^{j\omega t}$ time dependence. Combining (5.3) and (5.2) and rearranging terms leads to

$$W_{rad}(z) = \frac{1}{2}\mathrm{Re}\left(\frac{j\omega p u_z^*}{\overline{D}} - \frac{\rho U |u_z|^2}{\overline{D}}\frac{dU}{dz}\right) \tag{5.4}$$

Because $\overline{D} = j(\omega - k_x U)$, the term $\frac{\rho U |u_z|^2}{\overline{D}}\frac{dU}{dz}$ is an imaginary quantity, the real part of which is zero. Noting also that equation (2.11) gives $u_z = \overline{D}q$, equation (5.4) simplifies to

$$W_{rad}(z) = \frac{1}{2}\mathrm{Re}\left(-j\omega p q^*\right) = \frac{1}{2}\mathrm{Re}\left(j\omega p^* q\right). \tag{5.5}$$

To investigate whether power is conserved through the shear flow, equation (5.5) is differentiated with respect to z to give

$$\frac{dW_{rad}}{dz} = \frac{1}{2}\mathrm{Re}\left(j\omega\left(\frac{\partial p^*}{\partial z}q + p^*\frac{\partial q}{\partial z}\right)\right) \tag{5.6}$$

Using equations (2.14a) and (2.14b) leads to

$$\begin{aligned}\frac{dW_{rad}}{dz} &= \frac{1}{2}\mathrm{Re}\left(j\omega\left(\rho_0\overline{D}^2|q|^2 + \frac{1}{\rho_0\overline{D}^2}\left(\frac{\overline{D}^2}{{c_0}^2} + {k_x}^2 + {k_y}^2\right)|p|^2\right)\right) \\ &= 0\end{aligned} \tag{5.7}$$

Equality to zero follows since all terms in (5.7) are real except for $j\omega$, so that $\frac{dW_{rad}}{dz}$ is the real part of an imaginary quantity. Thus, for the single real valued wave number ideal-fluid solutions considered here, with the sound speed c_0 taken as real, W_{rad} is constant and the definition of acoustic intensity in (5.1) leads to exact conservation of acoustic energy through the parallel shear flow of the boundary layer.

5.2 Radiation impedance and radiation efficiency

In this section the conservation of power flow through a boundary layer demonstrated above is used to relate the radiation efficiency of a vibrating surface under a boundary layer to the radiation impedance of the surface. If power were not conserved then the radiation efficiency would not be well defined.

5.2.1 Definitions and formulae

The radiation impedance of a vibrating boundary is defined as the complex ratio of pressure and normal particle velocity at the boundary. This may be related to the other acoustic parameters defined in Chapter 2 as follows:

$$Z_{rad} = \frac{p(0)}{u_z(0)} = \frac{p(0)}{\overline{\overline{D(0)}}\overline{\overline{q(0)}}} = \frac{\chi(0)}{\overline{\overline{D(0)}}} \tag{5.8}$$

Morse and Ingard [3], page 707, show that when there is no boundary layer, and an infinite plane wall radiates directly into an adjacent uniform flow, the radiation impedance is given by

$$Z_{rad} = \frac{j\rho c(c_t - U_0)^2}{|c_t|\sqrt{c^2 - (c_t - U_0)^2}} \tag{5.9}$$

where $c_t = \frac{\omega}{k_x}$ is the trace wave speed. In the next section, equation (5.9) will provide a useful reference for comparison with the results of the numerical model as $\delta / \lambda \to 0$.

For supersonic waves ($|k_x|/k<1$) the angle of radiation into the flow, ϕ, is a real quantity related to the trace wave speed by

$$\cos\phi = \frac{c}{c_t - M_0 c} \quad . \tag{5.10}$$

For these waves equation (5.9) may be written

$$Z_{rad} = \frac{\rho c}{(1+M_0\cos\phi)\sin\phi} \tag{5.11}$$

It is also useful, for the purposes of later chapters, to write the radiation impedance as a function of k_x:

$$Z_{rad} = \frac{j\rho c(\omega - U_0 k_x)^2}{\omega\sqrt{c^2 k_x^2 - (\omega - U_0 k_x)^2}} \tag{5.12}$$

The radiation efficiency of a vibrating surface is defined as

$$\sigma = \frac{W_{rad}}{\rho c < u_w^2 >} \tag{5.13}$$

where $< u_w^2 >$ is the spatially averaged mean square wall velocity and W_{rad} is the power radiated per unit area of the surface. For the situation shown in Figure 5.1, where an infinite plane wall vibrates in a travelling-wave pattern, the mean square wall velocity is the same at all points on the wall, and $< u_w^2 >= \left(\frac{1}{2}|u_z|^2\right)_{z=0}$.

Because power is conserved in this case, W_{rad} may be calculated from the power radiated at the wall. The radiation efficiency is thus given by

$$\sigma = \left(\frac{2W_{rad}}{\rho c u_z u_z^*} \right)_{z=0} = \mathrm{Re}\left(\frac{Z_{rad}}{\rho c} \right) \tag{5.14}$$

5.2.2 Numerical results for varying δ / λ

With a boundary layer of finite thickness the flow velocity at the wall is zero so that $\overline{D(0)} = j\omega$ and so equation (5.8) may be written

$$Z_{rad} = \frac{\chi(0)}{j\omega} \tag{5.15}$$

Figure 5.2 shows the radiation impedance as a function of wave number for a boundary layer with $\delta / \lambda = 0.1$ and $M_0 = 0.6$, compared with the $\delta / \lambda \to 0$ limit defined by (5.9). The radiation efficiency for surface waves propagating with the flow is hardly affected at all by the boundary layer, but radiation efficiency for waves propagating against the flow is significantly reduced, particularly near the cut-off wave number $\frac{k_x}{k_0} = \frac{-1}{(1-M_0)}$.

The effect of boundary layer thickness on the radiation impedance is further demonstrated in figure 5.3 by comparing solutions for four values of δ / λ ranging from 0.01 to 10. The same results are replotted on a logarithmic scale in figure 5.4. For a thin boundary layer with δ/λ = 0.01 the radiation impedance is close to the uniform flow solution, with peaks in radiation efficiency close to $\frac{k_x}{k_0} = \frac{\pm 1}{(1 \pm M_0)}$, as expected. As the boundary layer thickness increases, the peak in radiation efficiency for the negative wave numbers shifts towards $k_x / k_0 = -1$. This is because waves with $k_x / k_0 < -1$ are cut-off near the wall and only radiate by tunnelling. As a result the efficiency with which waves are radiated at the grazing angle in the upstream direction, where $\frac{k_x}{k_0} = \frac{-1}{(1-M_0)}$, falls rapidly as δ/λ increases. This has implications for the active control of low order modes in engine intake ducts, as outlined in Chapter 10.

For downstream travelling waves the peak in radiation efficiency at $\frac{k_x}{k_0} = \frac{1}{(1+M_0)}$ does not similarly shift towards the zero-flow position, $k_x / k_0 = +1$, as the boundary layer thickness increases. This is because waves with $\frac{k_x}{k_0} > \frac{1}{(1+M_0)}$ are cut-off in the uniform flow region. No power is radiated through the boundary layer (or at the wall, since power is conserved), and the real part of the radiation impedance is zero. At the same time, the imaginary part of the radiation impedance for $\frac{k_x}{k_0} > \frac{1}{(1+M_0)}$ shows an oscillatory behaviour indicative of boundary layer modes, as was mentioned in the discussion of Figure 4.4b). In this wave number region the displacement impedance χ switches from a large positive to a large negative value at points through the boundary layer; the imaginary part of the radiation impedance switches from positive to negative at values of k_x/k_0 where this occurs at the wall. Such oscillatory behaviour of the reactive wall impedance can be suppressed by introducing a small imaginary component in the sound speed c_0 (representing fluid damping), and allowing δ / λ to become large. For further details see Section 5.3.

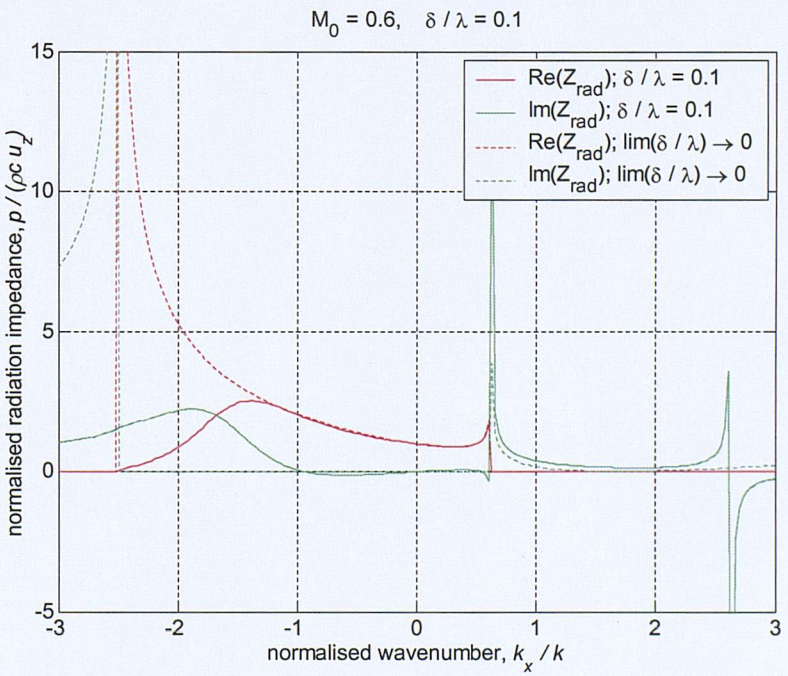

Figure 5.2 Radiation impedance at M_0=0.6 , δ/λ=0.1 compared with limit as $\delta / \lambda \rightarrow 0$

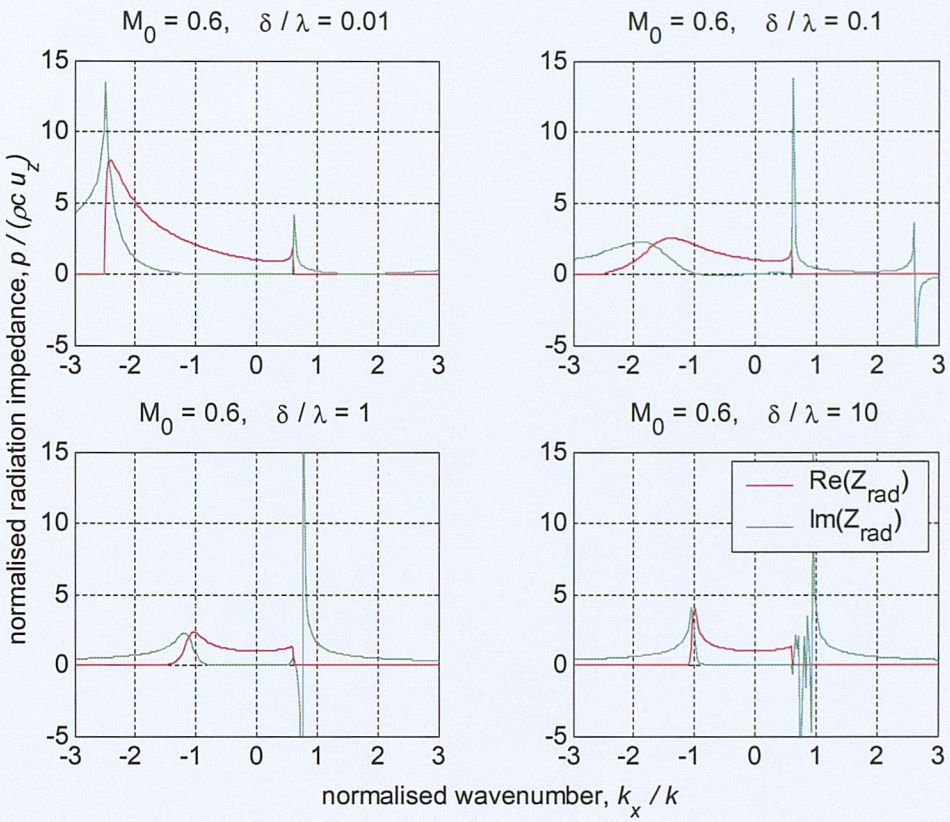

Figure 5.3 Radiation impedance at M_o=0.6 for a range of δ/λ values

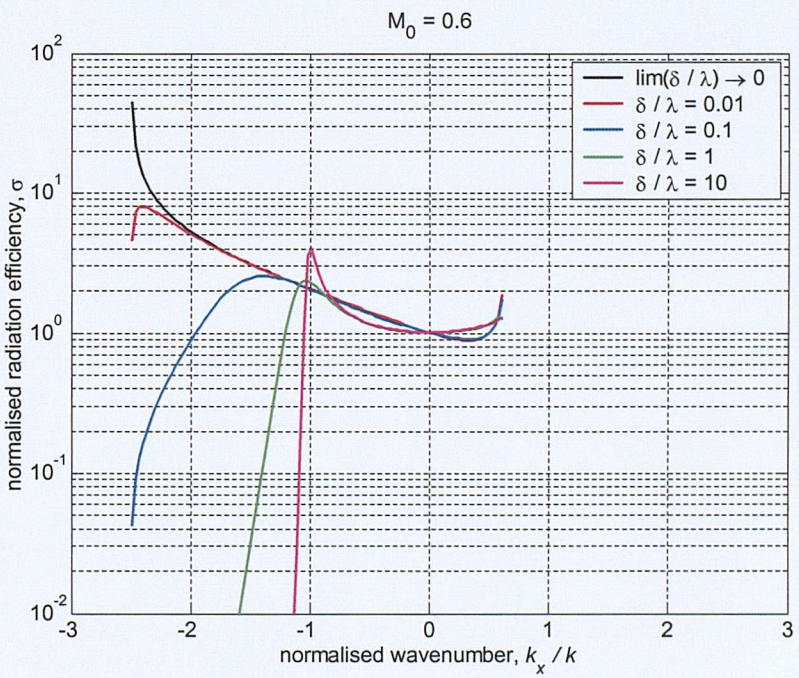

Figure 5.4 Radiation efficiency at M_0=0.6 for four values of δ/λ. Radiation efficiency is zero outside the range shown.

5.3 Effect of fluid damping on radiation impedance

For thick boundary layers (δ/λ large), figure 5.4 shows that the real part of the radiation impedance converges to the zero flow value for upstream propagating surface waves (negative wave numbers), but for downstream-travelling waves the radiation resistance is zero for $\frac{k_x}{k_0} > \frac{1}{(1+M_0)}$ and does not converge to the zero flow solution.

Adding damping to the fluid, in the form of a complex speed of sound, permits acoustic energy radiation from the wall for all wave numbers up to and beyond $k_x/k_0 = 1.0$, resulting in a non-zero radiation resistance and suppressing the reactance oscillations mentioned on page 62. This is demonstrated in figure 5.7, where results for $\delta/\lambda = 10$ with and without damping and with and without flow are compared. For the damped cases the imaginary part of the speed of sound is 3% of the real part.

In the absence of flow (lower graphs), damping replaces the singularities in radiation impedance at $k_x/k_0 = \pm 1$ with finite peaks. With flow (upper graphs) the major effect is to modify the radiation impedance in the range $\frac{1}{(1+M)} < \frac{k_x}{k_0} < 1$, suppressing the strong reactive peaks and giving a positive real part to the radiation impedance, similar to the damped zero flow case.

Comparison of the two damped cases (right hand graphs) demonstrates the similarity of solutions with and without flow for a damped fluid. Physically, the damping in the fluid means that the radiation impedance of the surface is controlled by the low-speed mean flow near the boundary as δ/λ becomes large.

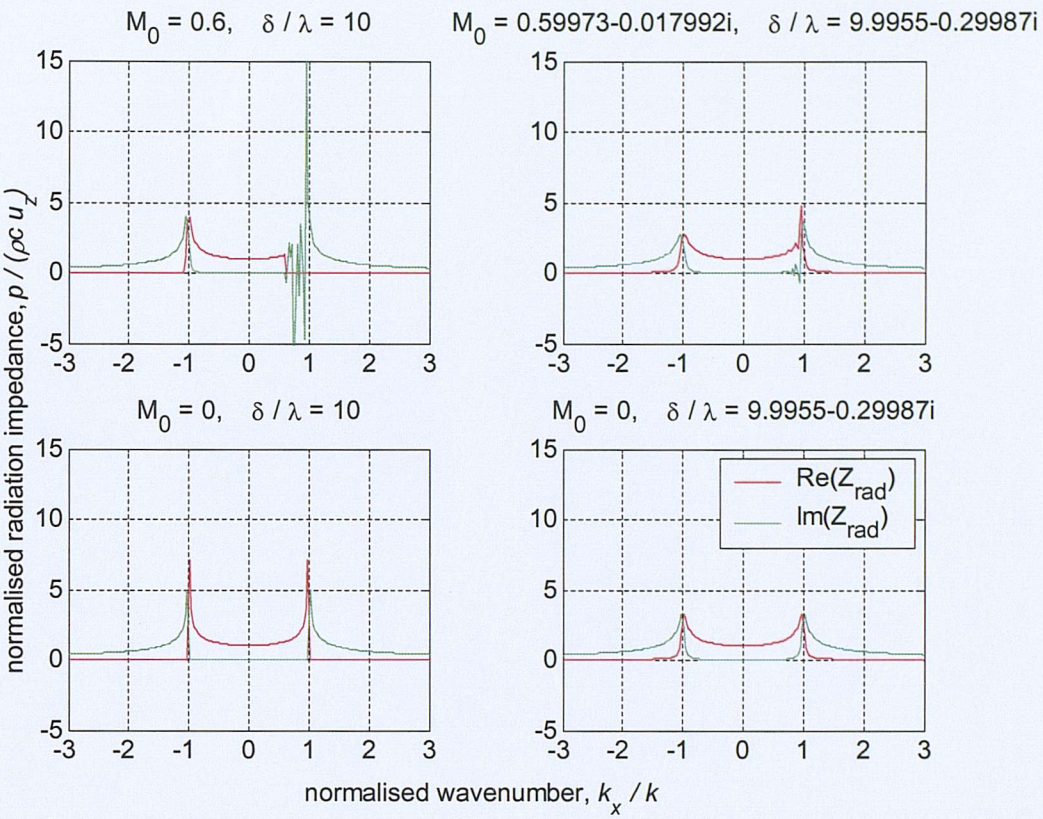

Figure 5.5 Effect of fluid damping at δ/λ =10; comparison of radiation impedances with and without flow, and with and without damping.

5.4 Conclusions

An important result of this chapter is that the flow of acoustic power through a shear layer is conserved. As a result a radiation efficiency based on the radiation impedance of the surface is well defined.

The radiation efficiency is shown to be a strong function of the boundary layer thickness for surface waves propagating upstream near coincidence. This effect may be of concern for active control techniques aimed at low order upstream-propagating modes in aero-engine intakes. In addition it is clear that the plate modal radiation impedances calculated by Frampton [28] will be modified.

An interesting feature of the results for thick boundary layers is that the radiation efficiency of waves propagating against the flow converges towards the zero flow value; whereas for

downstream propagating waves no power is radiated by the surface in the wave number range $\frac{1}{(1+M)} < \frac{k_x}{k_0} < 1$, unless there is damping in the fluid, because these waves are cut-off in the region of uniform flow.

Chapter 6

6. SOUND RADIATION FROM A VIBRATING PISTON IN A PLANE SURFACE: FORMULATION OF THE PROBLEM

Whereas previous chapters have considered the pressure in the fluid produced by a single wave number disturbance propagating in an infinite surface, we now consider the sound field radiated by a fixed piston-like source of finite size in an otherwise stationary wall. For the purposes of this thesis the source is considered to be a uniform piston, but the method can be applied to any source distribution, e.g. a non-uniform piston or, as noted in the previous chapter, a finite panel vibrating in a particular mode of vibration.

In other respects the situation being modelled is the same as in Chapters 4 and 5; thus the uniform flow region outside the boundary layer extends to $z = \infty$, and the outgoing wave condition is applied at the edge of the boundary layer.

The formulation given here is for 3-D problems, but corresponding 2-D equations can be obtained by setting k_y=0 and only integrating over k_x. The bulk of numerical results presented in the following chapters are for 2-D problems because of the large computational resources that would be required to carry out a similar parameter study in 3-D.

The results presented in this chapter are mainly for zero mean flow, the aim being to demonstrate the principle of the method and to validate it against known analytical results. The effect of non-zero mean flow is considered in the next chapter.

6.1 Formulation using a Fourier transform of the boundary condition and pressure field

For single-frequency excitation by a uniform piston the boundary condition at the wall is specified as

$$u_w(x,y) = 1 \text{ on the piston} \qquad 6.1)$$
$$= 0 \text{ elsewhere}$$

where $u_w(x,y)$ is the complex amplitude of the wall velocity. Typical velocity distributions for a discretized computational domain are shown in figure 6.1.

Fourier transforming $u_w(x,y)$ gives a boundary condition in the wave number domain:

$$u_w(k_x,k_y) = \iint u_w(x,y)e^{-j(k_x x+k_y y)}dxdy \tag{6.2}$$

where the integral extends over the vibrating area. The characteristics of wave number spectra as a function of source location and size are examined in the next section.

In the following discussion it is necessary to distinguish between the pressure generated in the fluid by the component of wall vibration $u_w(k_x,k_y)$, which will be denoted $p(k_x,k_y,z)$, and the numerical solution for the pressure obtained by integrating from an assumed initial condition at the edge of the boundary layer (as described in chapter 4) which will be called $\tilde{p}(k_x,k_y,z)$. There is no confusion for the displacement impedance χ since this is the same for both cases.

The pressure at the wall, $p(k_x,k_y,0)$, generated by the boundary velocity $u_w(k_x,k_y)$, follows from the radiation impedance of the wall. Equation (5.8) gives

$$\begin{aligned} p(k_x,k_y,0) &= Z_{rad}(k_x,k_y)\, u_w(k_x,k_y) \\ &= \frac{\chi(k_x,k_y,0)}{j\omega} u_w(k_x,k_y) \end{aligned} \tag{6.3}$$

At other z-locations the pressure is then given by

$$p(k_x,k_y,z) = \frac{\tilde{p}(k_x,k_y,z)}{\tilde{p}(k_x,k_y,0)}\ p(k_x,k_y,0) \tag{6.4}$$

Outside the boundary layer, $z > \delta$, the solution for $p(k_x,k_y,z)$ is obtained from

$$p(k_x,k_y,z) = p(k_x,k_y,\delta)\,e^{jk_z(z-\delta)} \tag{6.5}$$

where k_z is the z-wave number in the uniform flow, as given by equation (3.6).

Finally the pressure field in the (x,y) plane at height z above the wall, $p(x,y,z)$, is obtained from the inverse transform of $p(k_x,k_y,z)$:

$$p(x,y,z) \;=\; \frac{1}{(2\pi)^2}\iint p(k_x,k_y,z)e^{j(k_x x+k_y y)}dk_x dk_y \tag{6.6}$$

where the integral extends (in principle) over all wave numbers. The factor $1/(2\pi)^2$ is included since the integrals are expressed in terms of wave number rather than spatial frequency; this factor is not required in MATLAB programs.

At the wall, z=0, it is convenient for the purposes of the next Chapter to combine equations (6.3) and (6.6) to give the pressure in terms of the local displacement impedance and the wave number spectrum of the wall velocity:

$$\begin{aligned} p(x,y,0) &= \frac{1}{(2\pi)^2}\iint Z_{rad}(k_x,k_y)u_w(k_x,k_y)e^{j(k_x x+k_y y)}dk_x dk_y \\ &= \frac{1}{(2\pi)^2}\iint \frac{\chi(k_x,k_y,0)}{j\omega}u_w(k_x,k_y)e^{j(k_x x+k_y y)}dk_x dk_y \end{aligned} \tag{6.7}$$

It is worth noting here that if the pressure field $p(x,y,z)$ is only required at $z=0$, then only the governing equation for χ, equation (2.32a), need be solved. If the pressure field in the body of the fluid is also required then equation (2.32b) must also be solved.

The power radiated by the piston is calculated by rearranging equation (5.14) and integrating over all wave numbers for which Z_{rad} has a non-zero real part, as shown for example by Cremer and Heckl [35].

$$W_{rad} = \frac{1}{2(2\pi)^2} \iint \mathrm{Re}(Z_{rad}(k_x, k_y)) \left| u_w(k_x, k_y) \right|^2 dk_x dk_y \qquad (6.8)$$

6.2 Numerical implementation using a discrete Fourier transform: spatial resolution, and image sources

Because the wall vibration is taken to be zero outside of the area of the piston, the integrals in the forward Fourier transform, equation (6.2), can be evaluated exactly for any values of k_x and k_y, although in practice an approximate numerical integral is performed. There may be some merit in performing an analytical Fourier transform since this would enable the wave number characteristic of the source to be represented exactly for sources of arbitrary size, whereas using a numerical method source resolution is determined by the digitisation rate.

The inverse Fourier transform in (6.6) requires integration over an infinite wave number domain and for computational reasons it is necessary to limit the integration to a finite range of wave numbers either side of zero. This implicitly requires two approximations:

a) wave numbers which are well cut-off and decay rapidly away from the surface will be neglected. This has the effect of reducing the resolution with which fine-scale features in the spatial domain can be resolved, particularly in the immediate vicinity of the source. Depending on the range of wave numbers considered, the waves with a critical layer will only occur at high Mach numbers.
b) the integrand in (6.6) will only be evaluated at a finite number of equally spaced wave number points so that the continuous Fourier transform is approximated by a discrete Fourier transform. In particular a fast Fourier transform (FFT) routine may be used.

Discretization of the spatial domain, and hence the wave number domain, implies that the source is periodic with image sources outside the spatial region of interest. These images perturb the sound field near the edge of the main spatial domain. The separation distance of the image sources is inversely proportional to the discrete wave number spacing.

The steps in the numerical solution process may be summarised as follows:

1. The solution domain size L, the source dimension $2a$ and the velocity distribution $u_w(x,y)$ are specified. In the examples below, the piston is either a strip (2D radiation) or square (3D) with a denoting the half width.
2. The domain is discretized into N points (where typically N =2048 in each direction for 3D problems, N = 8192 for 2D problems at low Mach number and N =16384 points at high Mach number).
3. The wall boundary velocity distribution $u_w(x,y)$ is Fourier transformed using (6.2) to give $u_w(k_x,k_y)$
4. For each wave number pair (k_x,k_y), starting values for $\tilde{p}$ and $\tilde{q}$ or χ are specified in the uniform flow region and integrated to z=0 using equations (2.32) or (2.14)
5. $p(x,y,z)$ is obtained from the inverse transform given by equation (6.6).

It should be noted that the forward Fourier transform of the wall boundary condition in (6.2) uses $e^{-j(k_x x+k_y y)}$ in the integrand since the convention used for the (x,y,t) dependence of acoustic variables in the equations of chapter 2 is $e^{j(\omega t-k_x x-k_y y)}$. The inverse transform in equation (6.6) uses a plus sign in the exponent. Because MATLAB uses the opposite convention it is necessary to use the inverse Fourier transform routine, IFFT, in implementing equation (6.2) and the forward Fourier transform routine, FFT, in implementing (6.6). Using the incorrect routine for the transforms leads to a solution in which the upstream and downstream directions are swapped. This could have been avoided by using the opposite convention to derive the governing equations.

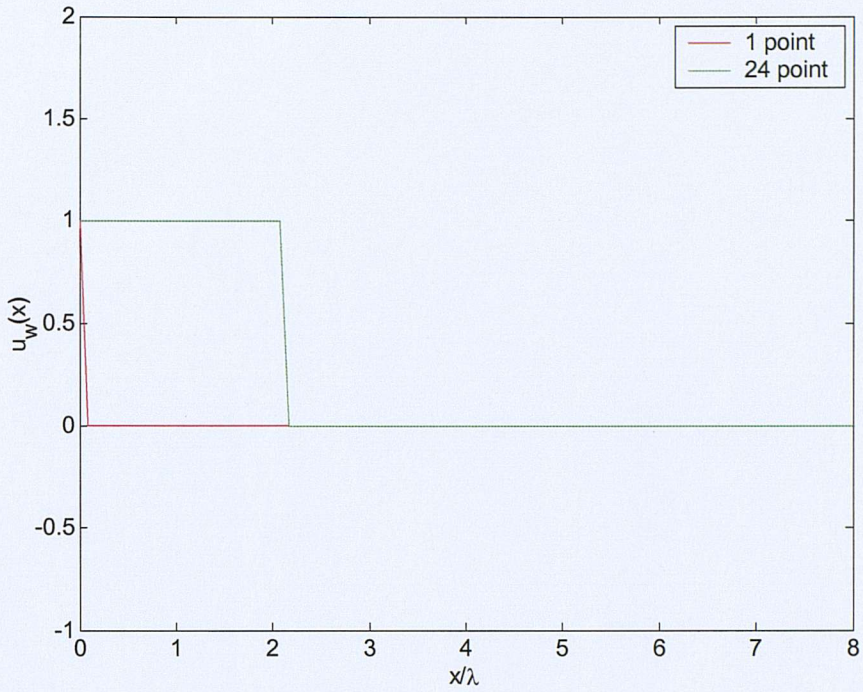

Figure 6.1 Wall velocity distributions for 2D sources located next to x=0 for sources comprising 1 and 24 discretization points. Total domain size is approximately 720 λ.

Typical wave number spectra for 2-D sources of two different sizes located next to the origin, is shown in figure 6.1, are shown in figure 6.2. The non-dimensional source size is given by *ka,* where *a* is the half-width of the 2-D source. The spectrum of the single point source is real valued, but the spectrum for the 24 point source has an imaginary part as the source is not centred at x=0.

For a 2-D line source represented in the spatial domain by a single point (N=1) located at $x = x_0$, or a 3-D point source located at (x_0, y_0), the discrete wave number spectra are respectively:

$$u_w(k_x) = e^{-jk_x x_0}$$

$$u_w(k_x, k_y) = e^{-j(k_x x_0 + jk_y y_0)} \tag{6.9}$$

In both cases $|u_w| = 1$ for all k_x and k_y

The wave number spectrum of a line source located at the mid point of the spatial domain is as shown in figure 6.3. Because of the x-shift relative to figure 6.1 the phase changes rapidly with wave number, and the real and imaginary parts of the spectrum oscillate rapidly from positive to negative; the plots effectively show the envelope of each curve.

Using equation (6.3) the wave number spectrum of the pressure field at the wall may be calculated from the product of the wave number spectrum of the wall vibration and the radiation impedance at the wall. This spectrum is shown in figure 6.4 for the point source; the slight asymmetry occurs because the source is not exactly at the mid point of the spatial domain since this has been discretised by an even number of points.

If the pressure in the body of the fluid is required, then the data in figure 6.4 would need to be used in equation (6.4) to obtain the pressure wave number spectrum at other z locations.

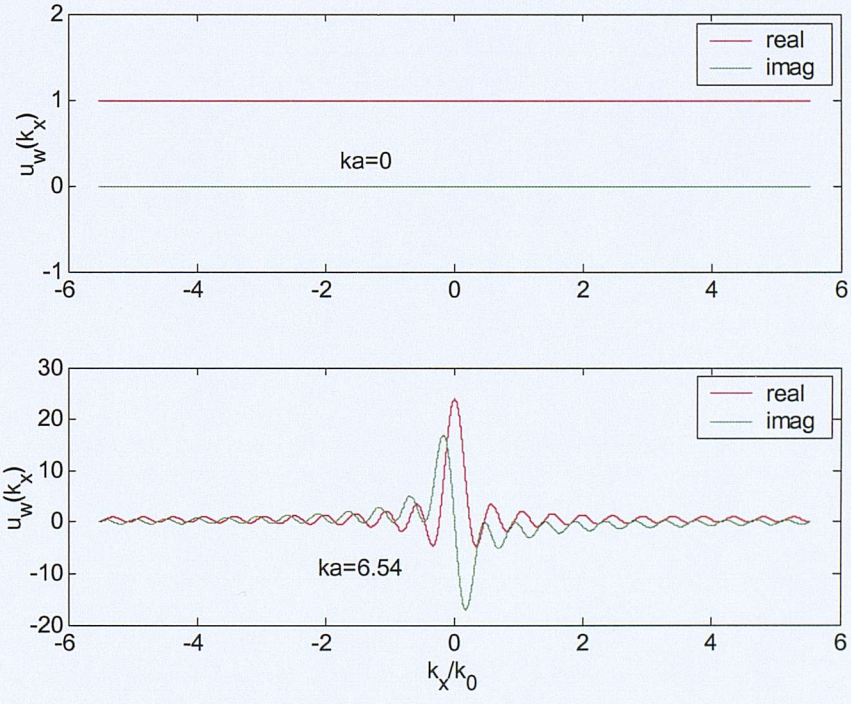

Figure 6.2 Wall velocity wave number distributions for the 2D sources shown in 6.1; ka = 0 for the single point source and ka = 6.54 for the source comprising 24 discretization points.

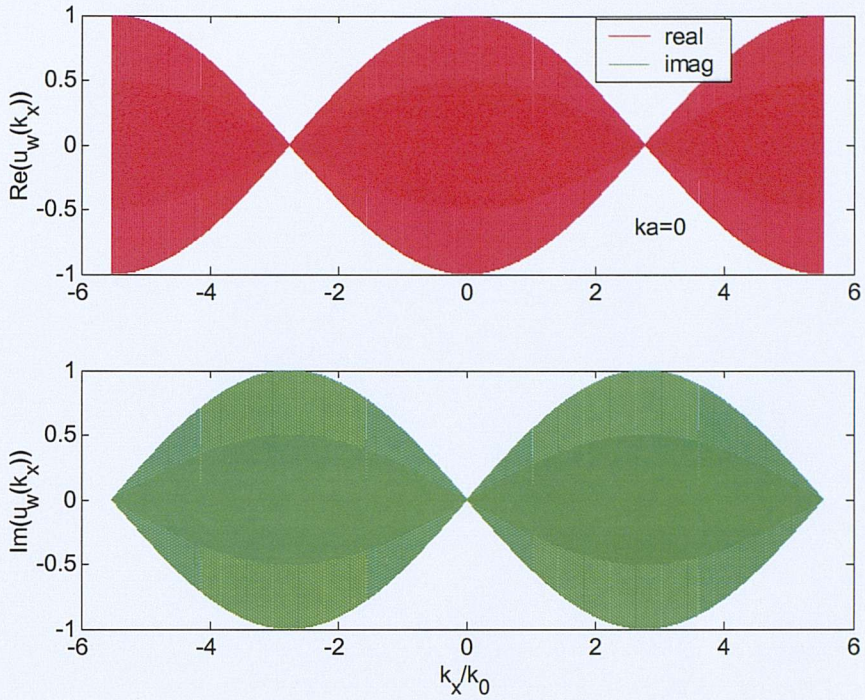

Figure 6.3 Real and imaginary parts of the wall velocity wave number distributions for a point source located close to x=L/2.

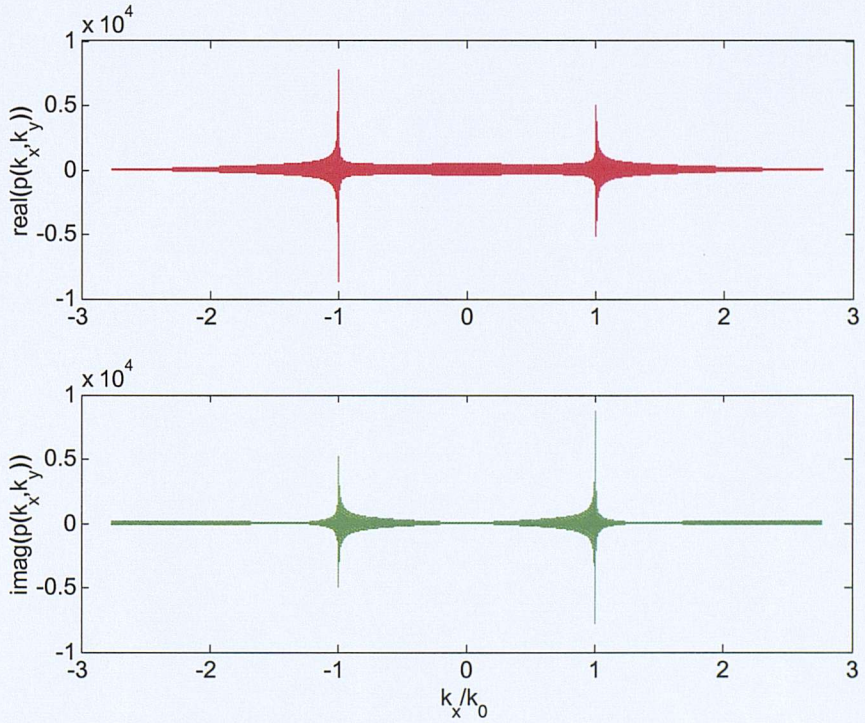

Figure 6.4 Real and imaginary parts of the pressure wave number spectrum at the wall $p(k_x,0)$ for a line source located close to x=L/2; zero mean flow.

6.3 Pressure field around a 2-D source in the absence of flow

Taking the inverse Fourier transform of the data in figure 6.4 gives the the spatial sound field shown in figure 6.5. This is the pressure at the wall, $p(x,z=0)$, radiated by a line source in the absence of flow. The magnitude of the acoustic pressure is a maximum at the source and decays with distance. Because this is a 2-D solution the acoustic pressure reduces at a rate of 3dB for each doubling of distance from the source, a slope which is made apparent by plotting the pressure on a logarithmic x-scale as shown in figure 6.6.

As the edge of the domain is approached the decay rate (shown by the upper edge of the envelope) becomes noticeably smaller as the image sources start to contribute to the overall level. The infinite spatial distribution of image sources creates a 'noise floor' at 90 dB on this scale, so that the dynamic range of the prediction is only about 25 dB. Phase interference also causes an interference pattern between the primary source and its image, shown as the progressively thickening envelope of the solution.

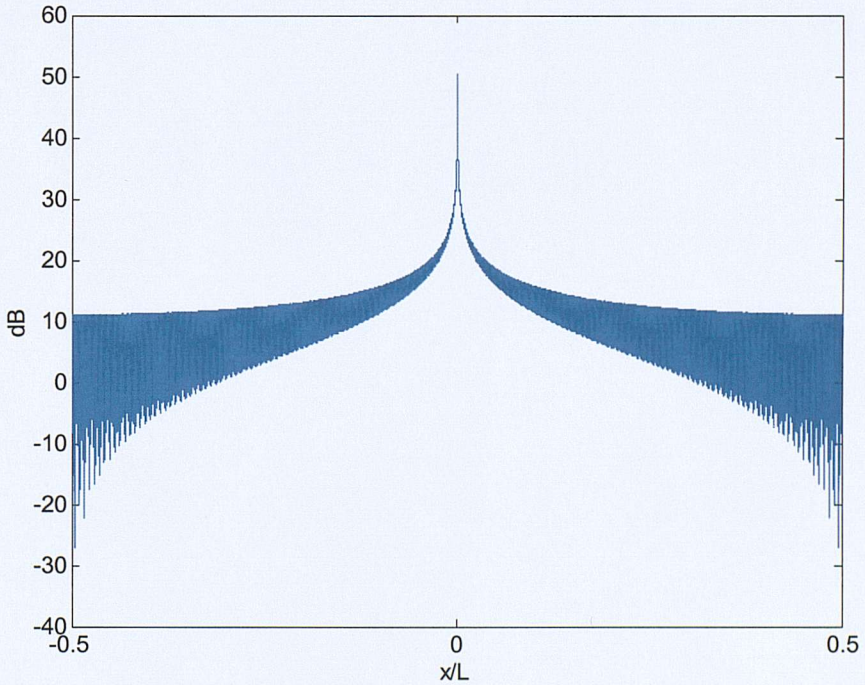

Figure 6.5 Pressure distribution at z=0 around a line source at x=0; 2-D model, no flow.

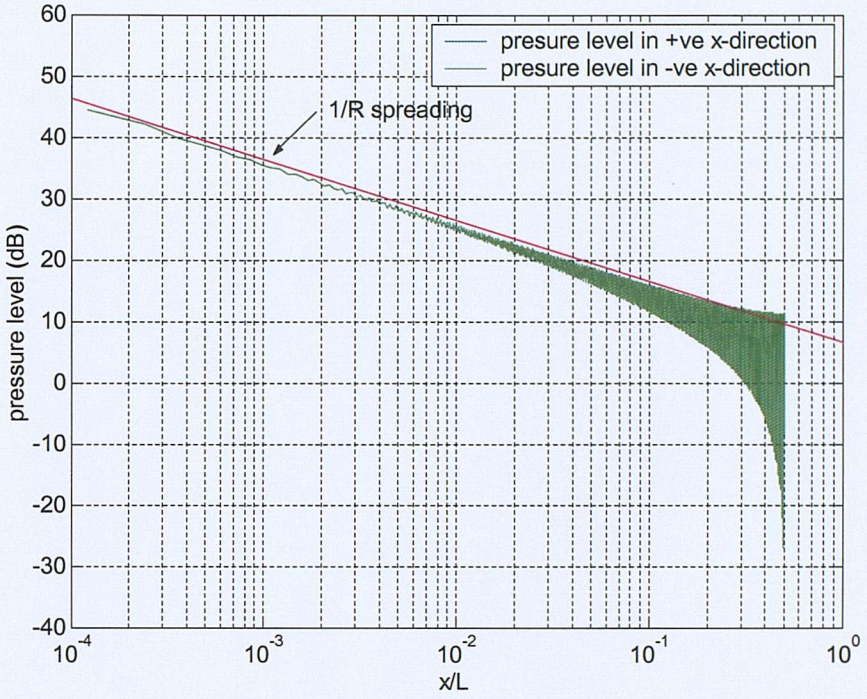

Figure 6.6 Pressure distribution at z=0 *either side of a source at* x=0. *2-D model, zero damping. Red line shows 1/R cylindrical spreading. Solutions in the positive and negative x-directions are identical*

6.4 Effect of fluid damping

It was noted in Chapter 5 that peaks occur in the radiation impedance, and hence in the wall pressure response, when $\frac{k_x}{k_0} = \frac{\pm 1}{(1 \pm M_0)}$, these are apparent in figure 6.4. Depending on the height of the peak this can cause numerical inaccuracies in the FFT, effectively because the peak is not fully resolved in the discrete version of the integral in (6.6). The resolution of the peak in the wave number domain is also linked to the proximity of image sources in the spatial domain, and increasing the number of points in the FFT will therefore increase the dynamic range of the solution.

Another way of controlling these errors is by using a complex speed of sound to include the effect of damping in the fluid; Figures 6.5 and 6.6 are for zero damping. The effect of fluid damping is to cause additional decay of the sound pressure level at locations many

wavelengths from the source, with the result that the 'noise floor' from image sources is greatly reduced.

Figures 6.7 and 6.8 show this effect and demonstrate that, for a complex sound speed with 0.1% imaginary part, and for $|x|<0.01\,L$, which is the region of interest in following chapters, the additional decay with distance from the primary source is negligible. Much 'cleaner' results, with no spatial interference, are produced in this region.

Adding damping also helps to 'clean up' the response in the body of the fluid immediately around the source. Figure 6.9 shows the pressure-level contour plots in the *x-z* plane in the region $|x|<0.012\,L$, $z<0.012\,L$, computed with and without damping. To produce the level for $z>0$ equation 6.6 has been used. With no damping the interference pattern arising from the image sources causes tortuous contours, whereas a small amount of damping gives the clean cylindrical contours expected for this problem.

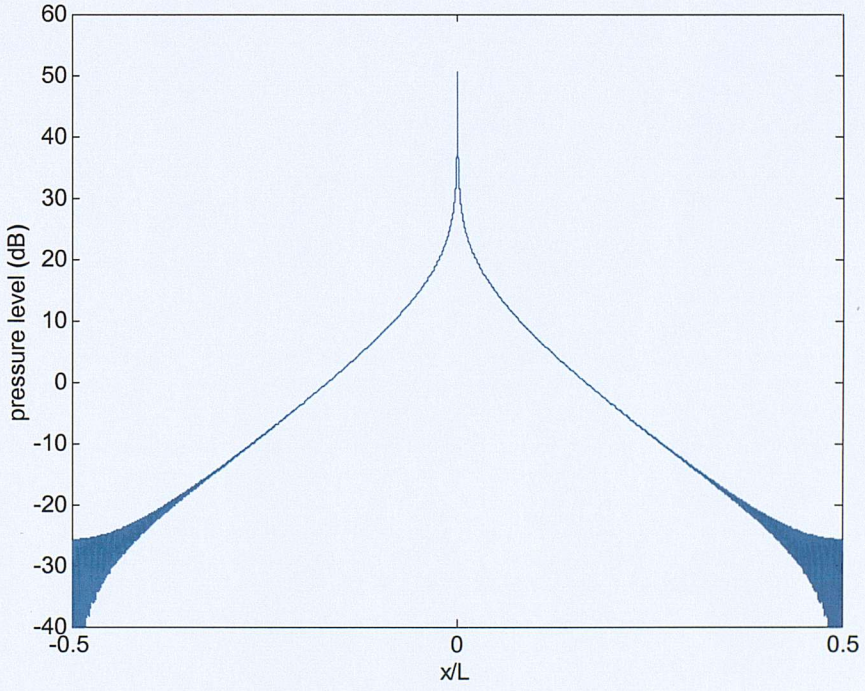

Figure 6.7 Pressure distribution at z=0 around a 2-D line source at x=0; damping due to 0.1% complex speed of sound

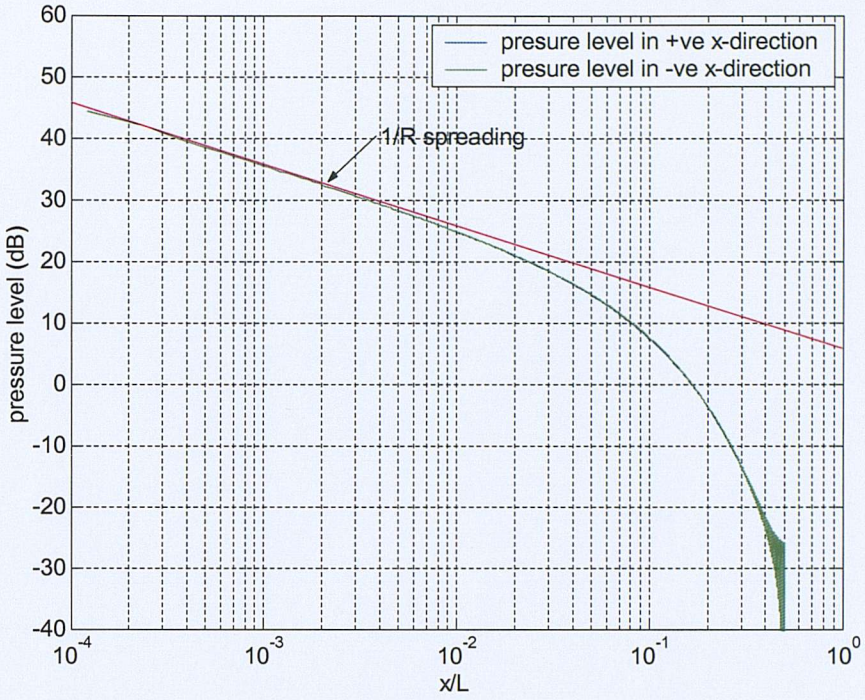

Figure 6.8 Pressure distribution at z=0 *either side of a 2-D line source at* $x = 0$*; damping due to 0.1% complex speed of sound.*

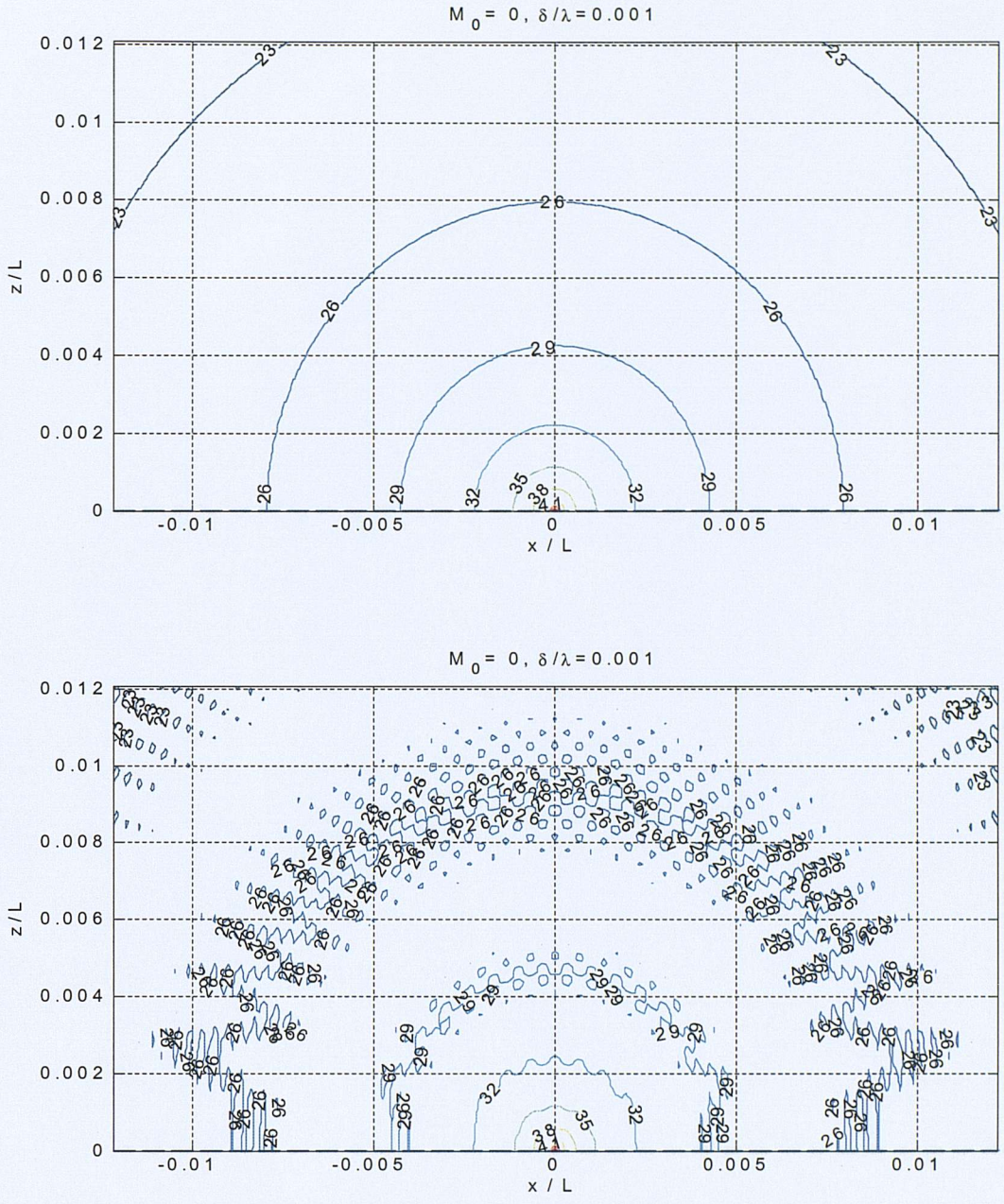

Figure 6.9 effect of damping on pressure contours around a point source. Lower graph has zero damping, upper graph has damping corresponding to $Im(c_0)/c_0$=0.1 %.

6.5 Effect of 2-D source size

A source of size *ka*=0, a line source, is omni-directional in the absence of flow, as shown in figure 6.9. As *ka* increases it is well known [2] that the sound field of a piston becomes progressively more directional, with a strong primary lobe and smaller side lobes. For ka > 3.83 there is a single side lobe, and a second side lobe occurs for ka > 7.01.

Figure 6.10 demonstrates the ability of the method to predict these characteristics for a source with *ka* = 6.54. Such a source is approximately two wavelengths in width, as shown in figure 6.1, and has the wave number spectrum shown in the lower graph of figure 6.2 when located at the origin. The size of the source is only specified to within the discretization spacing, so that the quoted *ka* value is only determined to this accuracy, i.e. about 4% for a source comprising 24 points.

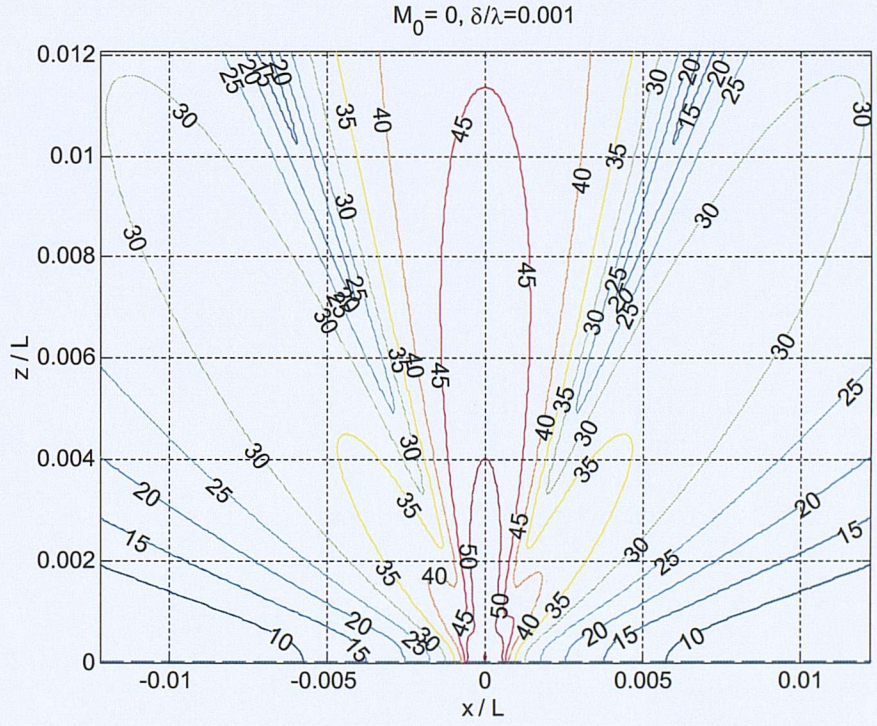

Figure 6.10 SPL contours around a 2-D piston source of size ka=6.54, with zero flow

6.6 Pressure field around a 3D source in the absence of flow

The results presented so far in this chapter have all used the 2-D form of the Fourier transform in equation 6.6. This section now considers a 3-D point source located in the

centre of the *x-y* computational domain. As mentioned in Section 6.2, because of the larger computational requirements in calculating 3-D problems the size of the Fourier transform and the computational domain is reduced compared with 2-D problems.

Figures 6.11 and 6.12 show the result of a zero flow 3-D calculation. As required, the contours in the *x-y* plane are circular. The sound field along the line y=0, z=0 decays as $1/R^2$, 20 dB per factor of 10 change in distance from the source, as shown in figure 6.12.

These results provide a baseline for comparisons with those of Section 7.2 which show the effect of a mean flow and a boundary layer on a 3-D source.

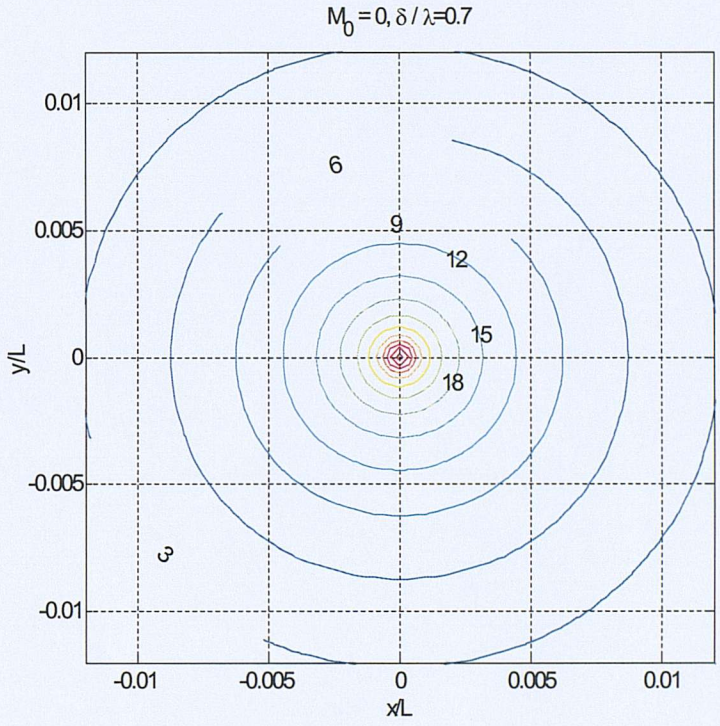

Figure 6.11 Sound pressure level contours at z=0 around the source source centred at x=0, y=0; zero flow.

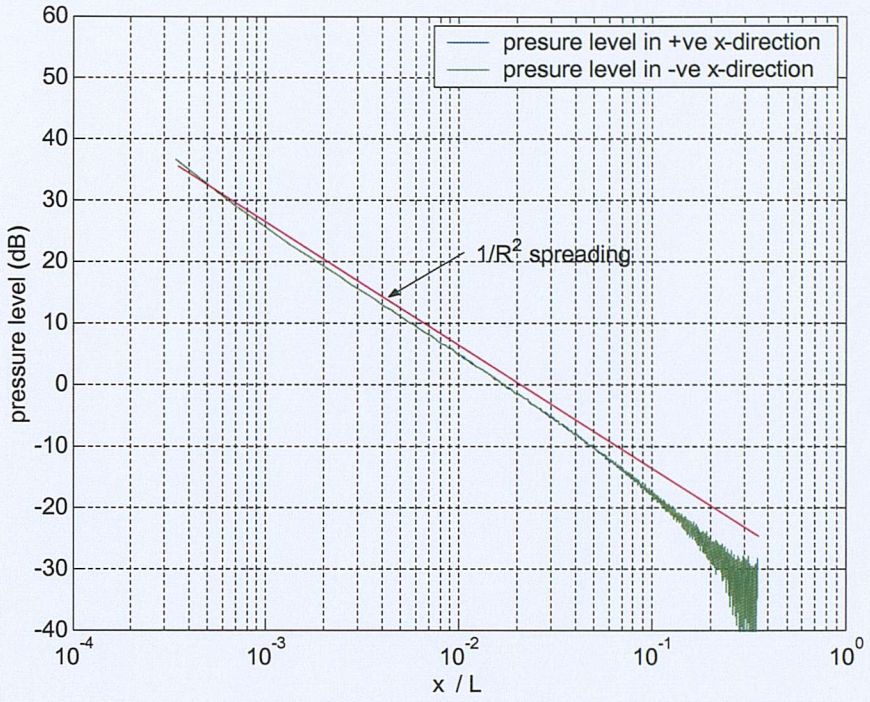

Figure 6.12 Sound pressure level cut along the line y=0, z=0 through the data of figure 6.10

6.7 Windowing in the wave number domain to control leakage effects with flow

So far in this chapter only zero flow problems have been considered, and in that case the magnitude of $Z_{rad}(k_x,k_y)$ and $u_w(k_x,k_y)$, and hence $p(k_x,k_y)$, are all symmetric in k_x and k_y. This symmetry can be seen in figure 6.4.

When there is a non-zero mean flow however $Z_{rad}(k_x,k_y)$ is no longer symmetric in k_x, and hence $p(k_x,k_y)$ is no longer symmetric. Figure 6.13 shows this for a 0.2 Mach number flow over a line source.

Because the spectrum is discontinuous between the maximum positive and negative wave numbers, $\pm k_{x,\max}$, applying the inverse transform to obtain $p(x,y)$ causes 'leakage' [36]. Taking the inverse transform of 6.13 gives the sound field shown in figure 6.14. There are significant non-physical fluctuations in the level which are not removed by adding damping.

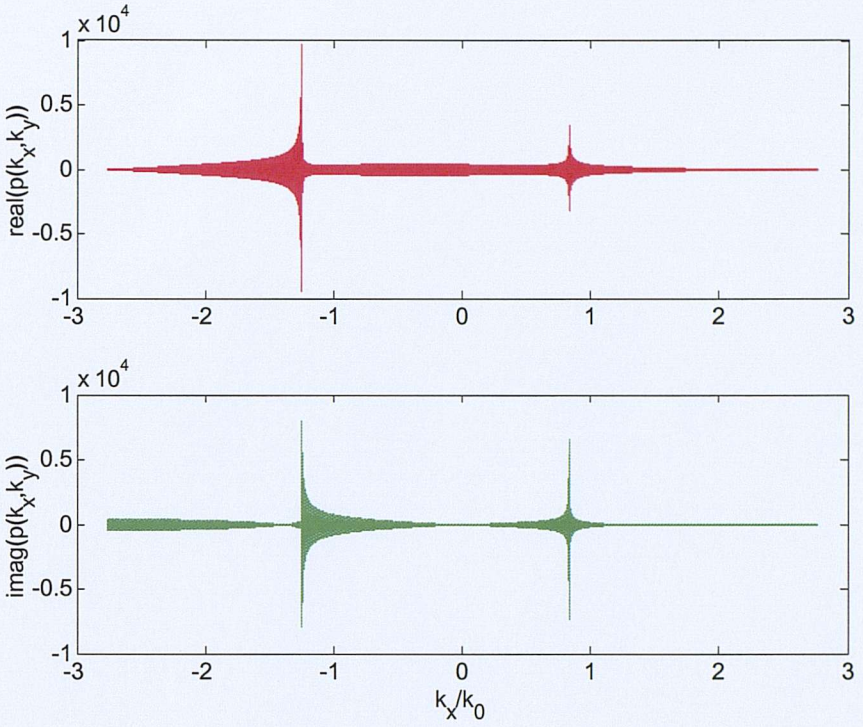

Figure 6.13 Real and imaginary parts of the wall pressure wave number spectrum for a point source located close to x=L/2; Mach 0.2 flow.

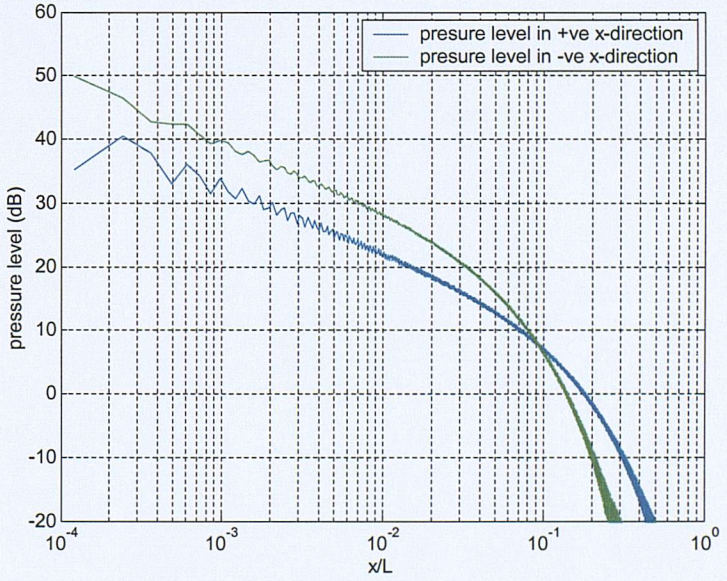

Figure 6.14 Sound field of a line source in the presence of a 0.2 Mach number flow with a thin boundary layer.

Leakage is an effect most commonly observed when Fourier analysing transients which are longer than the capture time window of the transform, and in signal processing the problem is generally cured by applying a window function so that the start and end point of the transient are forced to zero.

Applying this method here, $p(k_x, k_y)$ may be multiplied by a window function $H(k_x, k_y)$ such that $H(k_{x;\max}, k_y)p(k_{x;\max}, k_y) = 0$. Using a Hanning window, figure 6.15 [36], gives the pressure wave number spectrum shown in figure 6.16, and the resultant sound field in the spatial domain shown in figure 6.17. This result should be compared with the un-windowed result in 6.13.

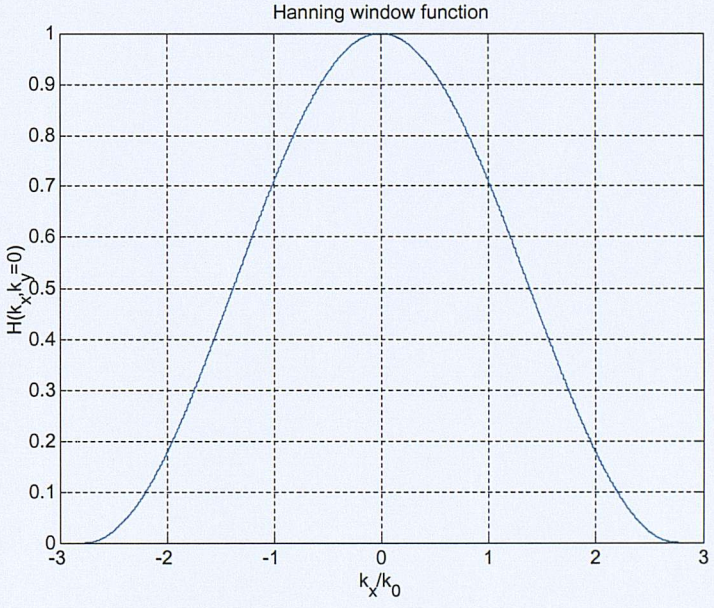

Figure 6.15 The Hanning window function

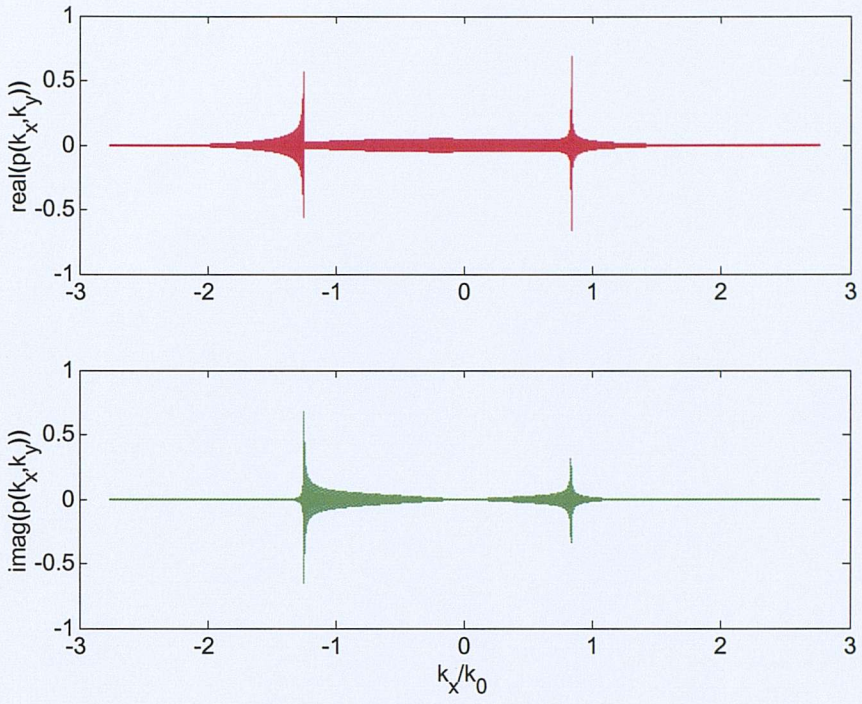

figure 6.16 Windowed pressure wave number spectrum; source at x=L/2, Mach 0.2 flow

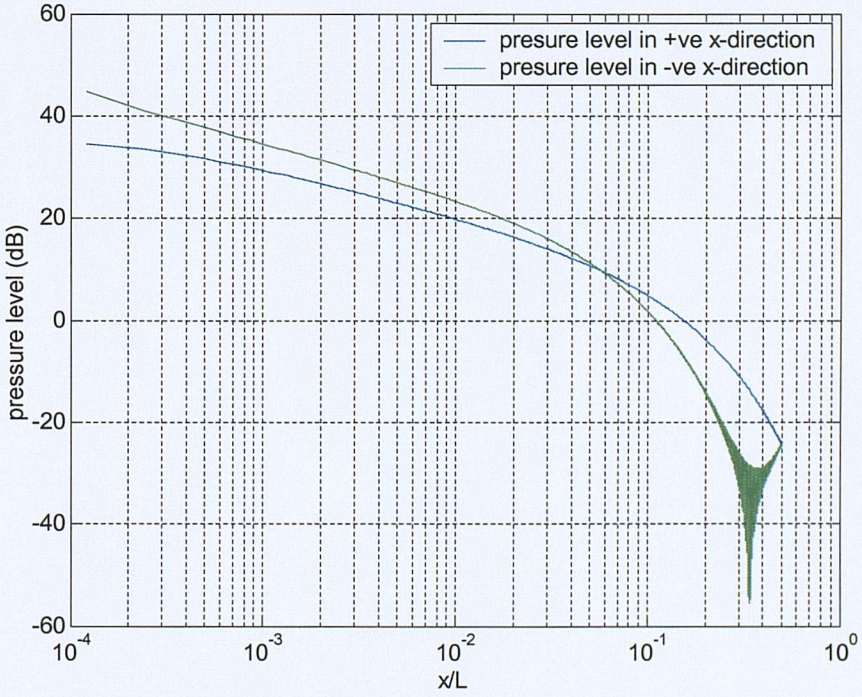

Figure 6.17 Pressure distribution upstream and downstream of a windowed point source; Mach 0.2 flow

This process has been described as an application of the window function to $p(k_x,k_y)$ in equation (6.6). This is equivalent to applying the window function to $u_w(k_x,k_y)$ in equation (6.7), and it is clear that the result shown in figure 6.17 is the pressure field that is produced by a source whose wave number transform is $H(k_x,k_y)u_w(k_x,k_y)$, plotted in figure 6.18. Taking the inverse transform of $H(k_x,k_y)u_w(k_x,k_y)$ gives the spatial distribution of the windowed source, as shown in figure 6.19; the windowing process broadens the point source into a multi-point distribution. This effect is well known from the field of signal processing [36].

There are potentially other window functions which might be more suitable than the Hanning window shown in figure 6.14. For example a window function that had a value of 1.0 for all propagating waves and then dropped to exponentially to zero for higher wave numbers, a cross between a Boxcar window and a Hanning window, would have the useful property that the sound field in the body of the fluid would be relatively unchanged by its application.

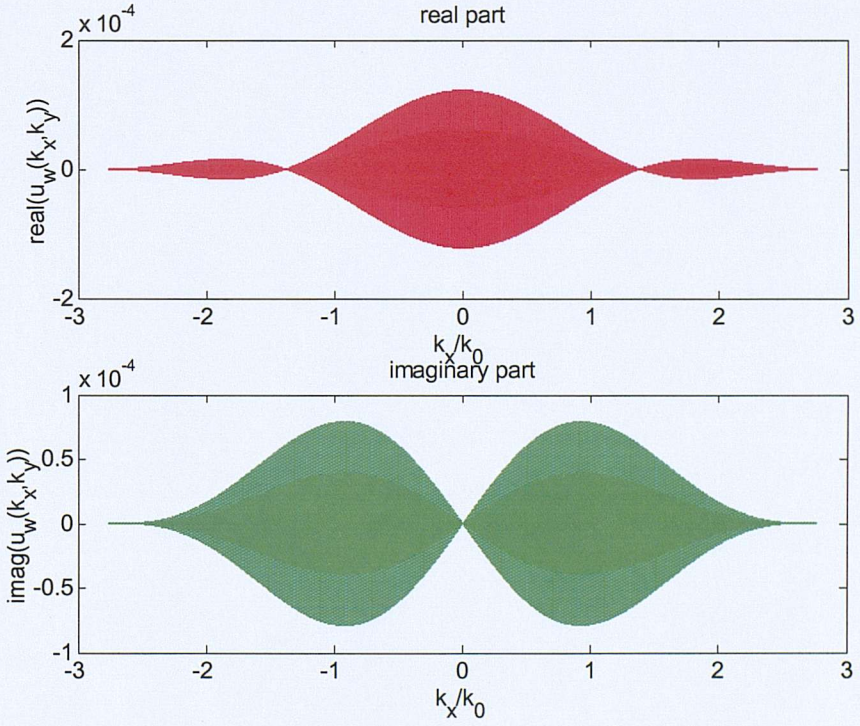

Figure 6.18 Real and imaginary parts of the wall velocity wave number spectrum for a point source located close to x=L/2 after application of a Hanning window

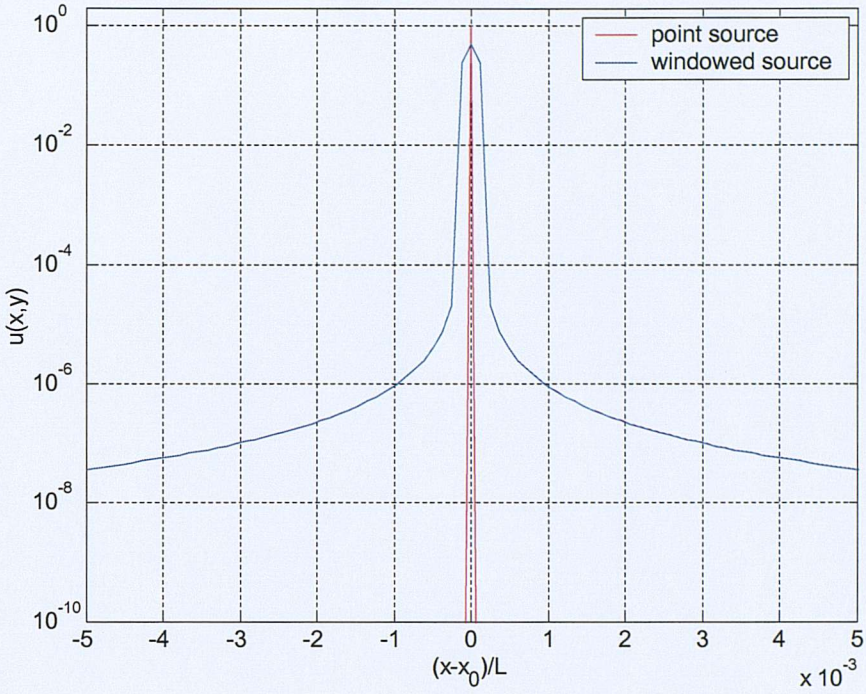

Figure 6.19 Effect of wave number windowing on spatial distribution of a point source

6.7 Conclusions

This chapter has outlined how to obtain the spatial distribution of pressure from the wave number dependent solutions presented in Chapter 4.

It is shown that errors in the predicted sound field can occur because of the necessary compromises in a numerical implementation of the method. Firstly, the discretization of the problem gives rise to image sources and may give poor resolution of coincidence peaks; these errors can be controlled by including damping in the model. Secondly, the asymmetry of the radiation impedance when there is a mean flow leads to 'leakage' in the inverse Fourier transform; these errors can be controlled by windowing the wave number spectrum of the source.

Chapter 7

7. ACOUSTIC FIELD DUE TO A VIBRATING PISTON UNDER A SUBSONIC BOUNDARY LAYER

Chapter 6 demonstrated the ability of the spatial Fourier Transform method to predict the sound field radiated from a vibrating plane surface in the absence of flow. This chapter now considers the effect of a parallel shear flow on the pressure field generated in the fluid, and on the power radiated from the surface.

The effect of uniform flow on the sound radiation from compact pistons has been described previously in a number papers [30,31,32], with both 3-D sources [31] and 2-D strip sources [32] being considered. Specific new analytical results have also been generated by Morfey [33], based on an extension to [34] and [30], to assist in the validation of the numerical results presented here.

Sound radiation from a source in a boundary layer has also been considered recently by Suzuki and Lele [43] who used direct numerical simulation methods (DNS), and compared results with analytically determined low and high frequency limiting cases.

7.1 A line or point source radiating into a uniform flow

As a reference for the validation of numerical results with finite thickness boundary layers in the next section, we first consider the effect of a uniform flow on the pressure and power radiated in the compact limit ($ka \ll 1$). Two methods are considered for finding the power radiated from a vibrating surface into a uniform adjacent flow. The first uses the method of Chapter 6 together with analytical formulae from Morse and Ingard [3] for the radiation impedance. The second method, given in unpublished papers by Morfey [33], gives a full analytical solution for the far field pressure and sound power radiation from compact 2D and 3D sources. These latter results are presented here without proof to allow comparison with results from the first method.

For a 2-D line source located at $x = x_0$ the source spectrum is $u_w(k_x) = e^{-jk_x x_0}$ and the radiation impedance as a function of wave number is given by equation (5.12). Thus equations (6.5) and (6.7) give the pressure field as

$$p(x,z) = \int_{\infty}^{\infty} \frac{j\rho c(\omega - U_0 k_x)^2}{\omega\sqrt{c^2 k_x^2 - (\omega - U_0 k_x)^2}} e^{jk_x(x-x_0)} e^{jk_z z} dk_x \tag{7.1}$$

The power radiated from the line source is given by equation (6.8) and, noting that $|u_w(k_x)| = 1$ for all k_x and that Re(Z_{rad}) is zero outside the range $\frac{-1}{(1-M)} < \frac{k_x}{k} < \frac{1}{(1+M)}$, this may be written

$$W_{rad} = \frac{1}{4\pi} \int_{-1/(1-M)}^{1/(1+M)} \frac{j\rho c(\omega - U_0 k_x)^2}{\omega\sqrt{c^2 k_x^2 - (\omega - U_0 k_x)^2}} dk_x \tag{7.2}$$

It is difficult to evaluate equations (7.1) and (7.2) analytically, but a numerical integration is simple to implement using the QUAD function in MATLAB.

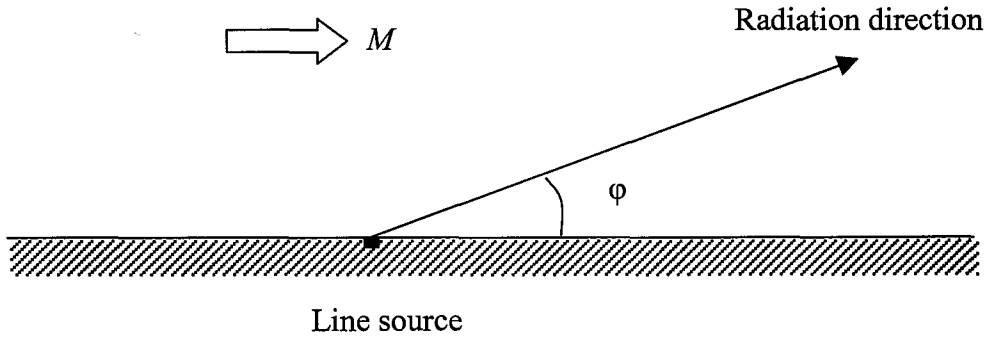

Figure 7.1 Radiation angle from a line source into a uniform mean flow as used in (7.3)

Morfeys result for the far-field pressure and power radiated by a 2-D point source are as follows:

$$p(x,z;M) \approx \frac{p(x,z;0)}{\left(1+M\cos\phi\right)^{5/2}} \tag{7.3}$$

$$W(M) = \frac{1+\frac{1}{2}M^2}{\left(1-M^2\right)^{5/2}} W(0) \tag{7.4}$$

Here $p(x,z;M)$ is the pressure field radiated from the line source with a grazing flow of Mach number M and ϕ is the emission angle relative to the flow direction as shown in figure 7.1. $W(M)$ is the power radiated by the source at Mach number M.

Equation 7.3 provides a simple relationship between the zero-flow and with-flow results in the far field, with convective amplification given by the factor $\left(1+M\cos\phi\right)^{-5/2}$. The near field solution for $p(x,z;0)$ is intricate to solve analytically and so the accuracy of the Fourier transform method is illustrated in figure 7.2 by comparing a zero-flow solution which has been corrected according to (7.3) with an actual with-flow solution from the Fourier Transform method of (7.1).

The solutions are not quite identical with differences of the order of +1dB in the upstream direction and –1dB in the downstream direction. This is due to the damping in the model which, relative to zero flow, gives increased attenuation upstream and decreased attenuation downstream. This effect must be borne in mind when considering plots for non-uniform flow in the next section.

The two methods of predicting power radiated from a line source, using (7.2) and (7.4) are shown to be in perfect agreement in figure 7.3.

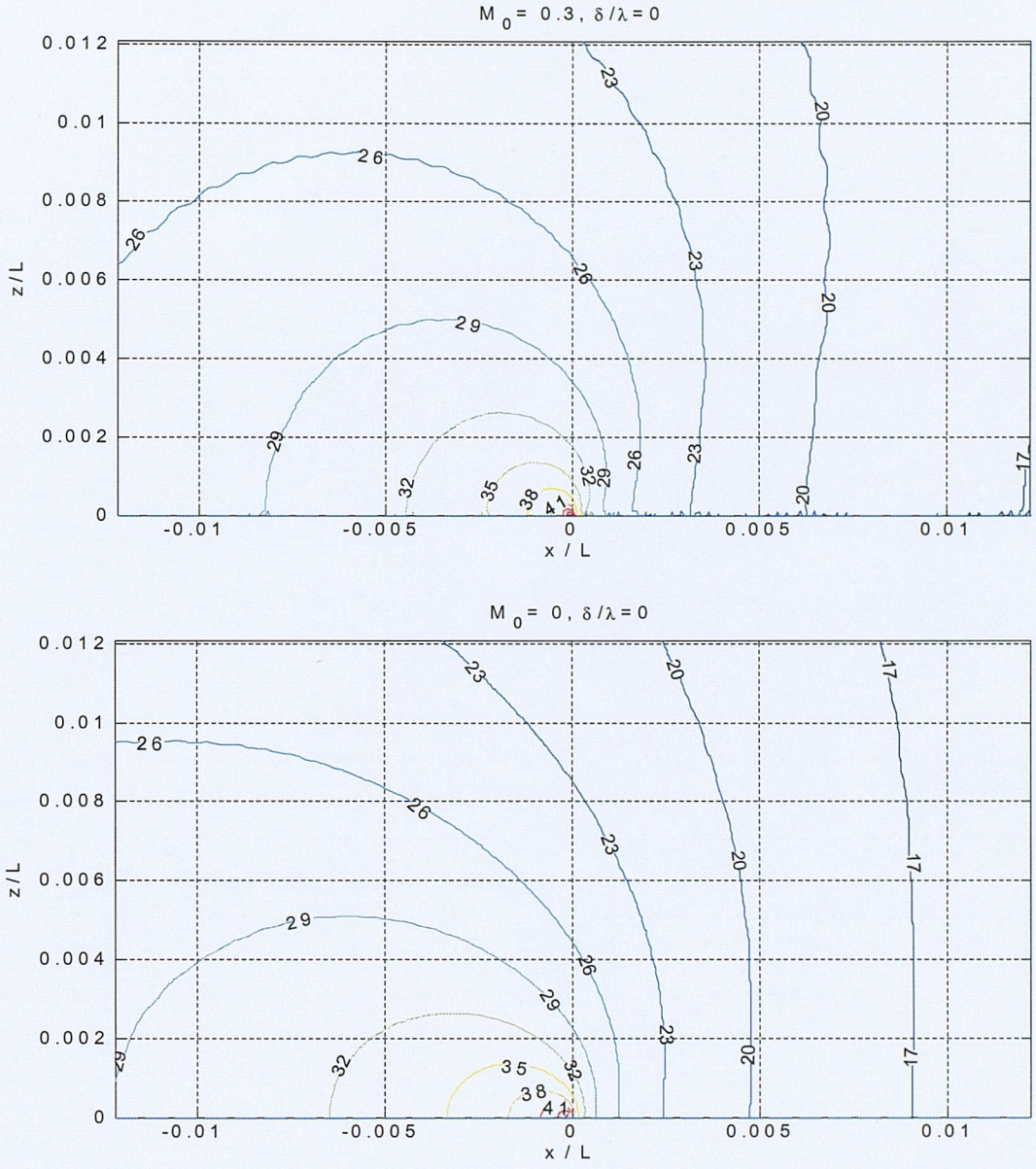

Figure 7.2 convective amplification of a line source under an M_0=0.3 uniform flow; upper graph generated using equation (7.1), lower graph generated using the zero flow result of figure 6.9 and correcting for flow using equation (7.3)

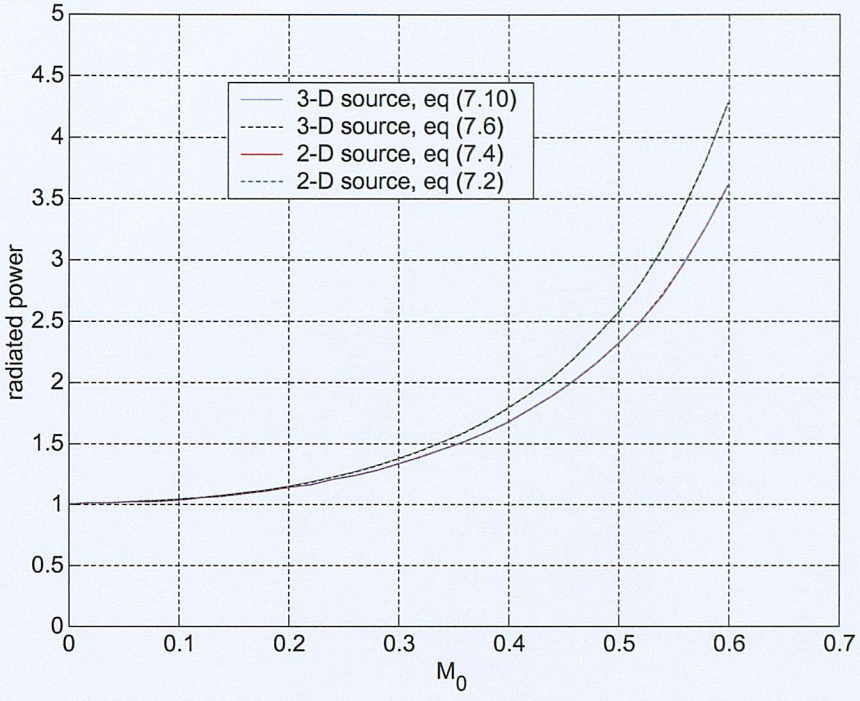

Figure 7.3 Power radiated into a uniform flow from 2-D and 3-D compact sources as a function of Mach number ; comparison of analytical and numerical integral results.

For a 3-D point source located at (x_0, y_0) the wave number spectrum is $u_w(k_x, k_y) = e^{-(jk_x x_0 + jk_y y_0)}$. The radiation impedance needs to be generalised to include k_y and, by inspection of (5.12), may be written:

$$Z_{rad}(k_x, k_y) = \frac{j\rho c(\omega - U_0 k_x)^2}{\omega\sqrt{c^2(k_x^2 + k_y^2) - (\omega - U_0 k_x)^2}} \tag{7.5}$$

Using (6.7) as before gives the pressure as

$$p(x, y, z) = \frac{1}{(2\pi)^2} \iint \frac{j\rho c(\omega - U_0 k_x)^2}{\omega\sqrt{c^2(k_x^2 + k_y^2) - (\omega - U_0 k_x)^2}} e^{j(k_x(x-x_0) + k_x(y-y_0)} e^{jk_z z} dk_y dk_x \tag{7.6}$$

The power radiated from the point source is given by equation (6.8). Noting that $|u_w| = 1$ for all k_x and k_y and that Re(Z_{rad}) is only non-zero inside an ellipse defined by

$$\left(\frac{k_x}{k}\right)^2+\left(\frac{k_y}{k}\right)^2=\left(1-\frac{k_x}{k}M\right)^2 \tag{7.7}$$

the radiated power is then given by

$$W_{rad}=\frac{1}{2(2\pi)^2}\int_{-1/(1+M)}^{1/(1+M)}\int_{-k_{y1}}^{k_{y1}}\frac{j\rho c(\omega-U_0k_x)^2}{\omega\sqrt{c^2(k_x^2+k_y^2)-(\omega-U_0k_x)^2}}dk_ydk_x \tag{7.8}$$

where $\frac{k_{y1}}{k}=\sqrt{\left(1-\frac{k_x}{k}M\right)^2-\left(\frac{k_x}{k}\right)^2}$.

As for the 2-D case, it is difficult to solve (7.6) and (7.8) analytically but a numerical integration using the DBLQUAD routine in MATLAB is straightforward.

Morfey's results [3] for the far-field pressure and power radiated by a 3-D point source are as follows

$$p(x,y,z;M)\approx\frac{p(x,y,z;0)}{(1+M\cos\phi)^3} \tag{7.9}$$

$$W(M)=\frac{1+\frac{1}{3}M^2}{(1-M^2)^3}W(0) \tag{7.8}$$

No comparison is made for the pressure field predicted using the two methods, but the perfect agreement between the analytical result and the numerical integration for the 3-D source is again shown in figure 7.3.

7.2 Sound radiation from 2-D sources under a boundary layer

7.2.1 Pressure field in the fluid

For a mean flow with a boundary layer of finite thickness it was shown in Chapter 4 that the waves propagating upstream are refracted away from the surface creating a noise shadow zone, whereas waves propagating downstream are channelled causing enhanced levels within the boundary layer. These effects are in addition to the influence of convective amplification, demonstrated in the previous section, which has the opposite effect of increasing levels in the upstream direction and reducing levels in the downstream direction.

The overall effect on the pressure field at the wall, z=0, is shown in figure 7.4 a)-c) which plots the pressure in the upstream and downstream directions for zero flow, and a 0.2 Mach number flow for two values of δ / λ.

From equation (7.3) the convective amplification for a 0.2 Mach number flow over a 2-D source is predicted to be +4.8 dB in the upstream direction and –3.9 dB in the downstream direction, a total difference of 8.7dB. Figure 7.4b) shows that for a thin boundary layer the numerical model predicts about 8 dB total difference in level between upstream and downstream at a distance of x/L=0.001, although an accurate determination of the difference is difficult because of the ripple in the data caused by the leakage effect discussed in Section 6.7. The level difference is not constant with distance because the damping in the model has a stronger effect upstream than downstream. The difference of approximately 0.7 dB between the numerical and theoretical upstream / downstream level difference is due to the effect of the thin boundary layer.

For a thicker boundary layer, figure 7.4c), the convective amplification around the source is much reduced, with the level upstream being only 1dB higher than the downstream level in the region of the source. At larger distances the level upstream falls rapidly due to the effect of refraction in the boundary layer, and the level downstream is enhanced by channelling. As a result, contrary to the thin boundary layer result in 7.4b) the level downstream is far higher than the level upstream. In figure 7.4c) it can be seen that the upstream and downstream values at the edge of the computational domain are equal, as expected for the Fourier method.

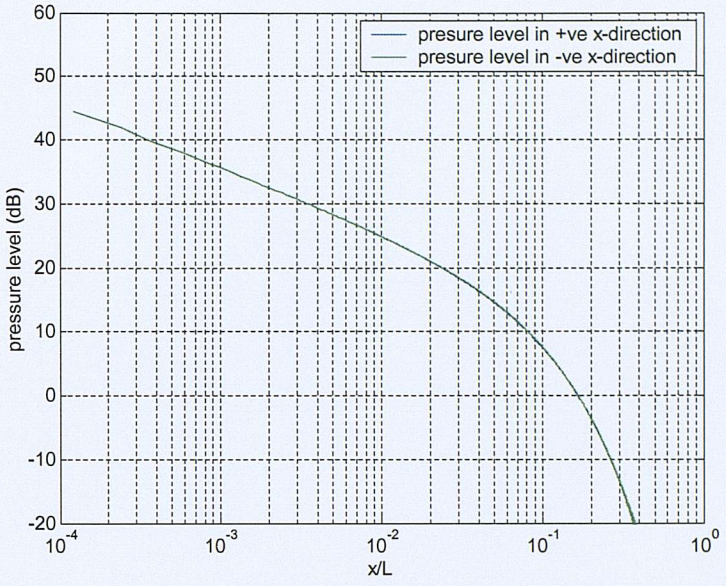

Figure 7.4a) Sound field with no flow showing identical upstream and downstream pressures

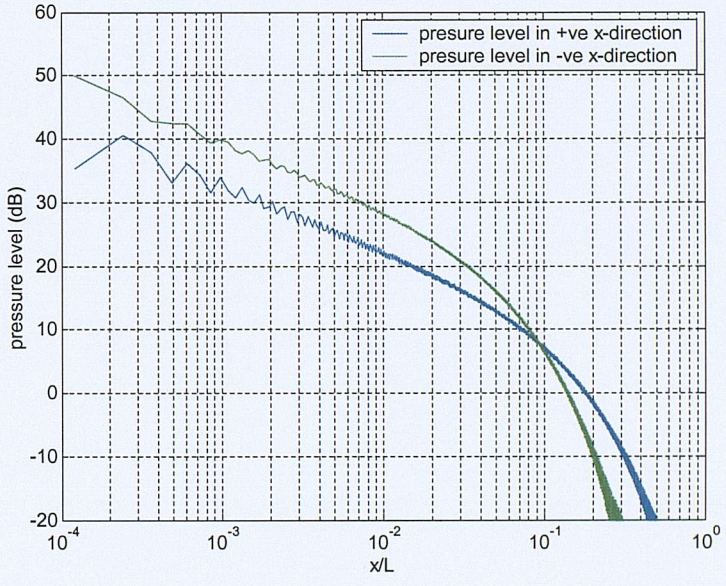

Figure 7.4b) Sound field in the presence of a 0.2 Mach number flow with a thin boundary layer.

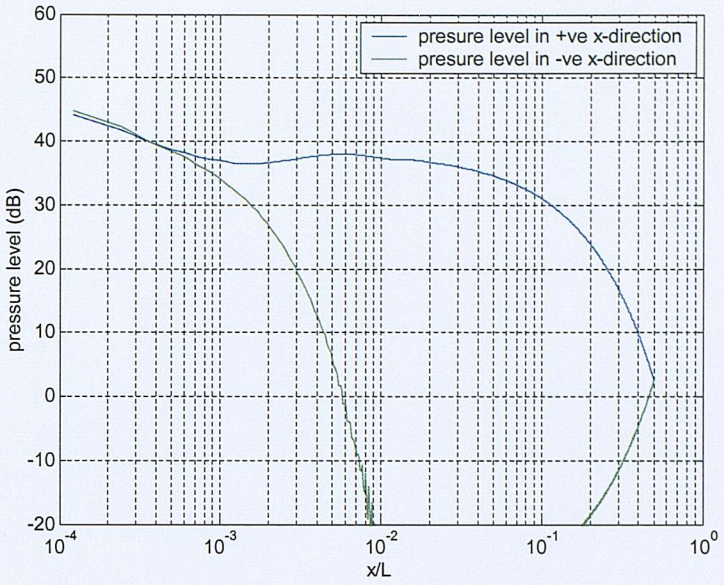

Figure 7.4c) Sound field in the presence of a 0.2 Mach number flow, boundary layer 1 wavelength thick

The effect of the flow and boundary layer thickness is most easily seen in contour plots in the x-z plane. Figures 7.5b)-f) which show results for a free stream flow Mach number of 0.3 with $\delta/\lambda = 0.001,\ 0.01,\ 0.1,\ 1,\ 10$. For comparison the zero flow result is included in figure 7.5a). The edge of the boundary layer is shown by a dashed line, although this is only visible for the thicker boundary layers. Figure 7.5g) shows a result for a 0.6 Mach number flow with $\delta/\lambda = 1$.

Feature of these plots are:

- Comparing the results for zero flow, figure 7.5a) with that for a thin boundary layer figure 7.5b), the effect of convective amplification is clearly dominant for this flow condition. The power output of the source is also increased by 1.2dB by the flow and this increases the contour size along the line z=0.
- as the boundary layer thickness grows up to a value of $\delta/\lambda = 1.0$ a deepening 'zone of silence' upstream is apparent, fig 7.5c)-e).
- Just downstream of the shadow zone is a region where pressure is enhanced relative to the zero flow sound field. For $\delta/\lambda = 1.0$ this peak in directivity occurs at an angle of 55° from the upstream flow direction (note that the aspect ratio of the plot is not square).

- Comparison of solutions at 0.3 and 0.6 Mach number, figs 7.5e)and 7.5g) shows, as expected, a steeping of the angle of the shadow zone and associated peak in directivity
- for $\delta/\lambda = 10$ the depth of the shadow zone is diminished relative to the levels seen at the wall with $\delta/\lambda = 1$.
- Downstream channelling of the sound by the boundary layer is apparent, for all boundary layer thicknesses.
- For $\delta/\lambda > 1.0$ there are local pressure maxima downstream. These are probably due to interference effects of boundary layer modes propagating at different phase velocities. Comparing 7.5e) and 7.5g) the proximity of the maxima to the source is reduced as Mach number increases.

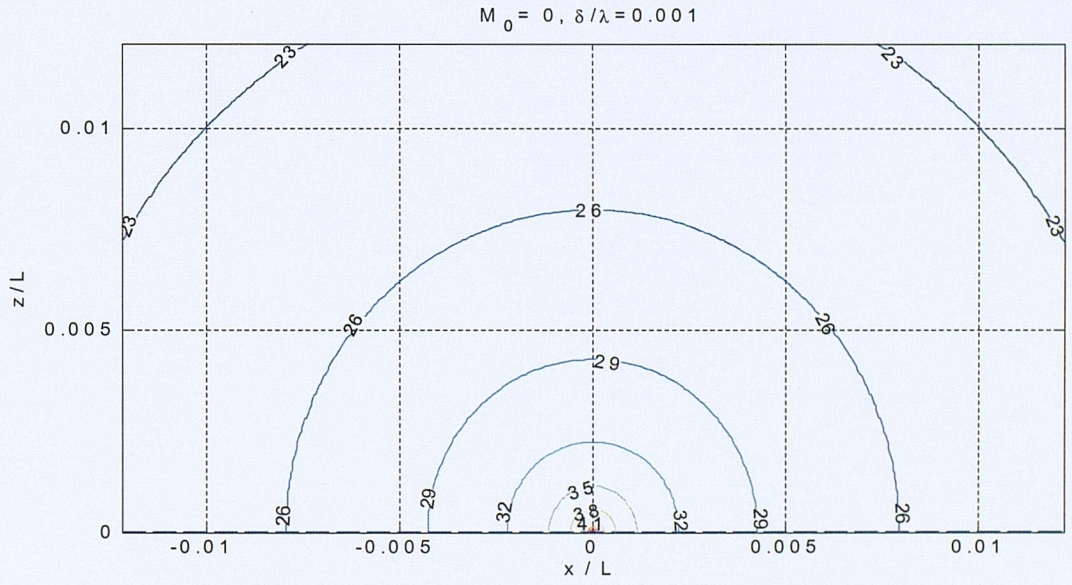

Figure 7.5a) Pressure contours around a line source. Zero flow solution

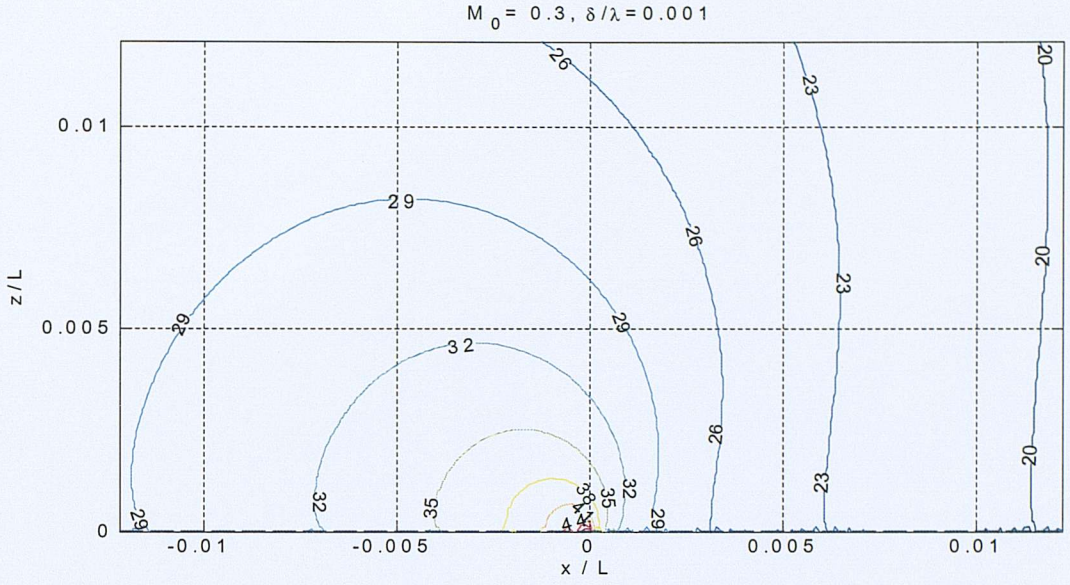

Figure 7.5b) Pressure contours around a line source. M=0.3 $\delta / \lambda = 0.001$

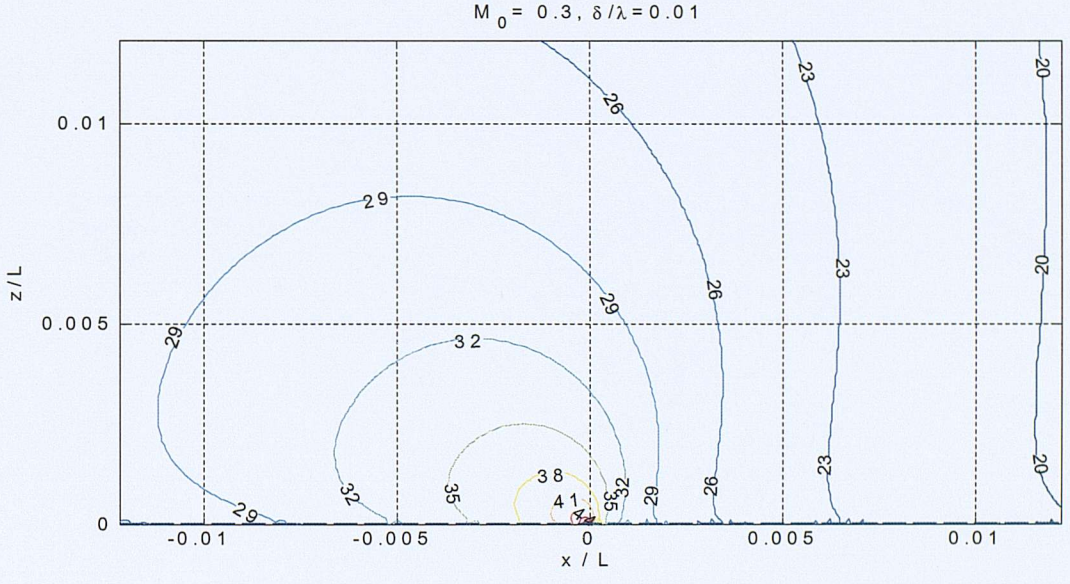

Figure 7.5c) M=0.3 $\delta / \lambda = 0.01$

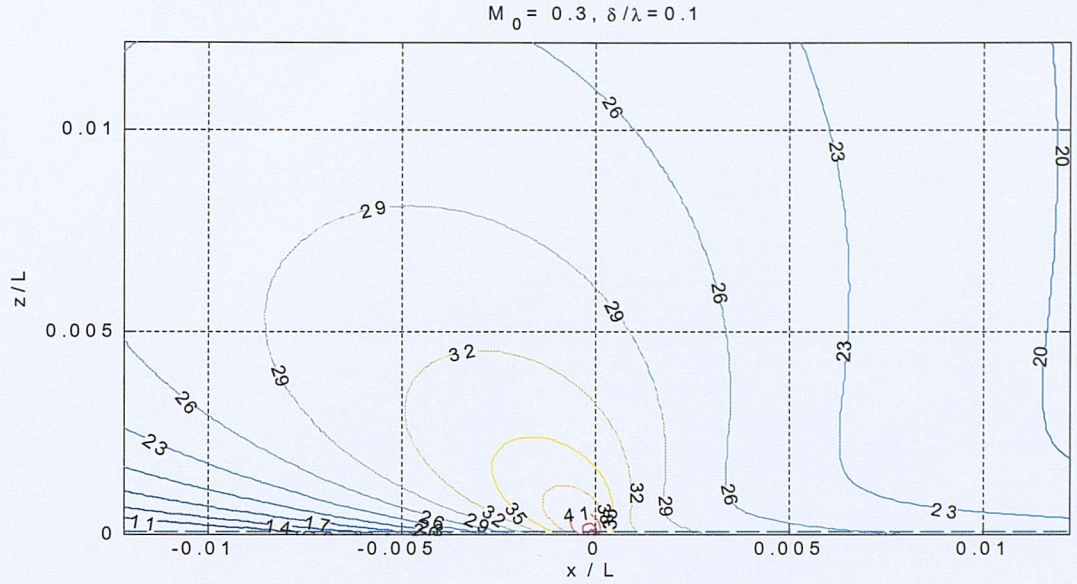

Figure 7.5d) M=0.3, $\delta / \lambda = 0.1$

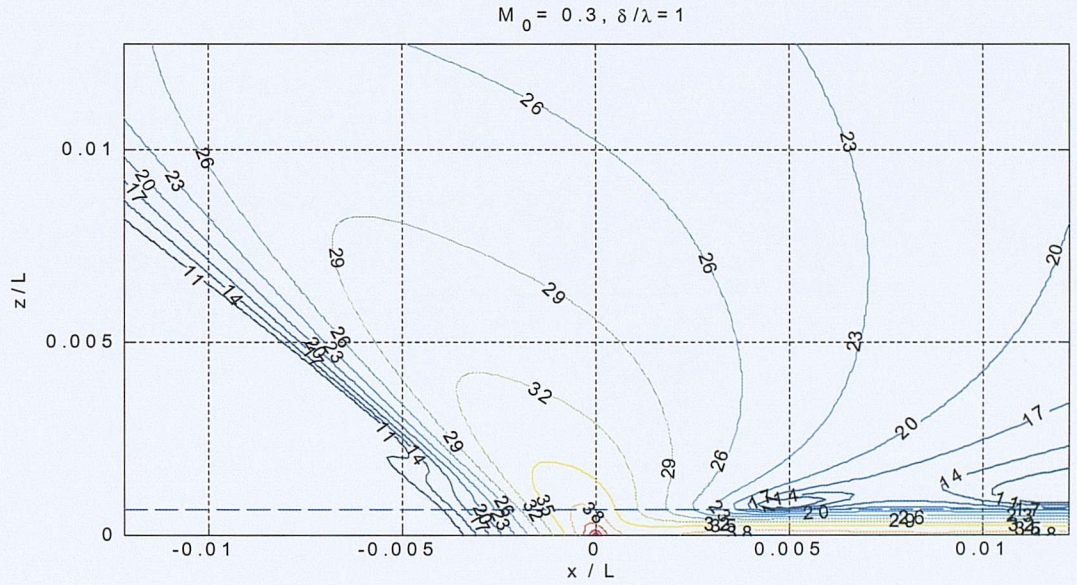

Figure 7.5e) M=0.3, $\delta / \lambda = 1.0$

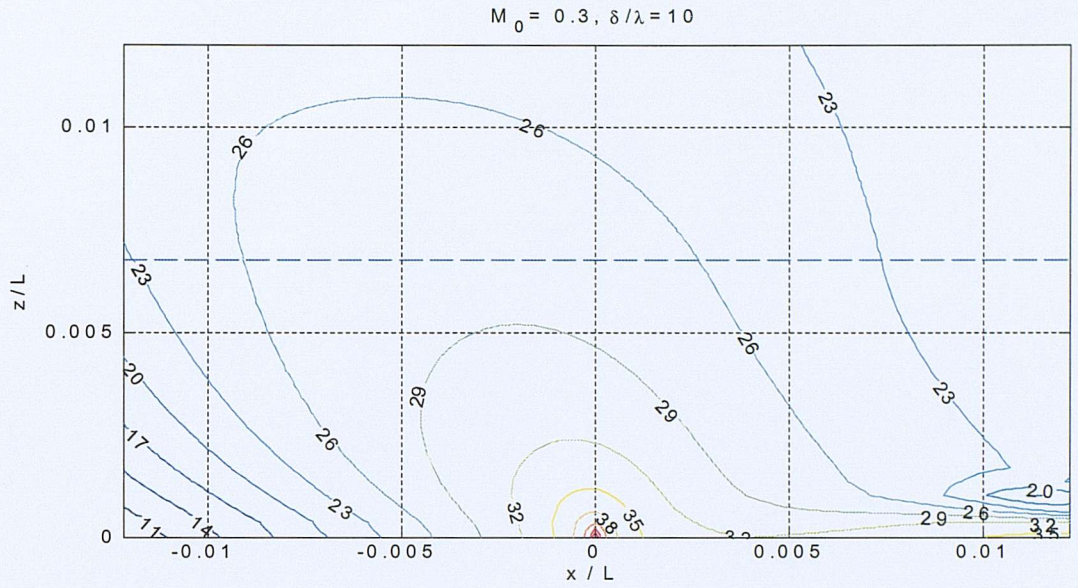

Figure 7.5f) M=0.3, $\delta / \lambda = 10$

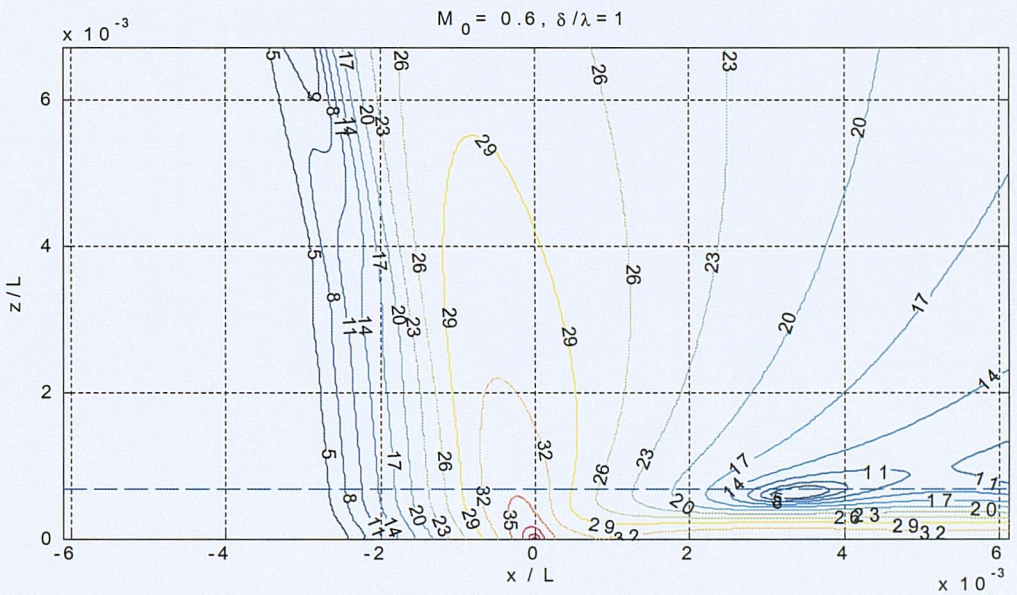

Figure 7.5g) Pressure contours around a line source. M=0.6, $\delta / \lambda = 1.0$

The previous plots have shown the pressure field due to a line source with *ka* = 0. For the *ka*=6.54 source described in the Chapter 6 the sound field generated with a 0.3 Mach number flow and a thin boundary layer is shown in figure 7.6. Comparing this result with figure 6.9 the following may be seen:

- the primary lobe of the sound field is now directed downstream rather than orthogonal to the surface

- there are two side lobes in the upstream direction, compared with one side lobe for the zero flow plot.
- The first side lobe, radiating at about 80° , is amplified relative to the zero flow plot and the downstream side lobe is reduced in amplitude. This is consistent with the expected effect of convective amplification.

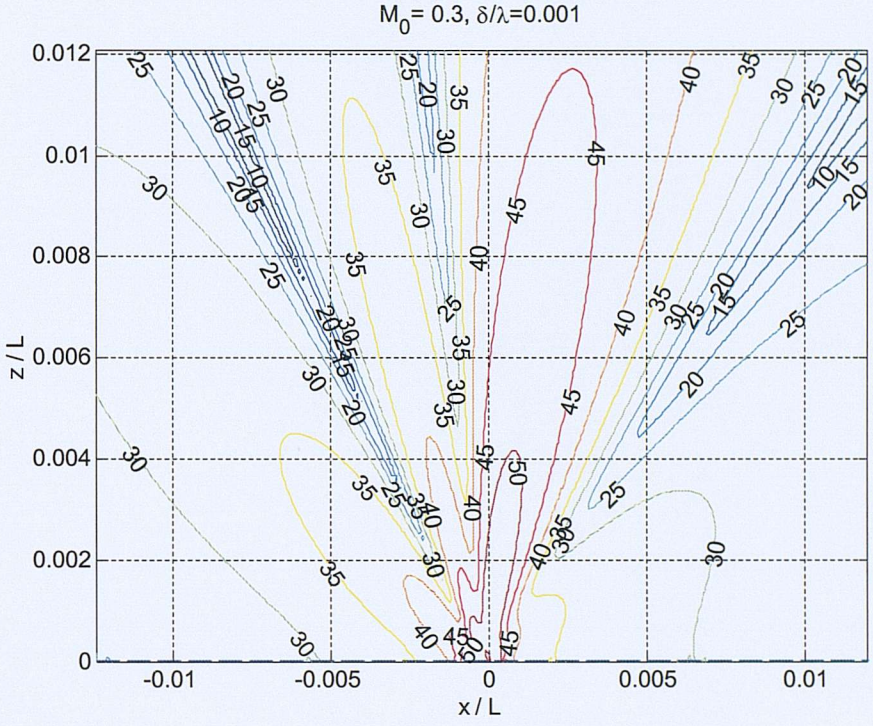

Figure 7.6 Sound field radiated by a 2-D source of ka=6.54 under a thin boundary layer with a 0.3 Mach number mean flow.

7.2.2 Sound power output from 2-D sources as a function of boundary layer thickness and Mach number.

In section 7.1 it was shown that the calculated sound power output from a line source under a uniform flow agreed with the expression given in equation (7.4). Here the effect of a boundary layer is now included.

Figure 7.7 shows the power output as a function of Mach number for a point source for a range of values of δ/λ. As the boundary layer thickness grows the radiated power drops rapidly to the zero flow power output. By visual interpolation between the lines plotted it can be seen that the effect of the flow in increasing power output is approximately halved when $\delta/\lambda \approx 0.03$.

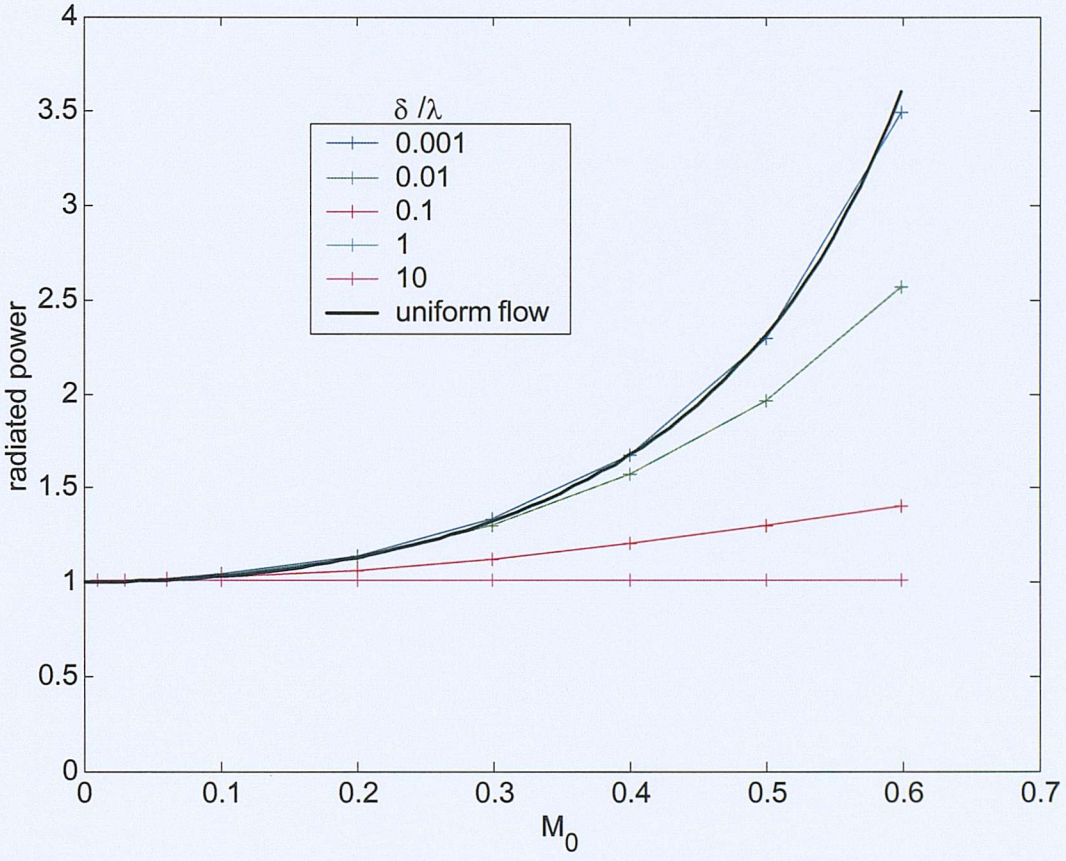

Figure 7.7 Power radiated from a 2-D point source as a function of Mach number and boundary layer thickness. NB $\delta/\lambda = 1$ is identical to $\delta/\lambda = 10$

The mathematical model may be used to predict the effect of the flow on non-compact sources. The result for the *ka*=6.54 source described in the previous section was produced, and it was found that the power output is virtually unaffected by the flow. This is because at this high *ka* most power is radiated across the flow, whereas the major effect of the flow on increasing power output occurs in the upstream direction. Carrying out a more detailed analysis of the effect of *ka* on flow–source interaction is suggested as an item of further work in Section 10.2.

7.2 Pressure field from 3-D sources under a boundary layer

In Section 6.3, figures 6.11 and 6.12, it was shown that in the absence of flow the model correctly predicts the inverse square law and the circular (hemispherical) noise contours around a 3 D source. When a transverse mean flow is applied, it may be expected that wave number components for which k_y=0, i.e. that propagate directly upstream or downstream, would see similar refraction and amplification effects to those demonstrated for 2 D propagation. However, for waves with non-zero k_y values which propagate across the flow, the effect of the boundary layer will be modified.

To illustrate the effects, figures 7.8 to 7.11 show the sound field at the wall, z=0, due to a 3D point source radiating into a mean flow of free-stream Mach number 0.3. Results are shown for thin and thick boundary layers, with $\delta/\lambda = 0.001$ and $\delta/\lambda = 1$ respectively. For each case a contour plot in the x-y plane of the sound field is produced, and also a cut through this plot at y=0.

With a thin boundary layer, figures 7.8 and 7.9, it can be seen that the effect of convective amplification dominates so that the level upstream is the level is increased relative to the zero flow case, and downstream the level is decreased.

For the thick boundary layer, $\delta/\lambda = 1$, figures 7.10 and 7.11, the refractive effect of the boundary layer is dominant and the level downstream at the wall is higher than the level upstream.

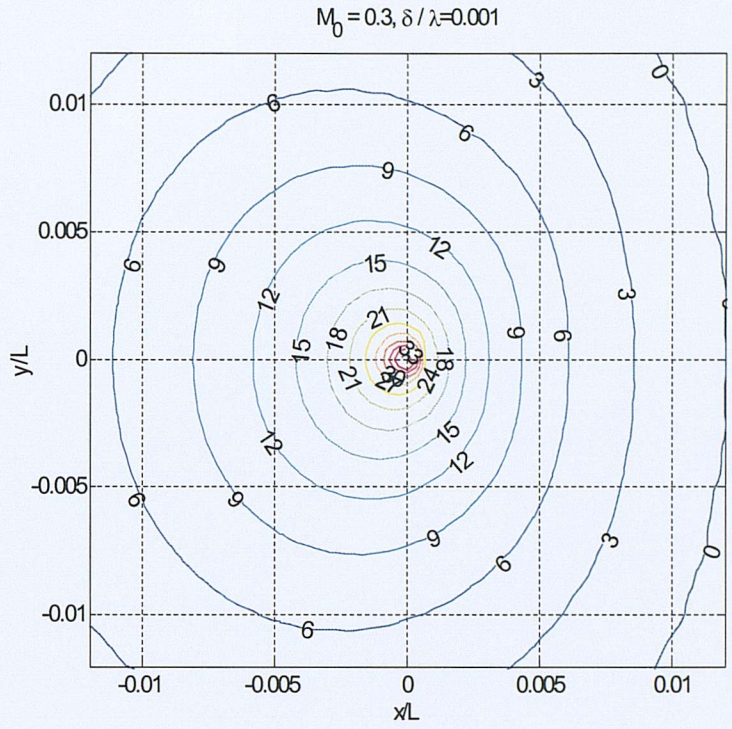

Figure 7.8 Contours of sound pressure level at z=0 around the source centred at x=0, y=0 with a Mach 0.3 flow in the +x-direction and boundary layer thickness $\delta / \lambda = 0.001$.

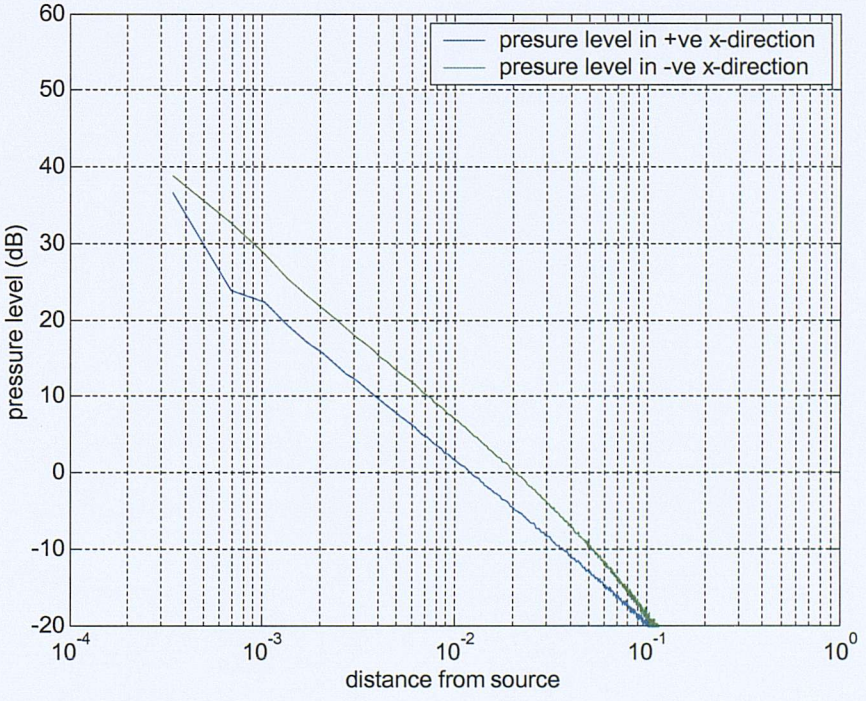

Figure 7.9 Sound pressure level cut along the line y=0, z=0 through the data of figure 7.9

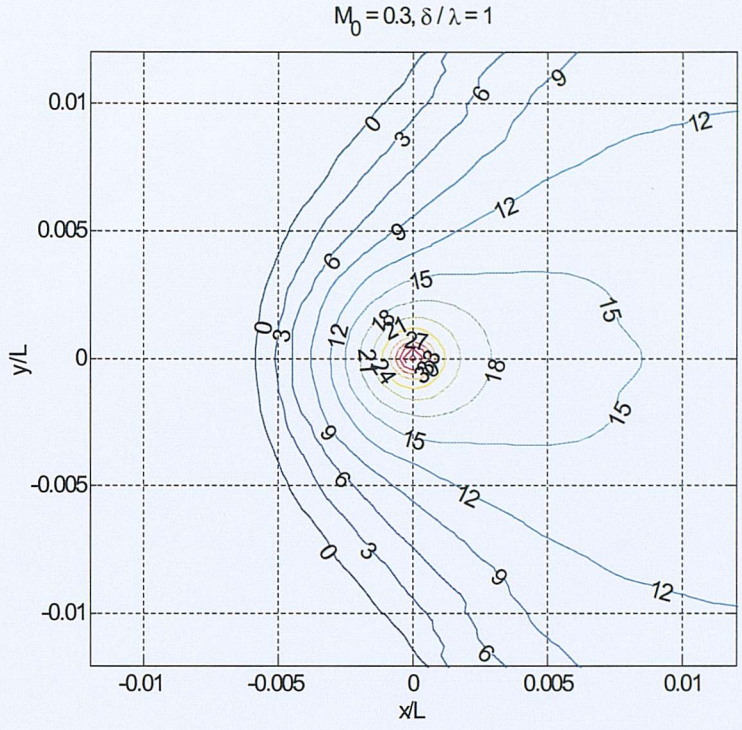

Figure 7.10 Contours of sound pressure level at z=0 around the source centred at x=0, y=0 with a Mach 0.3 flow in the +x-direction and boundary layer thickness $\delta / \lambda = 1.0$.

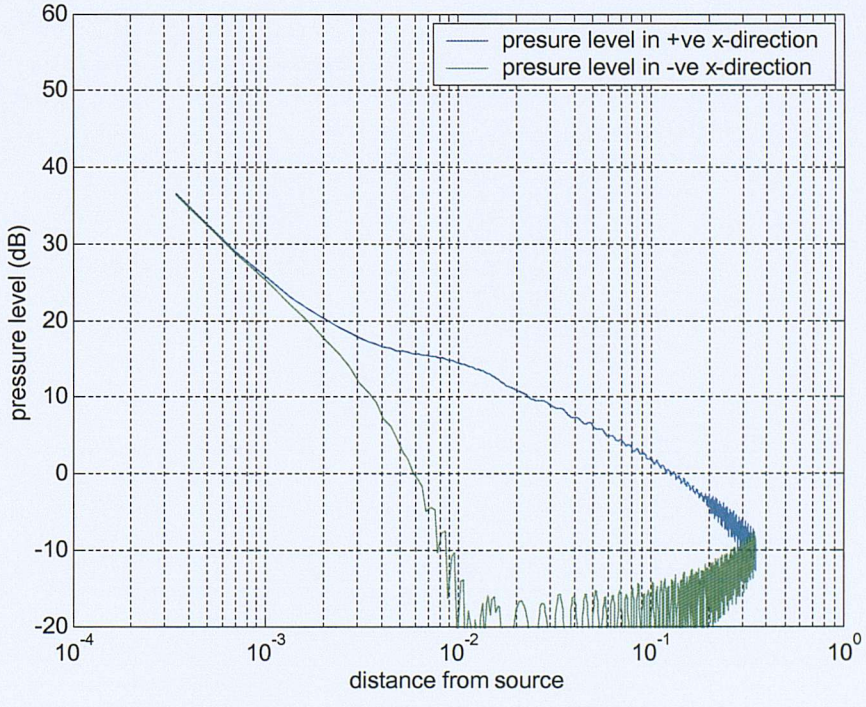

Figure 7.11 Sound pressure level cut along the line y=0, z=0 through the data of figure 7.9

7.4 Conclusions

The sound field radiated by compact 2D and 3D sources has been shown to be a strong function of Mach number and boundary layer thickness. For thin boundary layers the change to the sound field relative to the zero flow case is dominated by the effect of convective amplification that, as predicted by uniform flow models, increases the pressure upstream of the source and decreases the pressure downstream. The power radiated by the source is also increased by the flow.

As the boundary layer thickness grows a noise shadow forms upstream of the source and channelling of the sound by the boundary layer increases the level at the wall downstream. The power radiated is also reduced; the power output of a source under a boundary layer one wavelength thick is the same as the output of the source with no grazing flow.

The model is also able to predict the radiation from non-compact sources, with a combination of convective amplification and refraction again apparent.

Chapter 8

8. APPLICATION TO FLOW MEASURMENT

This chapter describes the application of the mathematical model to the problem of an ultrasonic flow measuring device. Chapter 9 then outlines some details of a prototype measurement system, describes a wind tunnel experiment to test the instrument and compares preliminary results from the experiments with predictions from the model.

8.1 The 2-transducer measurement principle for unidirectional flow

Ultrasonic flow measurement is a well established technique for fluid flowing in pipes with many papers published on the topic, a recent example being [38]. It is also used in meteorological anemometers to measure wind speed [39]. No literature has been found on the use of ultrasonic measurements in boundary layers.

The technique used in ducts depends upon a 1D model of the convected phase velocity of sound propagation in a moving medium: For a plane wave mode propagating in a rigid walled duct carrying a uniform flow, the phase velocity is $c_0(1+M_0)$ in the downstream direction and $c_0(1-M_0)$ in the upstream direction. Here c_0 is the speed of sound in stationary fluid and M_0 is the Mach number of the flow relative to this sound speed.

The measurement of phase velocity generally uses a system in which a transducer, the source, emits a pulse of sound, and the time taken for this to arrive at a second transducer, the receiver, is measured. The system uses phase information contained in the pulse to ensure that the phase velocity is measured rather than group velocity. The detail of how this is done is beyond the scope of this thesis, but the implication for a continuous wave model of the system is that the model must predict the total phase change between source and receiver.

Instruments measuring flow in a pipe commonly take a measurement of both upstream and downstream flight times, t_u and t_d, over some distance L, so that the two transducers act alternately as a source and then as a receiver. The Mach number of the flow and the speed of sound of the fluid may then be found by solving the following simultaneous equations:

$$\frac{L}{t_u} = c_0 (1 - M_0), \tag{8.1a}$$

$$\frac{L}{t_d} = c_0 (1 + M_0). \tag{8.1b}$$

Solving these equations for the flow Mach number gives

$$M_0 = \frac{L(t_u - t_d)}{2 t_d t_u c_0} \tag{8.2}$$

Equation (8.2) shows that the measurement of flow Mach number is dependent on the difference between the upstream and downstream times of flight, and one advantage of the dual measurement is that time delays inside the transducer or the electronics of the instrument cancel because of reciprocity. This makes the measurement technique far more robust.

8.2 Calculation of phase velocity from the mathematical model

This section describes how the model described in previous chapters may be used to determine the phase velocity for sound transmission between two transducers, flush mounted under a boundary layer. This method is then used in the following sections to show the effect of free-stream Mach number and boundary layer thickness on the phase velocity that would be inferred in an experiment.

In the measurement system described in the next chapter both source and receiver were located under a boundary layer and it was found that, because of the upstream noise shadow effects described in chapter 7, only a downstream measurement of time of flight could be made. It was thus necessary to calculate the speed of sound from the air temperature in the wind tunnel, so that equation (8.1b) could be used to determine a propagation Mach number ($1+M_0$), and hence a 'measured' flow velocity $U = c_0 M_0$.

In terms of the pressure field downstream of the source at the wall, $p(x,0,0)$, predicted by the continuous wave model, the propagation time from source to receiver at frequency f is given by

$$t_d = \frac{1}{2\pi f} \int_L \frac{d}{dx} \left(\arg(p(x,0,0)) \right) dx \tag{8.2}$$

For a discretized numerical model comprising a set of points x_i, with the source and receiver defined to be at x_0 and x_n respectively, the total phase change between source and receiver is approximated by the cumulative sum over the phase change between adjacent points. Thus the propagation time from the source point to the receiver point is given by

$$t_d(x_n) = \frac{1}{2\pi f} \sum_{i=0}^{n-1} (\arg(p(x_{i+1})) - \arg(p(x_i))) = \frac{1}{2\pi f} \sum_{i=0}^{n-1} \arg\left(\frac{p(x_{i+1})}{p(x_i)} \right) \tag{8.3}$$

The average propagation Mach number for this receiver location, $M_d(x_n)$, is then calculated from

$$M_d(x_n) = \frac{(x_n - x_0)}{t_d(x_n)\, c_0} \tag{8.4}$$

Figures 8.1 to 8.3 illustrate the process for a zero flow case. The plots also show the phase variation in the upstream direction, which is calculated using similar algorithms.

Figure 8.1 shows the local phase at a series of points in a small region around a point source at x/L =0. It is important to have many field points per wavelength so that there is no loss of phase information due to aliasing of the discretized spatial field. The cumulative sum of the phase change between points, the summation in (8.3), is plotted as a function of distance from the source in figure 8.2.

The average propagation Mach number of sound as a function of distance downstream of the source is shown in Figure 8.3. Close to the source there is a near field effect which perturbs the 'measurement', but the propagation Mach number quickly converges to $M_d = 1$, as expected for zero grazing flow.

When a mean flow of Mach number $M_0 = 0.3$ is applied, with a thin boundary layer $\delta/\lambda = 0.001$, it can be seen in figures 8.4 and 8.5 that the rate of change of phase with distance is reduced in the downstream direction and increased in the upstream direction compared with the zero flow results in figures 8.1 and 8.2.

Figure 8.5 shows that the rate of change of phase with distance in the upstream direction is constant out to $x/L = -0.25$, but that the graph then changes slope. This is due to the growing influence of image sources upstream as x/L becomes more negative, with nergy from the primary source being refracted away from the surface. This illustrates a difficulty with upstream 'measurement' in the mathematical model which is analogous to the difficulty of upstream measurement in an experiment.

For this case, M_0=0.3 and $\delta/\lambda = 0.001$, the downstream propagation Mach number M_d relative to the wall, figure 8.6, converges rapidly to (1+M_0) downstream and (1-M_0) upstream. In the upstream direction the 'measurement' gives a correct answer to approximately $x/L = -0.25$, but then diverges for the reasons noted above.

When the boundary layer is thickened to $\delta/\lambda = 1.0$, the results are as shown in figures 8.7 to 8.9. The cumulative phase graph shows an increased slope, indicative of the fact that the propagation Mach number shown in figure 8.9 has dropped from 1.3 to 1.16. Upstream, the thicker boundary layer refracts sound away from the surface more strongly than for the $\delta/\lambda = 0.001$ case of figure 8.6 and so that the region in which the true upstream propagation Mach number can be seen is considerably reduced in size.

In the following sections consider the effect of Mach number and boundary layer thickness on downstream propagation speed for a fixed transducer spacing will be considered. Figures 8.3, 8.6 and 8.9 show a cross at x/L=0.07, which marks a point where all 'measurements' from the model will be made.

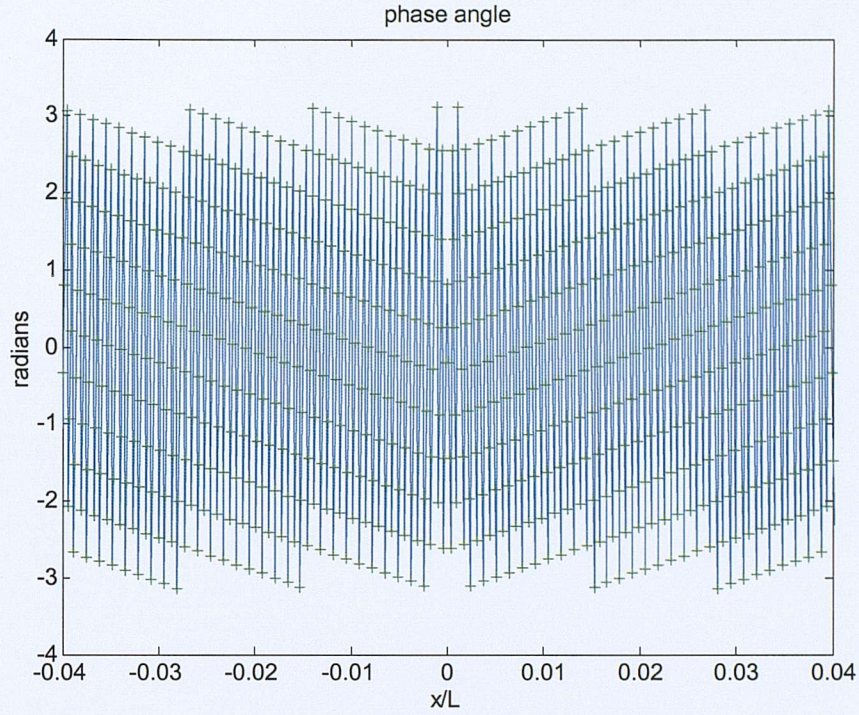

Figure 8.1 Phase at field points, marked +, around the locality of a point source; M_0=0.

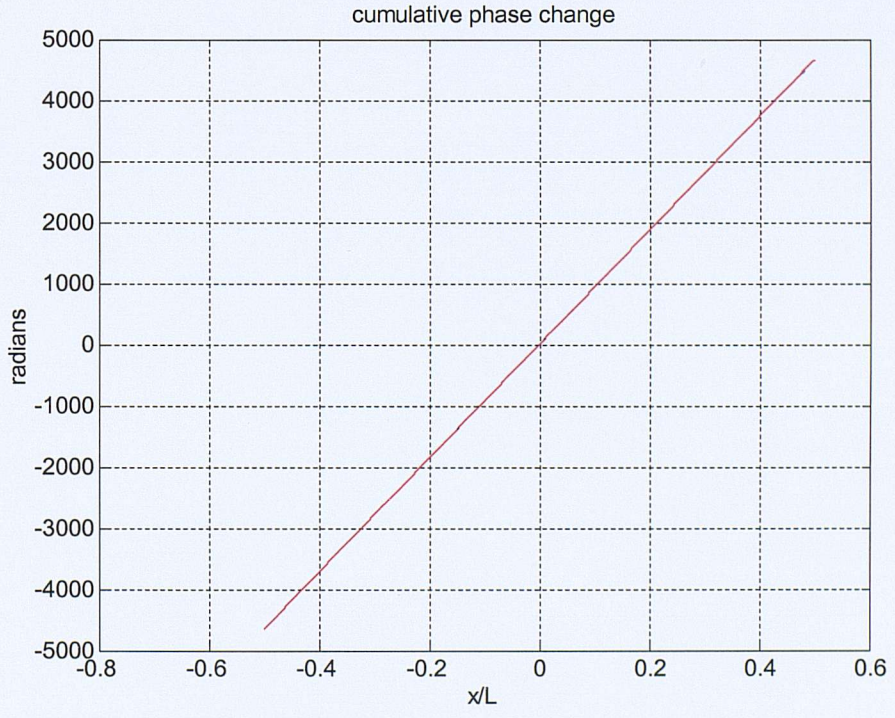

Figure 8.2 Cumulative phase variation integrated upstream and downstream from $x=0$ *to* $x = \pm L/2$ *;* M_0=0.

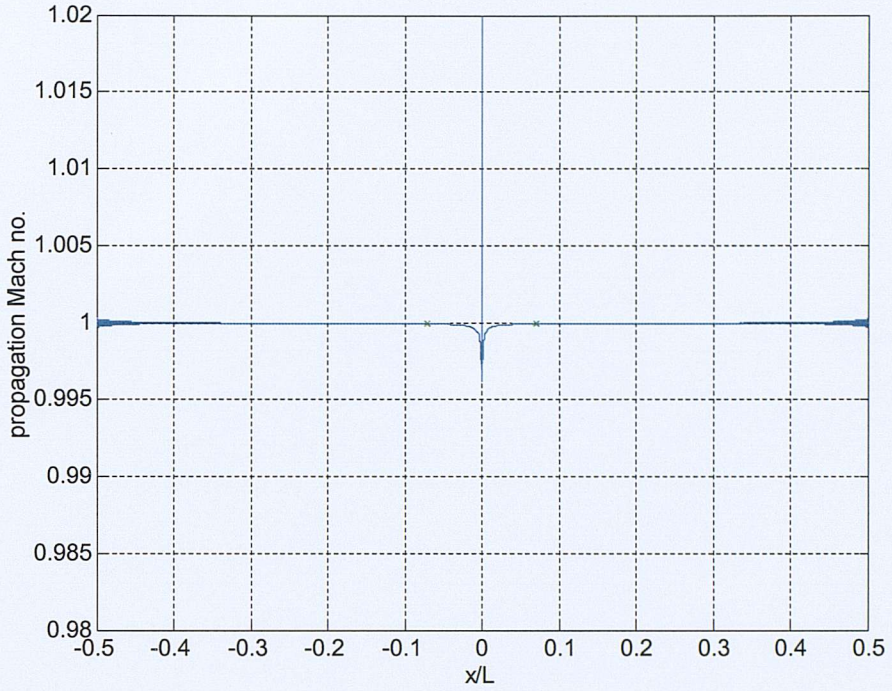

Figure 8.3 Calculated propagation Mach number as a function of distance from the source; M_0=0.

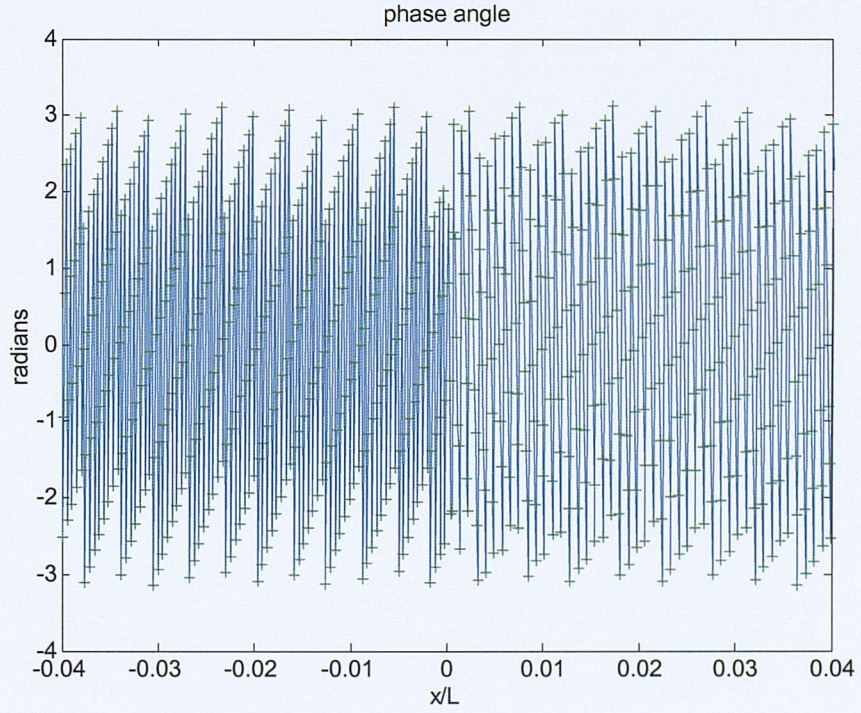

Figure 8.4 Phase at field point around the locality of a point source; $M_0 = 0.3$, $\delta / \lambda = 0.001$

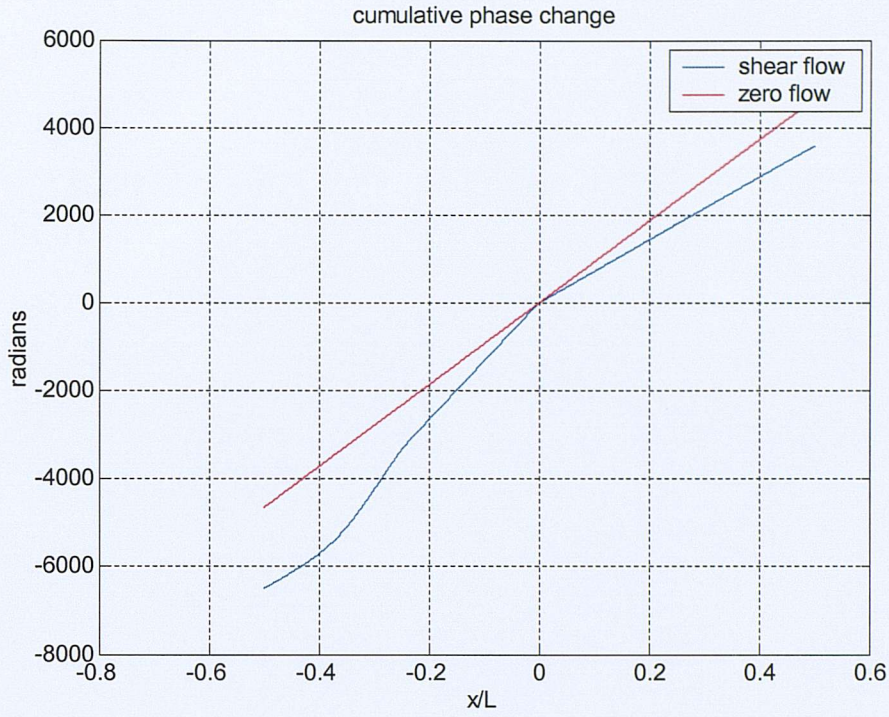

Figure 8.5 Cumulative phase variation integrated upstream and downstream from x=0 to $x = \pm L/2$; $M_0 = 0.3$, $\delta/\lambda = 0.001$

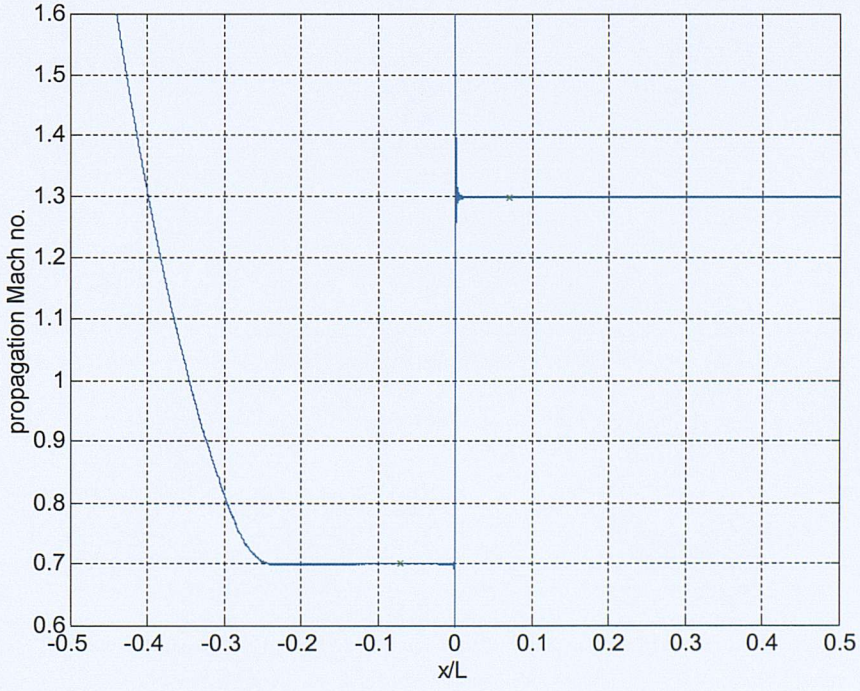

Figure 8.6 Calculated propagation Mach number versus distance; $M_0 = 0.3$, $\delta/\lambda = 0.001$

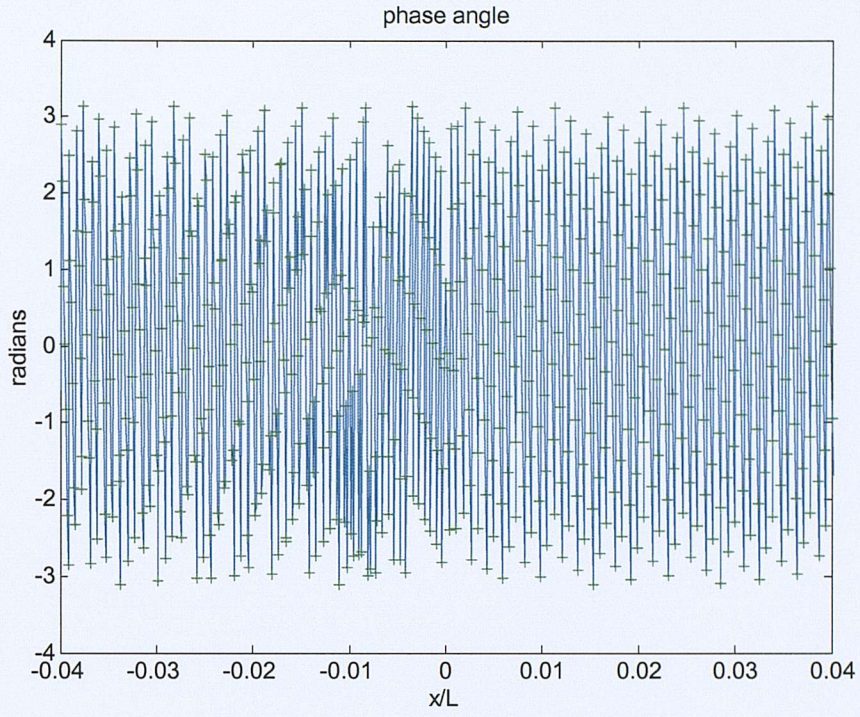

Figure 8.7 Phase at field point around the locality of a point source; $M_0 = 0.3$, $\delta / \lambda = 1.0$

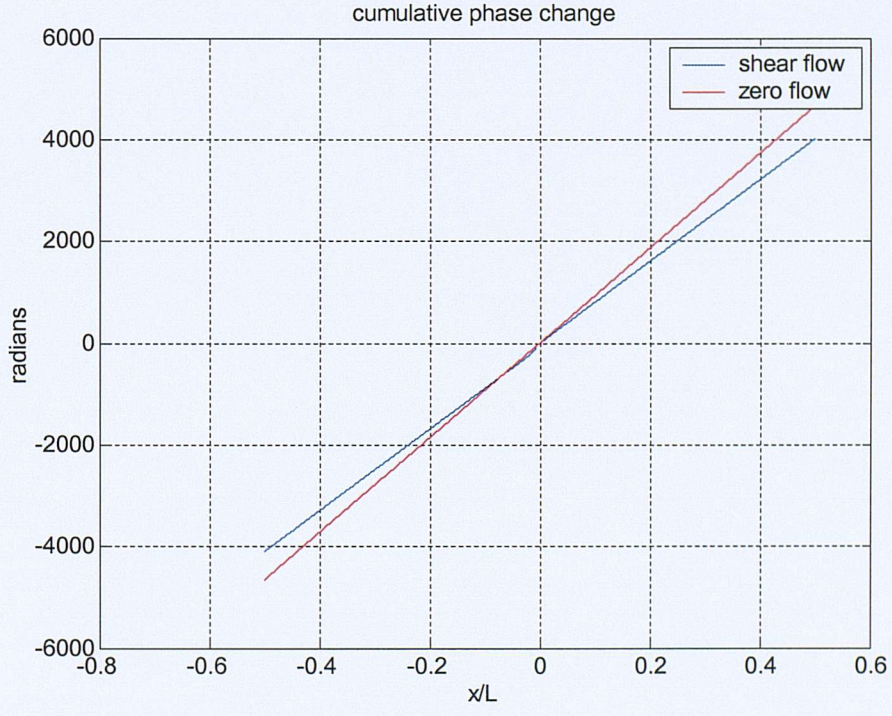

Figure 8.8 Cumulative phase variation integrated upstream and downstream from x=0 to $x = \pm L/2$; $M_0 = 0.3$, $\delta / \lambda = 1.0$

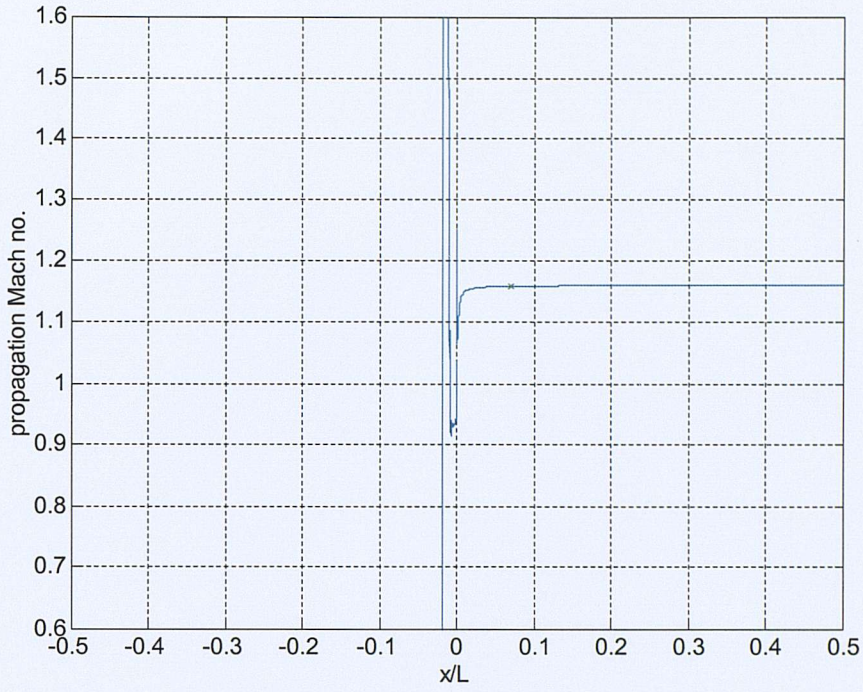

Figure 8.9 Calculated propagation Mach number versus distance; $M_0 = 0.3$, $\delta / \lambda = 1.0$

8.3 Phase velocity downstream of a 3D source

The previous section showed that a 2D model gives the expected change in downstream propagation Mach number with a thin boundary layer. This section now considers 3D geometry to show firstly that the downstream result is the same as for 2D propagation, and then to demonstrate the effect of propagation transverse to the flow direction.

The first case chosen to demonstrate the problem is for a Mach 0.3 flow with $\delta / \lambda = 0.001$. The sound pressure level distribution around the source for this case was shown in figures 7.9 and 7.10, and the flow measurement results may be compared with figures 8.5 and 8.6. Some care is needed in comparisons with the 2D model as a 8192 point transform was used to generate these results, whereas in the 3D problem a 2048x2048 double Fourier transform has been used. The discretization rate was the same in each case, but the domain size L was reduced by a factor of four in the 3D problem. This means that plots versus x/L are scaled differently by this factor.

Figure 8.10 shows a the cumulative phase plot upstream and downstream of the 3D source, and comparison with figure 8.5 shows that the rate of change of phase with distance is identical in the two problems, i.e. there is the same factor of four scaling in both coordinates.

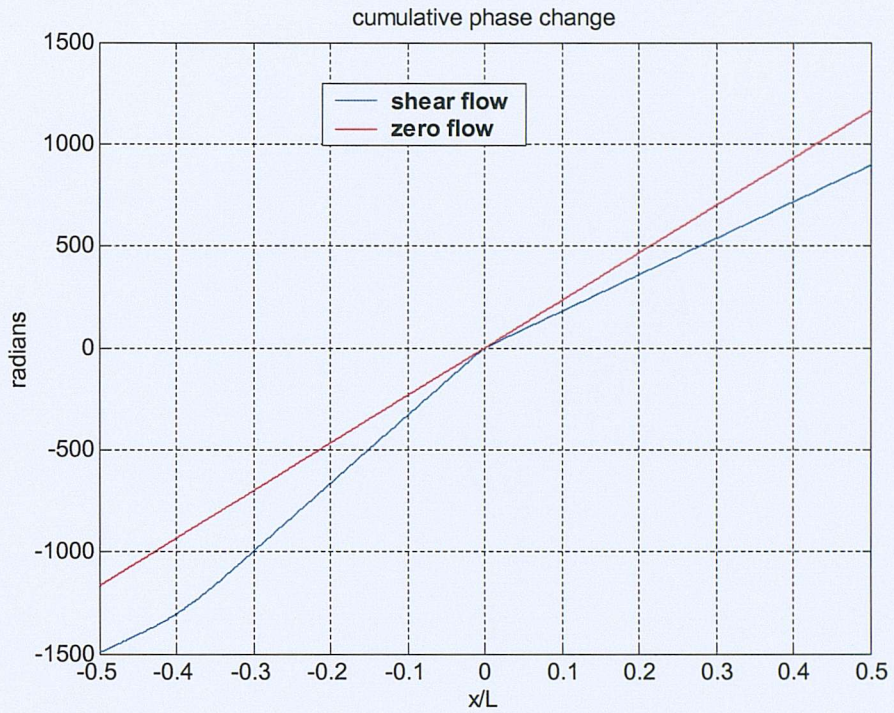

Figure 8.10 Cumulative phase variation integrated upstream and downstream from a 3D source at x=0 to $x = \pm L/2$; $M_0 = 0.3$, $\delta/\lambda = 0.001$

The propagation Mach number directly upstream and downstream of the 3D source is shown in figure 8.11, and comparison with figure 8.6 shows that 'measurement' converges to the same result as the 2D case, ($1+M_0$) downstream and ($1-M_0$) upstream. The main difference is that the rate of convergence is affected by the factor of four change in length scale. This result may have been anticipated since the waves propagating parallel to $y = 0$ in the 3D model by definition have transverse wave number $k_y = 0$, as is the case in the 2D model.

Figure 8.11 also shows the result of measuring propagation Mach number along the line x=0 which lies transverse to the flow. It might be thought initially that a value of M_d =1.0 should be observed along this trajectory, but consideration of figure 8.12 shows why this is not the case.

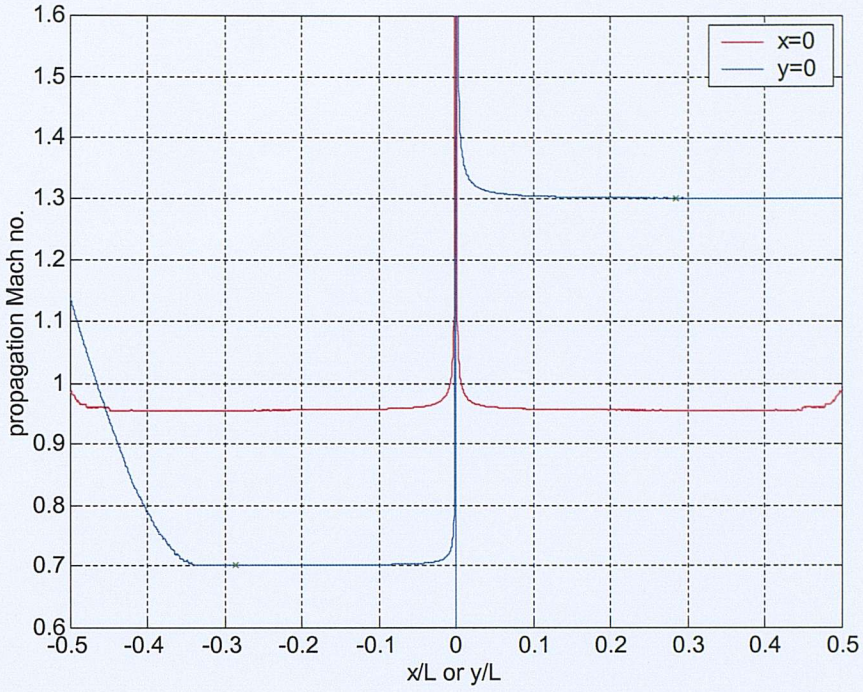

Figure 8.11 Calculated propagation Mach number versus distance from a 3D source located at (x=0, y=0) showing upstream and downstream propagation, y=0, and lateral propagation, x=0 ; $M_0 = 0.3$, $\delta / \lambda = 0.001$

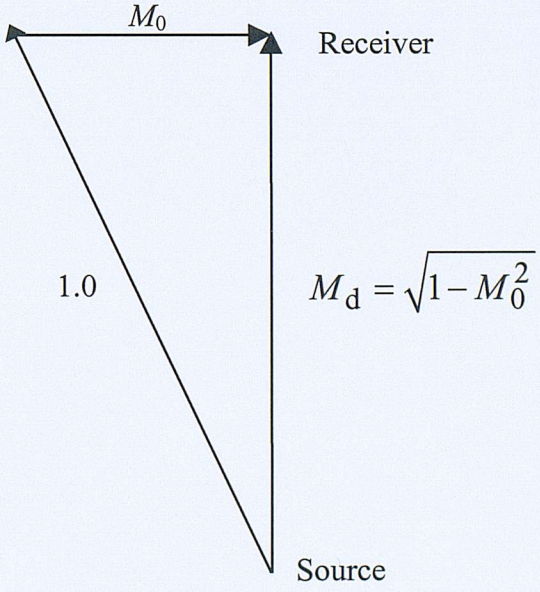

Figure 8.12 Mach number vector diagram showing the calculation of propagation Mach number from source to receiver when the receiver lies on the line x=0.

Sound arriving at the receiver may be considered to have propagated at Mach 1 along the path marked 1.0, and to be simultaneously convected downstream at Mach number M_0. Pythagoras then gives $M_d = \sqrt{1-M_0^2}$, which when M_0=0.3 means that M_d = 0.954. The limiting transverse propagation Mach number in figure 8.11 agrees well with this value.

It is clear from this discussion that in principle a measurement of propagation Mach numbers using a source and two receiver locations separated by an angle φ may be used to calculate both the free stream flow Mach number and the angle of the flow relative to the orientation of the three transducers. The situation is shown in the following diagram. Measurements of M_{d1} and M_{d2} would allow M_0 and φ_1 or φ_2 to be calculated using basic trigonometry.

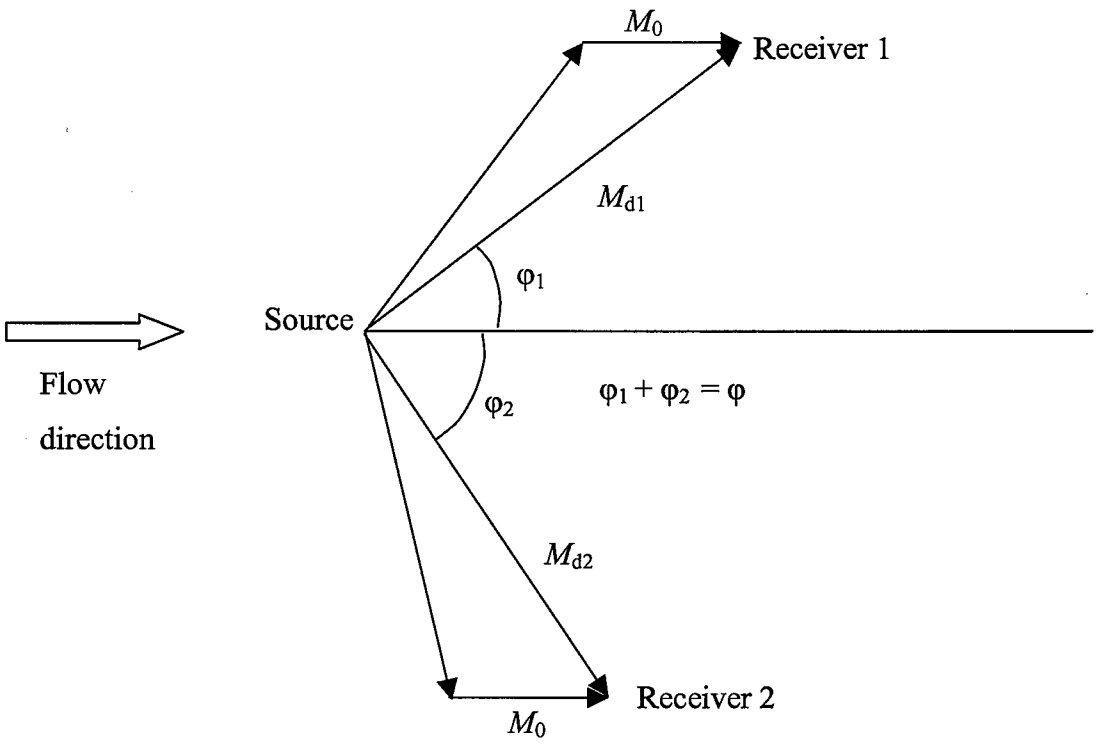

Figure 8.12 Mach number vector diagram for the calculation of flow direction from a measurement using a source and two receivers.

8.4 Parameter study using the 2-D model with flow

In this section the 2D acoustic model is used to study the variation of 'measured' sound propagation speed with flow Mach number, boundary layer thickness and boundary layer profile. The two boundary layer profiles considered are the cubic profile, which has been used to generate the bulk of results in this thesis and is fairly representative of a laminar boundary layer, and the $1/7^{th}$ power law profile which is representative of a turbulent boundary layer. The profile shapes are defined in equation (4.1) and plotted in figure 4.1.

Figure 8.13 shows the dependence of the excess propagation Mach number ($M_d - 1$) on the free stream Mach number M_0, and the non-dimensional boundary layer thickness. A cubic profile has been used. For a thin boundary layer with $\delta/\lambda < 0.01$ it can be seen that the predictions fall on the line expected for uniform flow, i.e. that ($M_d - 1$) = M_0. As the boundary layer grows in thickness beyond $\delta/\lambda = 0.1$ there is a strong variation of excess propagation Mach with boundary layer thickness.

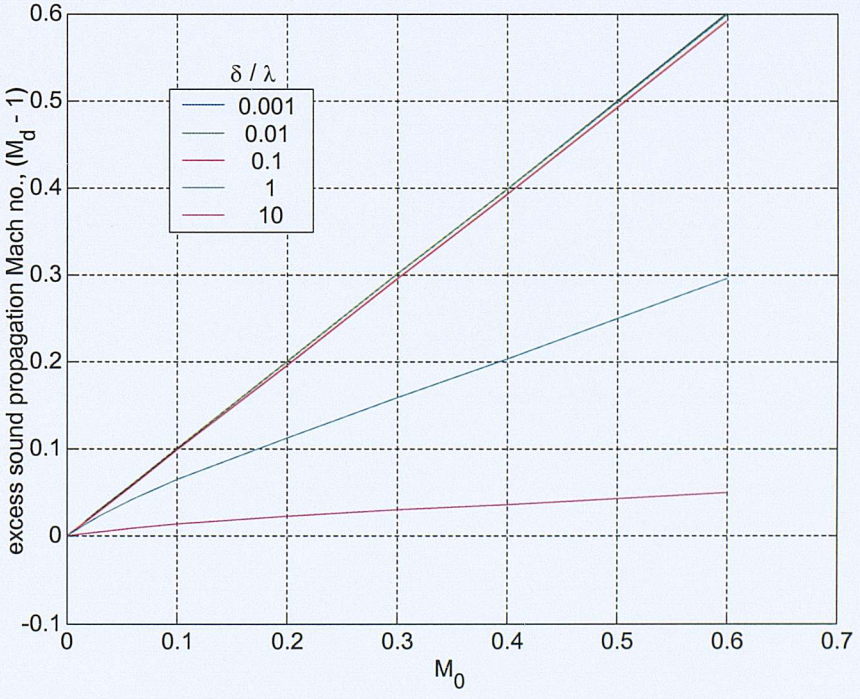

Figure 8.13 Variation of excess propagation Mach number, ($M_d - 1$), with free stream Mach number and boundary layer thickness for a cubic power law boundary layer profile.

A more detailed plot of the variation of $(M_d - 1)$ with boundary layer thickness is given in figure 8.14 for a flow with $M_0 = 0.3$. This plot shows results for both the cubic and $1/7^{th}$ power law profiles. Because the mean flow velocity in a $1/7^{th}$ power law profiles increases rapidly away from the wall, figure 4.1, the effect of this type of a thick boundary layer in reducing the excess propagation Mach number is significantly less than for the cubic profile.

The boundary layer parameter used to generate figures 8.14 and 8.15 is the layer thickness, defined as the distance from the wall to the edge of the region of uniform flow as shown in figure 2.1. It can be seen from enlarged profiles plotted in figure 4.1 that δ_{99}, the z value for which the flow velocity is 99% or the free stream value, is close to δ, and virtually the same for both profiles. A plot of excess propagation Mach number versus δ_{99} / λ would therefore look similar to figure 8.14.

Other measures of boundary layer thickness are the displacement thickness, the momentum thickness and the kinetic energy thickness. These are defined respectively [37] as the thickness of stationary fluid layer which accounts for the defect in fluid displacement, momentum or kinetic energy relative to the quantities for a uniform flow. It easy to show by an integration based on the profile equations (4.1) that the other measures have the values shown in the following table.

	Displacement thickness δ_{disp} / δ	momentum thickness δ_{mom} / δ	Kinetic energy thickness δ_{ke} / δ
1/7 power law	0.1250	0.0972	0.1750
Cubic power law	0.3750	0.1393	0.2156
Ratio	1 : 3	1 : 1.43	1 : 1.23

Table 8.1 Normalised measures of boundary layer thickness for the two profiles

From this table it can be seen that the ratio of displacement thicknesses between the two boundary layer profiles is 1:3, whereas the ratio for other measures is lower. By inspection of the data in figure 8.14 it is apparent that the best collapse of data will be achieved by re-

plotting the data as a function of displacement thickness. Figure 8.15 shows the data re-plotted in this way, and demonstrates a reasonable collapses for boundary layers with a displacement thickness of $\delta_{\text{disp}} / \lambda < 0.1$.

An implication of this result is that, by measuring the variation of phase velocity with frequency, it should be possible to determine both the free-stream velocity and the boundary layer displacement thickness. To do this the convected phase velocity is required at a minimum of two frequencies, ideally having wavelengths satisfying $\delta_{\text{disp}} / \lambda < 0.01$ and $\delta_{\text{disp}} / \lambda \approx 0.1$, i.e. at frequencies $f < \dfrac{c_0}{100\delta_{\text{disp}}}$ and $f \approx \dfrac{c_0}{10\delta_{\text{disp}}}$. A practical measuring device could use a broadband signal containing a range of frequencies to cover a range of boundary layer thicknesses, assuming that such a broadband transducer could be built. It would be useful to confirm this effect for other boundary layer profiles

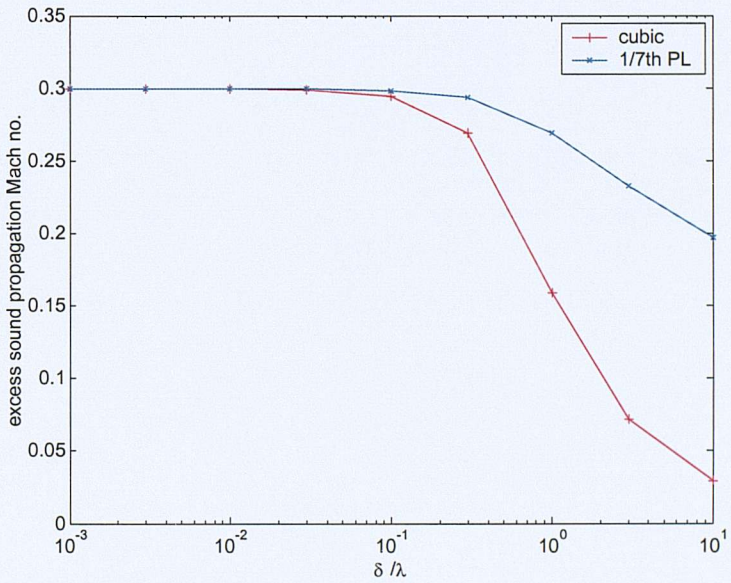

Figure 8.14 Variation of excess propagation Mach number, (M_d –1), with boundary layer thickness at a free-stream Mach number of 0.3; comparison of data for cubic and 1/7th power law profiles.

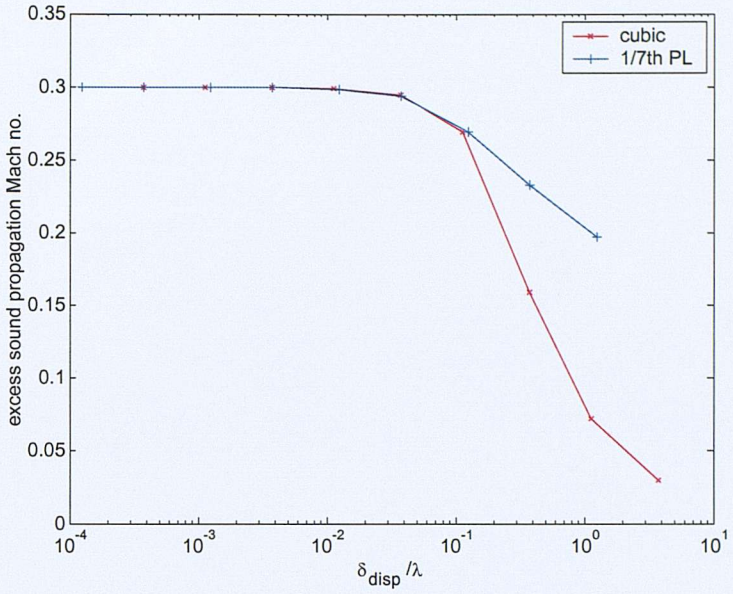

Figure 8.15 Variation of excess propagation speed with displacement thickness of the boundary layer at a free-stream Mach number of 0.3; comparison of cubic and 1/7th power law profiles.

8.5 Conclusions

This chapter has demonstrated the use of the model of sound propagation through a shear flow to predict the phase velocity of sound convected between a source and a downstream receiver. The model shows that a device working at a frequency where the boundary layer is thin on the wavelength scale would detect the free stream Mach number of the flow.

For boundary layers greater than one hundredth of a wavelength thick the phase velocity is reduced. It is shown that this dispersive effect is potentially useful as a means of determining the boundary layer displacement thickness by measuring phase velocity at two or more frequencies. The greater the number of frequencies used the more information could be gathered about the boundary layer profile.

The variation of amplitude and/or convected phase speed with angle downstream is also shown to be potentially useful for determining the direction of the local flow vector.

Chapter 9

9. COMPARISON WITH VALIDATION FLOW MEASUREMENT EXPERIMENTS

This chapter describes an experiment that was undertaken as a consultancy project to test the concept of measuring boundary layer properties using ultrasound. The work was carried out in collaboration with Gill Electronic R&D of Lymington, manufacturers of ultrasonic anemometers, and was funded by DERA (now QinetiQ). The experiments were performed in two phases during 2000 - 2001, and were carried out in parallel with initial development of the mathematical model.

9.1 Test apparatus

Figure 9.1 shows the test fixture that was manufactured to produce a variable thickness boundary layer over a flat plate containing the flow transducer . The device was installed in the 8' x 7' wind tunnel at the University of Southampton, and angled downwards to give a specified angle of attack into the flow. The leading edge of the plate was initially square, but subsequently had a rounded nose attached to give a more controlled initial growth of the boundary layer.

The flow over the transducer could be varied by changing the wind speed in the tunnel, the angle of attack of the plate and the profile of the leading edge. The development of the flow over the plate was monitored by a line of pressure tappings along the length of the plate, but there was otherwise no independent measurement of boundary layer thickness.

The test equipment was based on development hardware for the standard Gill free-field anemometers, with adaptations for making measurements at a wall. The device used a pulse of ultrasound, with a primary frequency of approximately 180 kHz. The pulse contains a phase marker caused by an abrupt phase change in the electronic driving signal of the system. The details of how the instrument carries out the measurements is beyond the scope of this thesis and it was used merely as a tool for measuring phase speed from time of flight.

Each transducer comprised a cylindrical piezo-electric crystal with an impedance matching layer, as used in other Gill instruments. The transducer face was approximately 5 mm

diameter, corresponding to about $ka = 8$ at 180 kHz. Normally such transducers are required to radiate a narrow beam along the axis of the transducer and this relatively large ka value is advantageous. In the current application however the transducers are required to radiate laterally and the directivity associated with a large ka is a disadvantage. This was countered by mounting the transducer under a cap with a 2 mm diameter hole, thus reducing the effective source size to $ka = 3.3$. From a measurement survey of the transducer directivity no side lobes could be detected, as expected for a piston with $ka < 3.83$, [2]. Further reduction in ka by using smaller apertures was not beneficial as this reduced the sound output too much to make the signal detectable downstream. Trials with a 90 kHz primary frequency were also attempted but were unsuccessful because of hardware problems.

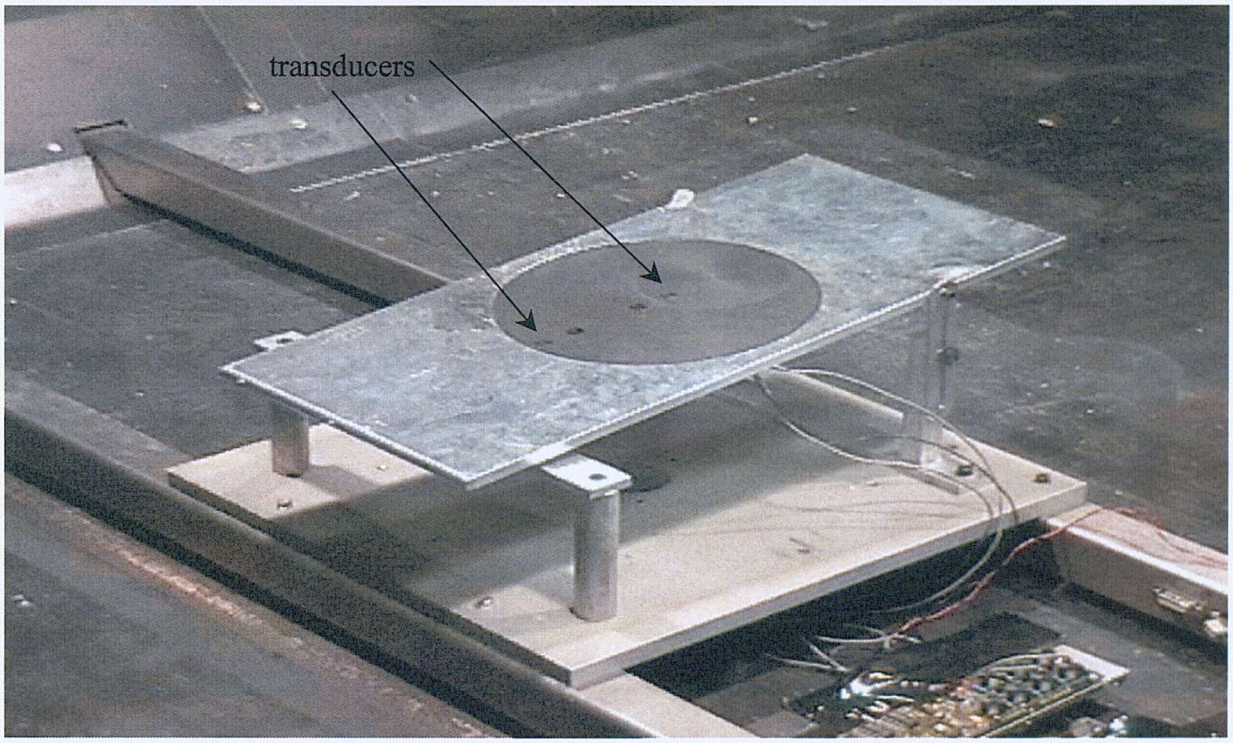

Figure 9.1 Test arrangement showing the ultrasonic transducers mounted in a rotatable housing. Measurements of propagation speed are made as a function of wind tunnel speed and plate angle of attack

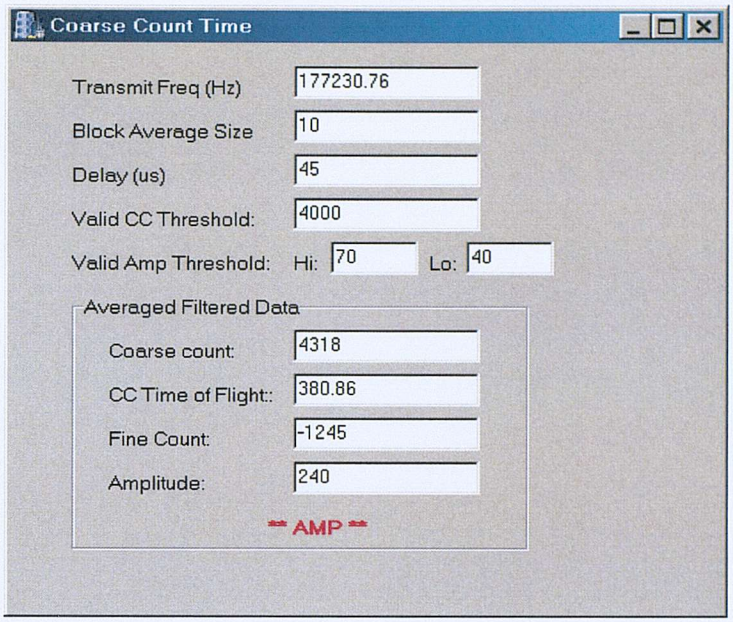

Figure 9.2 Graphical User Interface for the instrument. The time of flight measurement comprises a 'coarse count' of whole oscillation cycles and a 'fine count' phase measurement.

The key data presented in the following sections comprises measurements made with an ultrasonic frequency of nominally 180 kHz, using a 2 mm transducer aperture and a spacing of 0.104 m between the upstream and downstream transducers. The transducers were mounted in rotating housings so that their spacing and orientation relative to the flow direction could be varied. The mid point of the two transducers was nominally 0.200 m from the leading edge of the plate for most of the measurements.

9.2 Downstream propagation, source and receiver aligned in the flow

9.2.1 Measured data

The data presented in this section are for the receiver positioned downstream of the source. Measurements were made with flow velocities of 0 - 45 m/s in 5 m/s steps with the plate configured as follows:

- 0° angle of attack, square leading edge
- 0° angle of attack, semi-circular leading edge
- -6° angle of attack, square leading edge
- -6° angle of attack, semi-circular leading edge

The raw test data, the measured time of flight in μs, and the amplitude of the downstream signal, are shown in figure 9.3 and 9.4.

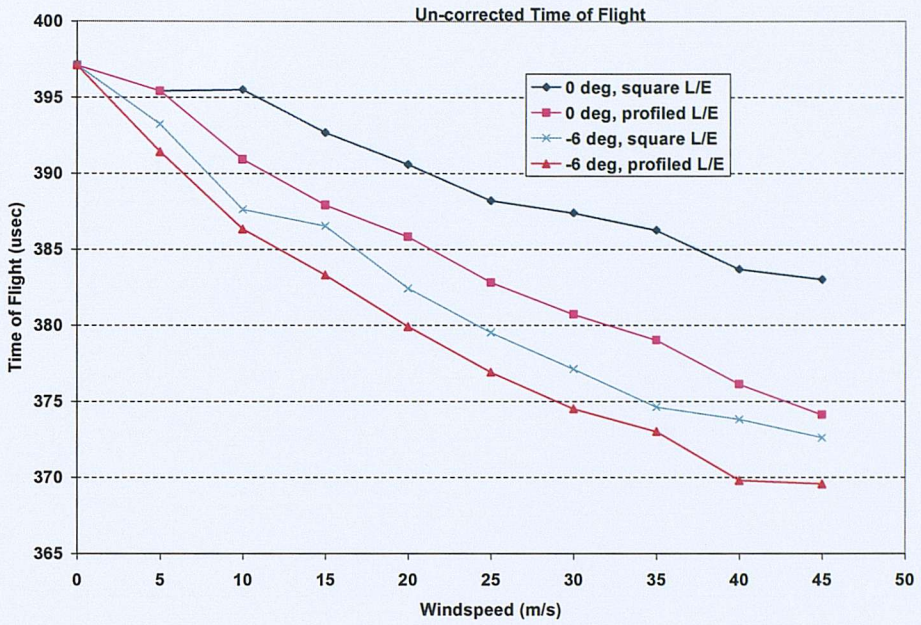

Figure 9.3 Comparison of time of flight for square and profiled leading edges as a function of tunnel wind speed and angle of incidence.

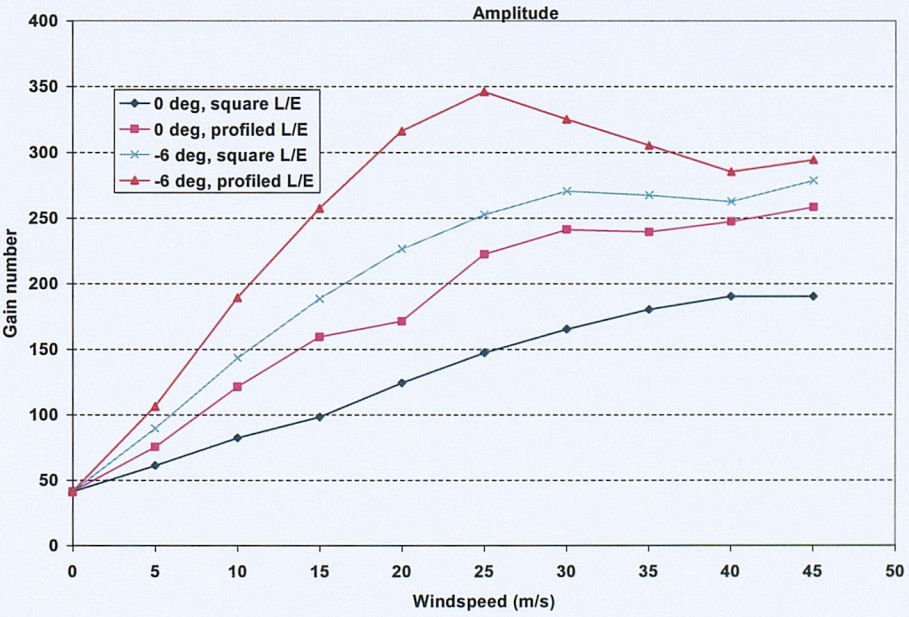

Figure 9.4 Comparison of downstream signal amplitude for square and profiled leading edges as a function of tunnel wind speed and angle of incidence

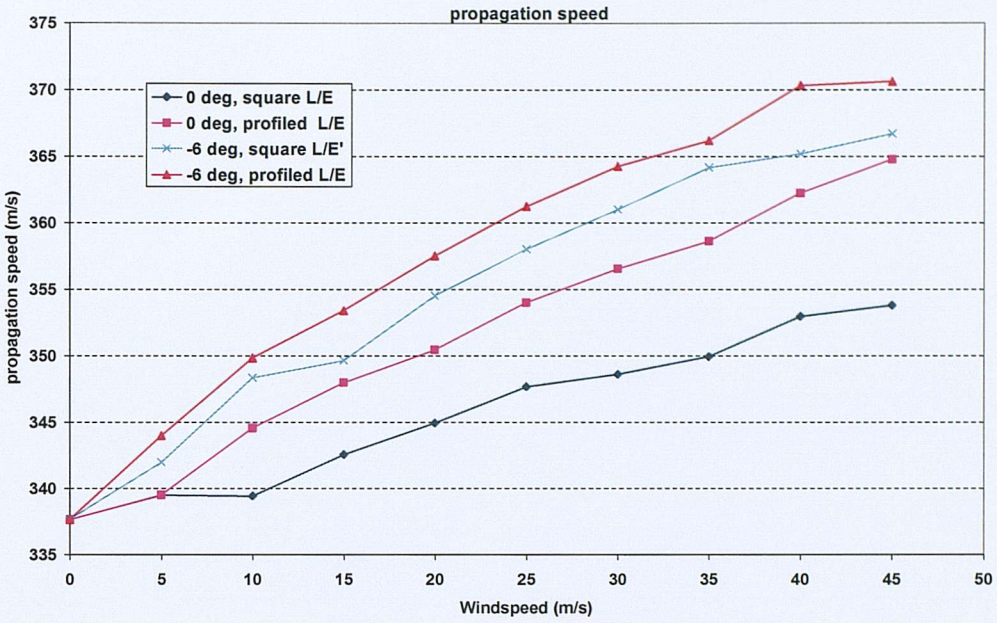

Figure 9.5 Measured apparent propagation speed as a function of flow velocity and angle of attack using data from figure 9.1

Figure 9.5 shows the sound speed deduced from the data; the data has been scaled slightly to give the same velocity at a wind speed of 0 m/s since the temperature of the tunnel was changing during the course of the experiments.

It may be expected that applying a negative angle of attack or using a round leading edge would reduce the thickness of the boundary layer over the transducer and hence increase the pulse propagation speed. This effect is clearly seen in figure 9.5, with the round leading edge at –6° angle of attack giving the highest propagation speed and the square leading edge at 0° angle of attack giving the lowest propagation speed.

With respect to the amplitude information shown in figure 9.4, the increase in downstream level may explained in terms of the channelling effect noted in chapter 7. It is calculated in the next section that $\delta / \lambda \approx 1$ in this test, and figure 7.2e) shows that for this condition there is significant downstream channelling of sound. As the flow velocity increases the effect grows, although this may be partially limited by the fact that the boundary layer gets thinner as the velocity increases. Another contributory factor is that the transducer in the experiment was not a point source and figure 7.3 shows that the main directivity lobe is progressively directed downstream as the flow rate increases.

9.2.2 Comparison of the test rig measurements and the prediction model for downstream propagation

To make quantitative comparisons between the test measurements and the prediction model it is necessary to determine the mean boundary layer thickness between the source and receiver transducer locations. No account will be taken of the fact that the boundary layer continues to grow over the finite distance between the transducers.

The only configuration for which the boundary layer thickness can reasonably be estimated from first principles is the test with the profiled leading edge and 0° angle of attack. From simple boundary layer theory the thickness of a laminar boundary layer may be calculated from the Reynolds number based on distance from the leading edge using the formula:

$$\frac{\delta_{99}}{x} = 4.91\,\mathrm{Re}_x^{-0.5} \tag{9.1}$$

where $\mathrm{Re}_x = \dfrac{M_0 c_0 x}{\nu}$ and ν is the kinematic viscosity.

Figure 9.6 plots the Reynolds number and predicted boundary layer thickness as a function of the streamwise position x, for 10 m/s and 45 m/s flows. Transition occurs nominally at $\mathrm{Re}_x = 5\times10^5$ and so the boundary layer is probably laminar throughout the measurement range of the experiments, provided the flow remains attached This means that the cubic boundary layer profile will be a reasonable approximation to the actual flow profile.

The boundary layer thickness to wavelength ratio at the mid point of the transducer is plotted as a function of flow velocity in figure 9.7. The boundary layer is approximately 1 wavelength thick at 10 m/s and half that at 45 m/s.

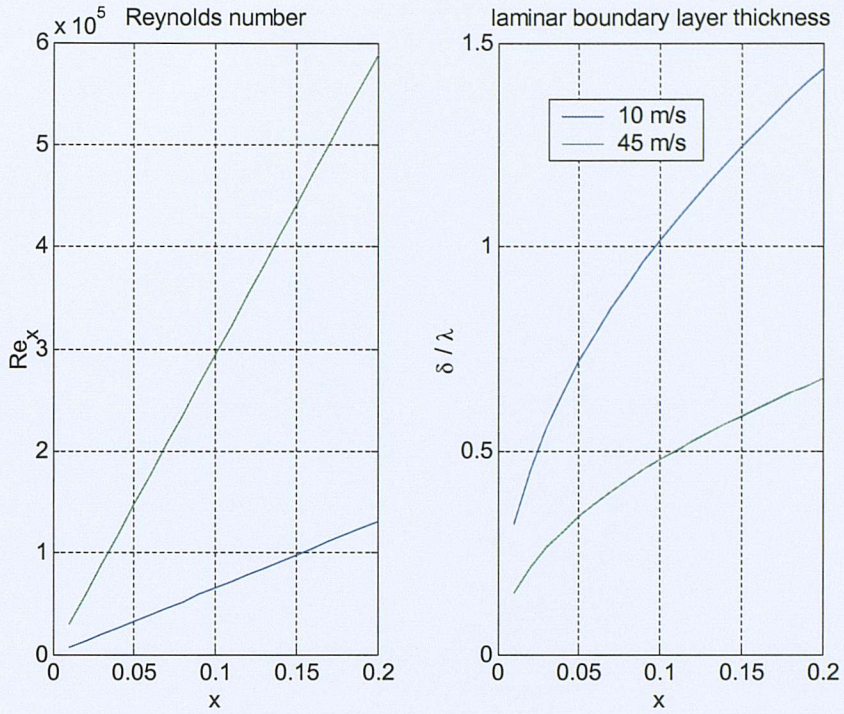

Figure 9.6 Estimated Reynolds number and boundary layer thickness for 10m/s and 45 m/s at 0° angle of incidence.

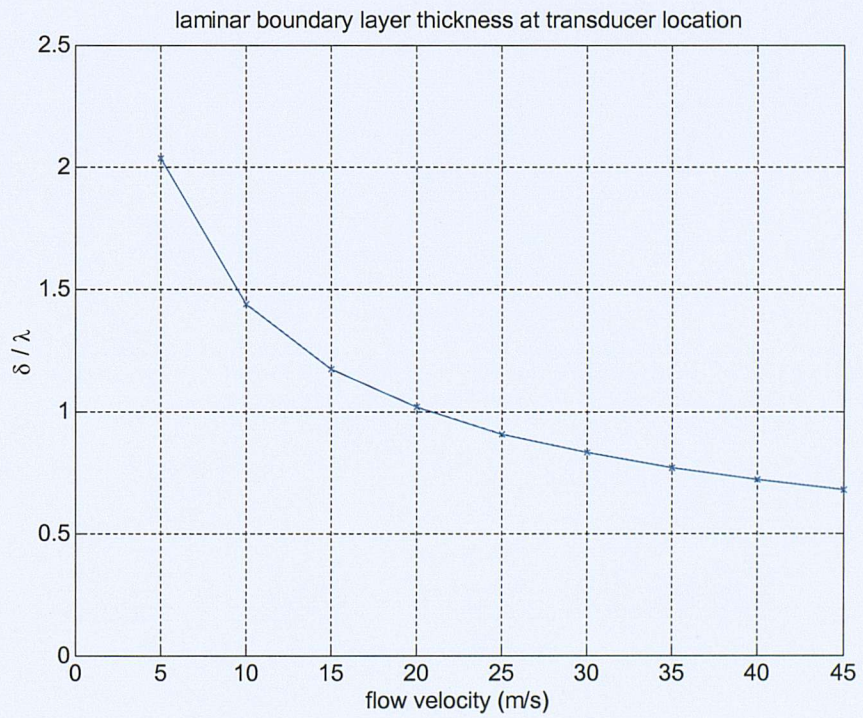

Figure 9.7 Estimated boundary layer thickness at the mid transducer location for the test rig at 0° angle of incidence and with a profiled leading edge.

By using the boundary layer thickness estimates of figure 9.5, the mathematical model of Chapters 6 and 7 may be used to simulate the measurements shown in figure 9.3, for the 0° angle of attack with a profiled leading edge configuration. The source *ka* value used in the predictions was 2.84, compared with the nominal value of $ka = 3.3$ for the actual source.

The predicted and measured convected wave speed data are shown in figure 9.8, and the predicted and measured Gain Number is given in figure 9.9. In both cases the predictions have been adjusted to give the correct measured value at zero flow velocity. For the velocity calculation this was a correction downwards of approximately 3 m/s, which is justified since there is an unknown system delay in the measurements associated with transmission through the transducer. The adjustment to the gain is justified since the actual source level of the Gill device is unknown.

For both the velocity data and the Gain data the model agrees remarkably well with the measurements, predicting changes to within 15% accuracy. This is good agreement considering some of the approximations which are included in the model, for example

- the assumption of a constant boundary layer thickness between source and receiver.
- the relatively crude estimate of boundary layer thickness.
- the method of approximating the actual source directivity.
- The algorithm for measuring time of flight and pulse amplitude in the Gill instrument has been optimised for different conditions, and may be subject to inaccuracies in the current configuration. In particular, the fact that sound propagation in the boundary layer is dispersive may affect the accuracy with which phase speed can be measured with the Gill analysis method.

The agreement would be improved if a thicker boundary layer were used in the model; it might be expected that the thick leading edge of the plate could give rise to a thicker than expected boundary layer.

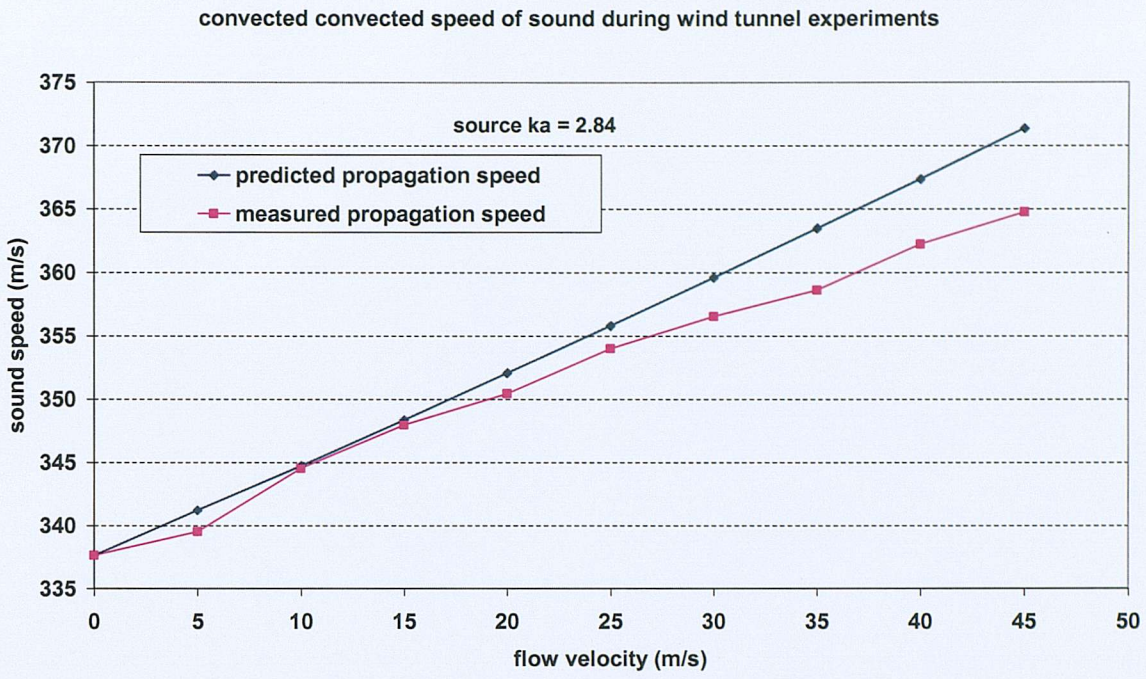

Figure 9.6 Comparison of predicted and measured variation of convected wave speed as a

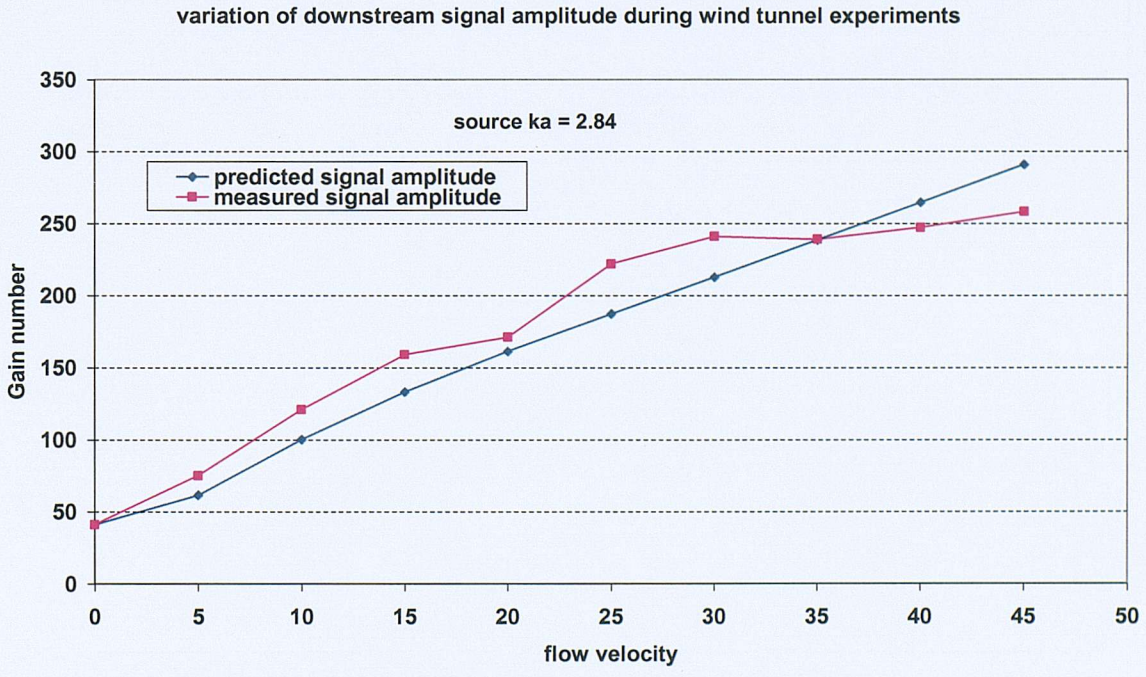

function of wind tunnel flow velocity; receiver downstream of source.

Figure 9.7 Predicted and measured variation of gain number as a function of wind tunnel flow velocity; receiver downstream of source.

9.3 Propagation transverse to the flow

The experimental rig include nested rotatable housings, just visible in the figure 9.1, which could be used to vary the angle of the transducers to the flow. This system was used to measure the time of flight and amplitude of pulses as a function of flow velocity and angle to the flow.

Tests were only performed with a –6° angle of attack on the plate. This means that it is not possible to easily make comparisons with the mathematical model. Qualitative comparisons can be made however, and for this purpose it is useful to point out two likely effects of tilting the plate down into the flow; the flow velocity over the plate will be increased and the boundary layer thickness will be reduced.

The raw time of flight data is presented in figure 9.8. As described in section 8.2, the time of flight is generally lowest for downstream propagation, 0° rotation, and is highest when the transducers are rotated to an angle of 90° to the flow. There appears to be an offset in the 0° data presented here, possibly due to a changing speed of sound due to temperature changes in the tunnel.

In Section 8.2 it was noted for sound propagation at 90° to the flow that the propagation Mach number would be less than 1.0; there is evidence of this in the data, with an increasing trend in the time of flight as the flow velocity increases.

The pulse amplitude data acquired in the experiment are shown in figure 9.9. Again the trends are consistent with the findings from the mathematical model described in Section 8.2 for a boundary layer approximately one wavelength thick. The amplitude is greatest in the downstream direction, and there is a reduction in amplitude for propagation at 90° to the flow.

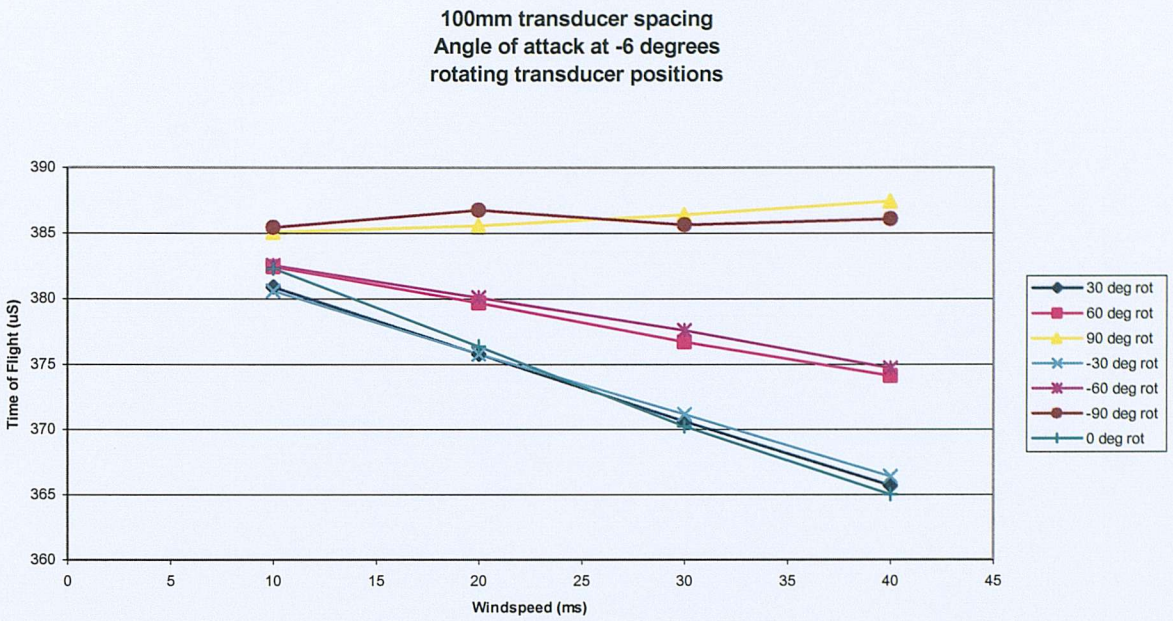

Figure 9.8 Raw time of flight data for sound propagation at various angles to the direction of flow

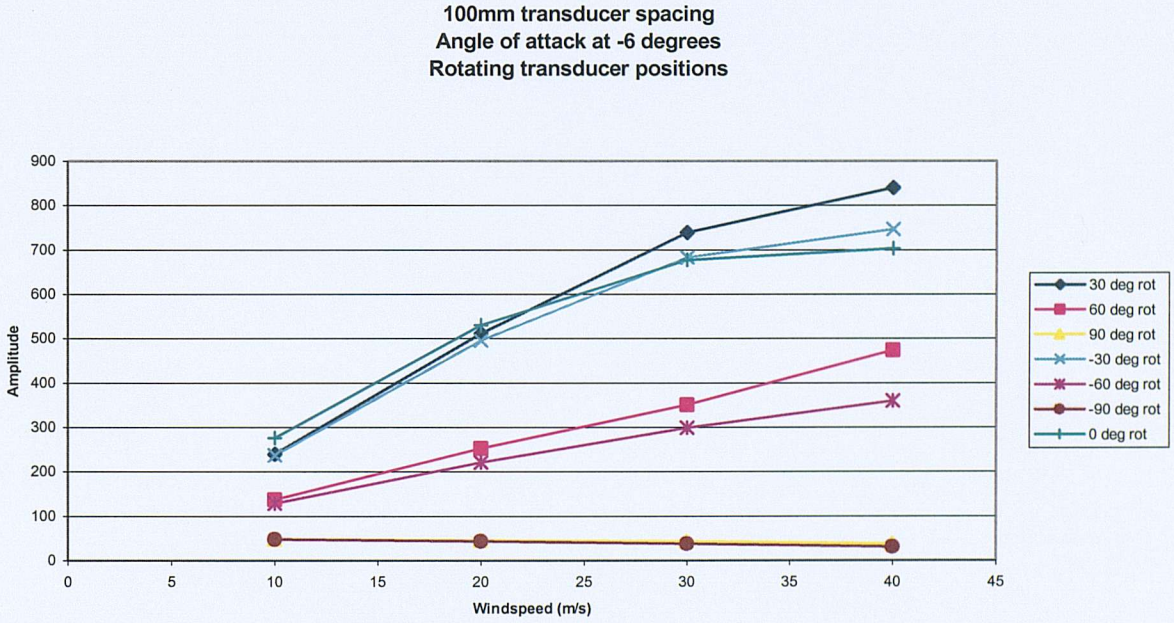

Figure 9.9 Raw pulse amplitude data for sound propagation at various angles to the direction of flow.

9.4 Conclusions

The experimental data has confirmed many of the predictions of the mathematical model, either quantitatively or qualitatively.

- The test results show that the sensor displays a fairly linear relationship between convected speed of sound and actual flow velocity for free stream flow velocities up to 45 m/s, Mach 0.12. The acoustic model suggests that, assuming incompressible flow, this linear relationship continues to higher Mach number.

- The mathematical model shows a strong relationship between the boundary layer thickness and the convected speed of sound when $\delta / \lambda > 0.1$. This behaviour has been confirmed qualitatively in the experiment by varying the angle of attack of the plate to change the flow conditions over the plate.

- For the one test case where it was possible to predict the boundary layer thickness with reasonable accuracy from first principles, for which $0.7 < \delta / \lambda < 2.0$ depending on flow velocity, the measured variation of convected speed of sound agreed well with the predictions of the model

- For sound propagation transverse to the flow the variation of both the convected speed of sound and the amplitude agreed qualitatively with the predictions of the model.

Chapter 10

10. OVERALL CONCLUSIONS, FURTHER WORK AND OTHER APPLICATIONS

10.1 Overall conclusions from the study

10.1.1 Flow measurement

The initial motivation for this study was a requirement to model the behaviour of a device for measuring the properties of a flow over a surface. For the one test case where it was possible to predict the boundary layer thickness with reasonable accuracy from first principles the measured variation of sound propagation speed and the downstream amplitude agreed well with the predictions of the model. The trends in other data, for which it was not possible to make quantitative predictions, also agreed with the predictions of the model.

This good agreement with preliminary experiments gives confidence that the model may be used to design an improved system, for example in the selection of operating frequencies and the size and spacing of transducers, so as to provide good measurement accuracy and operating characteristics.

The results presented in Chapter 8 have shown that to measure free-stream flow velocity accurately the device should ideally operate at a frequency such that the boundary layer displacement thickness is less than $1/100^{th}$ of a wavelength. This shows that, for the purposes of measuring free-stream velocity, the operating frequency in the experiment, for which $\delta/\lambda \approx 1$, was far too high.

The mathematical model predicts a strong relationship between the boundary layer thickness and the convected speed of sound when $\delta/\lambda > 0.1$. This behaviour has been confirmed qualitatively in the experiment by varying the angle of attack of the plate to change the flow conditions over the plate. By using a second operating frequency, where the boundary layer displacement thickness is close to $1/10^{th}$ of a wavelength, it should also be possible to infer the boundary layer thickness. Clearly, if the boundary layer thickness is not already known approximately, measurements using a range of frequencies should be made so that the

variation of propagation speed with frequency can be compared with a set of calibration curves based on figure 8.8.

Where the source and receiver are aligned with the flow the system may be designed to correctly measure free-stream mean flow velocity. However, if the angle of the mean flow is unknown, multiple receiver transducers could be used to also determine the flow direction. The experimental data with sound propagation transverse to the flow showed a variation of both the propagation speed and the amplitude that agreed qualitatively with the predictions of the model. The variation in amplitude of the sound field around the source also contains potentially useful information about the flow direction and the boundary layer thickness that could be used to enhance a measurement system.

The acoustic model suggests that, assuming isothermal flow and a constant boundary layer thickness, there is a linear relationship between propagation speed and free-stream flow velocity up to high Mach numbers. This is confirmed in the test results by the ability of the model to predict the data in figure 9.6, although this data is complicated by the fact that the boundary layer is varying with flow velocity.

10.1.2 Governing equations and critical layers

In order to be able to predict the sound field around the source transducer with confidence it was necessary to investigate alternatives to the governing equation for sound propagation in a parallel shear flow given by Pridmore-Brown, [5]. This was because a) the Pridmore-Brown equation requires the evaluation of the mean velocity gradient that becomes infinite at the wall for an idealised turbulent boundary layer profile, and b) in the sound radiation problem the equation must be solved for high positive wave numbers where there is a critical layer in the boundary layer which is difficult to integrate through.

Two alternative formulations were developed. The first, based on the pressure p and particle displacement q, (2.14a,b), resolves the problem of evaluating the mean velocity gradient, but has a singularity at a critical layer. The alternative formulation, based on pressure and displacement impedance χ, (2.32a,b), avoids the mean velocity gradient problem and also remains finite at a critical layer. Care in numerical solutions is still required at critical layers

since it is necessary to evaluate the ratio of two parameters which tend to zero there, but it is shown that the ratio is finite and the equations are well defined there.

In the course of deriving these new governing equations a number of general properties for solutions at a critical layer have been demonstrated. These properties, given in Section 2.5, apply to all flow profiles, and are useful for validating numerical solutions. The key properties are that $\frac{\partial p}{\partial z} = 0$ and $\chi = 0$ at a critical layer and that solutions are real valued everywhere in the boundary layer when a critical layer is present. Other properties listed may be useful in other ways, in particular they provide an understanding of which parameters remain finite (pressure p, particle velocity u_z, displacement impedance χ, and also $\frac{\partial u_z}{\partial z}$ and $\frac{\partial \chi}{\partial z}$) and which become infinite (particle displacement q, and $\frac{\partial q}{\partial z}$). It has been shown that the commonly assumed boundary condition of continuity of particle displacement does not apply across a critical layer since q must change sign.

10.1.3 Outgoing wave solutions of the governing equations

It was known previously that, for a vibrational wave in the surface radiating into a uniform flow, the pressure wave in the fluid may be either cut-on or cut-off depending whether the surface wave is propagating supersonically or subsonically relative to moving fluid.

The results presented in Chapter 4 demonstrate far more complex behaviour for sound propagating through a shear flow, with upstream propagating waves being refracted away from the surface and downstream propagating waves being channelled by the boundary layer. Two particular effects are shown to significantly alter the sound field radiated into a shear flow compared with radiation into a uniform flow:

- Upstream propagating waves in the range $-1/(1-M_0) < k_x/k_0 < -1$ propagate subsonically relative to the flow in the lower boundary layer, thus being cut-off and decaying away from the surface, whilst propagating supersonically relative to the flow in the outer portion of the boundary layer. In this case the wave tunnels through the flow near the wall until it can propagate in the outer boundary layer. In consequence,

an analysis using uniform flow will over predict the pressure generated in the fluid for these negative wave numbers.

- Downstream propagating waves in the range $1/(1+M_0) < k_x/k_0 < 1$ are cut-on at the wall, but cut-off in the main body of the flow, and thus propagate for a short distance away from the surface but decay thereafter. In consequence an analysis based on uniform flow will underestimate the pressure near the wall for these wave numbers.

10.1.4 Power flow and radiation efficiency

Chapter 5 considers power radiated from a surface vibrating under a boundary layer. An important result derived in this chapter is that acoustic power flow through a shear layer is conserved. As a result a radiation efficiency based on the radiation impedance at the surface is well defined.

The radiation efficiency is shown to be a strong function of the boundary layer thickness for surface waves propagating upstream near coincidence. This effect may be of concern for active noise control techniques aimed at low order upstream-propagating modes in aero-engine intakes. In addition it is clear that the radiation impedance of a mode of vibration in a plate will be modified compared with the value for uniform flow given in [28].

An interesting feature of the results for thick boundary layers is that the radiation efficiency of waves propagating against the flow converges towards the zero flow value; whereas for downstream propagating waves, no power is radiated by the surface in the wave number range $1/(1+M_0) < k_x < 1$, unless there is damping in the fluid.

10.1.5 Sound field generated by a piston under a boundary layer

Chapter 6 has outlined how to obtain the spatial distribution of pressure from the inverse Fourier transform solutions in the wave number domain. The application of this method is unusual in that the function to be Fourier transformed is a numerically integrated solution to the governing equations.

Errors can occur in the predicted sound field because of the necessary compromises in a numerical implementation of the method. Firstly, the discretization of the problem gives rise

to image sources and may give poor resolution of coincidence peaks; these errors can be controlled by including damping in the model. Secondly, the asymmetry of the radiation impedance when a mean flow is applied leads to 'leakage' in the inverse Fourier transform; these errors can be controlled by windowing the wave number spectrum of the source.

The contour plots in figures 7.5a-g) show that the sound field radiated by a compact source is a strong function of Mach number and boundary layer thickness. For thin boundary layers the change to the sound field relative to the zero flow case is dominated by the effect of convective amplification that increases the pressure upstream of the source and decreases the pressure downstream. The power radiated by the source is also increased by the flow. These effects can be predicted by analytical uniform flow models and the numerical model has been shown to converge to the correct answer for thin boundary layers.

As the boundary layer thickness grows, a noise shadow forms upstream of the source and channelling of the sound by the boundary layer increases the level downstream. The power radiated is also reduced towards the zero flow value.

The model is also able to predict the radiation from a non-compact source, with a combination of convective amplification and refraction again apparent.

10.2 Further work

This section outlines topics which fall with within the general scope of this thesis, but where there are possibilities for further in-depth investigation. The next section discusses a few other applications that could benefit from the understanding and methods provided by this study.

Far-field sound radiation

The contour plots produced in Chapter 7 show the sound field in the vicinity of the source, but for many purposes it useful to be able to predict the far field directivity . Although only the pressure distribution around the source has been shown here, the velocity distribution can also easily be obtained from the inverse Fourier transform of the velocity wave number spectrum. The acoustic particle velocity at the edge of the boundary layer may be used as a

virtual source distribution, radiating into a uniform flow. The pressure in the far-field may then be calculated from the Rayleigh integral, using the Frauenhofer approximation at large distances from the source as required.

Density and sound speed profiles

In adiabatic flows at high subsonic Mach numbers or with flow over heated walls there may be density and sound speed gradients through the boundary layer. These will modify both the wave number dependent refraction effects described in Chapter 4 and the source power output described in Chapter 7. The equations derived in Chapter 2 and the computer programs used to generate the results in subsequent chapters may be applied to this problem with only minor modifications.

Modal radiation efficiency of vibrating plates and other sources

Recent publications have considered the radiation efficiency of panels radiating into a uniform mean flow [27,28]. The model developed here, which has thus far only been used to predict sound radiation from uniform pistons, may be applied without further development to predict the effect of a non-uniform flow on the radiation efficiency of non-uniform sources such as modes of a vibrating panel or phased arrays of sources producing directional sound fields. It would also be useful to show the effect of flow for non-compact pistons to extend the results presented in Section 7.2.2.

Further development of the flow measurement concept

This study has demonstrated the basic principles of a device to measure the characteristics of a mean flow over a plate using single source and receiver transducers. To carry this concept forward the model could be used to optimise design parameters such as operating frequencies and transducer size and spacing for specific applications (e.g. turbulent boundary layers on aircraft, laminar boundary layers in ships, etc.) and the size and spacing of the transducers.

There are also a number of possible geometrical developments of the concept, for example using an array of receiver transducers distributed around a single or multiple source; it may be advantageous for example to measure relative phase between two receiver transducers rather than between source and receiver.

The principle of measuring boundary layer displacement thickness should be tested for other flow profiles

10.3 Other applications

Modified boundary conditions for sound propagation in soft walled ducts

Equations (2.30) and (2.31) describe the variation of the local fluid displacement admittance or displacement impedance through a boundary layer. In this thesis equation (2.30) has used to integrate from a radiation condition at the edge of the boundary layer to provide a radiation condition at the wall. Either equation can potentially be used to take a boundary condition at the wall and integrate outwards through the boundary layer to provide an equivalent condition at the edge of the boundary layer. This would be a useful technique for determining the effect of a boundary layer on the attenuation from an acoustic liner in a duct. Tester [40] has already considered this problem, but the relatively simple form of (2.30) and (2.31) may make it easier to obtain full analytic solutions for some simple boundary layer profiles.

Sound radiation from a source in a shear layer

The solutions found in this thesis are for outgoing waves. By also finding solutions for inward propagating waves the sound field radiated from a source in the boundary layer may be determined. This problem is of interest for environmental noise problems, where elevated sources radiate noise into under windy conditions, with the variability of the sound field downwind of the source being an area of current research.

Sound radiation from turbulence convected past a trailing edge

Turbulence convected over the trailing edge of an aircraft wing or other aerofoil is a source of aerodynamic noise. Whereas analytic models suggest that the sound field produced by this source should peak upstream in the plane of the wing, numerical modelling using CAA methods [41] have shown that refraction by the boundary layer modifies the sound field. By modelling the velocity distribution downstream of the trailing edge as a distributed source the effect of the boundary layer on the power output of the source could be investigated.

Inverse source identification methods

Inverse methods use analytically predicted Greens function to infer source distributions from far-field measurements using a microphone array. The precision with which sources can be localised depends on the accuracy of the Greens functions, and, where flow is considered, it is generally assumed to be uniform flow or with a zero thickness shear layers. The results in Chapter 6 suggest that the Greens function is significantly modified by a boundary layer of finite thickness, and that it may be useful to take this into account when applying inverse methods to the identification of sources of aerodynamic noise.

Active noise control in ducts

The sound field radiated upstream by a source has been shown to be a strong function of boundary layer thickness for grazing angles to the wall. The effect of a boundary layer is thus potentially important if there is a requirement to control modes which are well cut-on in a duct, and are propagating upstream in a high Mach number flow at low angles to the duct axis.

REFERENCES

1 M.C. Junger and D. Feit, 1993, *Sound, Structures and Their Interaction.* Acoustical Society of America.

2 A.D. Pierce, 1989, *Acoustics, An Introduction to its Physical Principles and Applications.* Acoustical Society of America

3 Morse and Ingard, 1986, *Theoretical Acoustics.*

4 Dowling and Ffowcs Williams, 1983, *Sound and Sources of Sound.* Ellis Horwood

5 D.C. Pridmore-Brown, 1958, *Journal of Fluid Mechanics* 4, 393-406. Sound propagating in a fluid flowing through an attenuating duct.

6 W. Eversman, 1994, NASA SP1258 volume 2. Chapter 13, Theoretical Models for Duct Acoustic Propagation and Radiation.

7 NK Agarwal and MK Bull 1989, *Journal of Sound and Vibration* 132(2) 275-298. Acoustic propagation in a pipe with fully developed turbulent flow.

8 C.K.W. Tam, 1975, *Journal of Sound and Vibration* 38(1) 51-79. Subsonic jet noise generated by large scale disturbances

9 C.K.W. Tam and P.J. Morris, 1980, *Journal of Fluid Mechanics* vol 98 part 2 349-381. The radiation of sound by the instability waves of a compressible plane turbulent shear layer

10 A.Agarwal, P.J.Morris and R.Mani, 2003, *AIAA paper 2003-0878.* The calculation of sound propagation in nonuniform flows: suppression of instability waves

11 Tam and Auriault Mean flow refraction effects on sound radiated from localised sources in jets

12 L.M.B.C. Campos, J.M.G.S. Oliveira and M.K. Kobayashi 1999 *Journal of Sound and Vibration* 219(5), 739-770. On sound propagation in a linear shear flow.

13 L.M.B.C. Campos and M.K. Kobayashi, 2000, *Journal of Fluid Mechanics 424 303-326.* On the reflection and transmission of sound in a thick shear layer.

14 C Peyret and G Elias, 2001, *JASA* 110 (2) Finite element method to study harmonic aeroacoustic problems

15 H. Galbrun, 1931, *Propagation d'une onde sonore dans l'atmosphere et theorie des zones de silence.* Gautier Villars

16 G Gabard F Treyssede M Ben Tahar *to be published in Journal of Sound and Vibration.* A numerical method for vibroacoustic problems with sheared mean flows.

17 V Pagneux and Y Auregan, 1998, *AIAA paper 98-2281.* Acoustic modes in duct with parallel shear flow and vibrating walls

18 L.M. Brekhovskikh and O.A. Godin, 1990. *Acoustics of layered media vols I and II.* Springer Verlag

19 F.B. Jensen et al, 1994. *Computational Ocean Acoustics.* American Institute of Physics.

20 S.M. Candel, 1977. *Journal of Fluid Mechanics* Vol83 part 3, pp465-493. Numerical solution of conservation equations arising in linear wave theory: application to aeroacoustics.

21 M. Goldstein, 1974. *JASA* vol. 56 no. 2. Unified approach to aerodynamic sound generation in the presence of solid boundaries

22 Morse and Ingard, 1986. Theoretical Acoustics

23 S.J. Rienstra 1999, *Journal of Fluid Mechanics* Vol 380, Sound transmission in slowly varying circular and annular lined ducts with flow.

24 G.B. Arfken and H.J. Weber 1995. *Mathematical methods for Physicists.* Academic Press.

25 D.G. Crighton, et al, 1992. *Modern Methods in Analytical Acoustics*, Springer Verlag.

26 E.J. Rice, 1979. *AIAA conference paper 79-0624.* Modal Propagation angles in ducts with soft walls and their connection with suppressor performance.

27 W.R. Graham, 1998. *Proc. Royal Society*, 454, 111-137. The effect of mean flow on the radiation efficiency of rectangular plates

28 KD Frampton 2002. *JASA* 113 (5), 2663-2673. Radiation efficiency of convected fluid loaded plates

29 C.L. Morfey, 1971. *Journal of Sound and Vibration* 14(2) 159-170. Acoustic energy in non-uniform flows.

28 R.H. Cantrell and R.W. Hart, 1964. *JASA* 36, 697. Interaction between sound and flow in acoustic cavities: mass, momentum and energy considerations.

29 B.J. Tester, 1973. *Journal of Sound and Vibration* 28(2), 205-215. Acoustic energy flow in lined ducts containing uniform or plug flow.

30 J.E. Ffowcs Williams and D.J. Lovely, 1975, *Journal of Fluid Mechanics* 71, 689-700. Sound radiation into uniformly flowing fluid by compact surface vibration.

31 F.G. Leppington and H Levine, 1979. *Journal of Sound and Vibration* 62(1) 3-17. The effect of flow on the piston problem in acoustics.

32 H. Levine, 1980. *Journal of Sound and Vibration* 71(1) 1-8. A note on sound radiation

into a uniformly flowing medium

33 C.L. Morfey, 2003. Private communication

34 C.L. Morfey and H.K. Tanna, 1971. JSV 15 325-351. Sound radiation from a point force in circular motion.

35 L. Cremer, M. Heckl and E.E Ungar,, 1973. *Structure Borne Sound*. Springer Verlag.

36 G.E. Hearn and A.V. Metcalfe 1995 *Spectral Analysis in Engineering*.

37 N. Curle and H.J. Davies, 1968. *Modern Fluid Dynamics*. Van Nostrand

38 V.Pagneux and B.Froelich, 2001. *Journal of Sound and Vibration* 346 (1) 137-155. Influence of low Mach number shear flow on acoustic propagation in ducts

39 http://www.gill.co.uk. Web site for Gill Instruments Ltd

40 B.J. Tester 1973, *Journal of Sound and Vibration* 28(2), 217-245. Some aspects of "sound" attenuation in lined ducts containing inviscid mean flows with boundary layers.

41 M. Lummer, J.W. Delfs and T Lauke, 2003. *AIAA* 2003-3109. Simulation of the influence of trailing edge shape on airfoil sound generation

42 M.A. Swinbanks 1975, *Journal of Sound and Vibration* 40(1), 51-76. The sound field generated by a source distribution in a long duct carrying sheared flow

43 T. Suzuki and S.K. Lele 2003, *Journal of Fluid Mechanics* 477, 129-173. Green's functions for a source in a boundary layer: direct waves, channelled waves and diffracted waves.